SANDIA REPORT
SAND2013-2481
Unlimited Release
Printed April 2013

History of HERMES III Diode to Z-Pinch Breakthrough and Beyond

(learning about Pulsed Power and Z-Pinch ICF)

Thomas W.L. Sanford

Prepared by
Sandia National Laboratories
Albuquerque, New Mexico 87185 and Livermore, California 94550

Sandia National Laboratories is a multi-program laboratory managed and operated by Sandia Corporation, a wholly owned subsidiary of Lockheed Martin Corporation, for the U.S. Department of Energy's National Nuclear Security Administration under contract DE-AC04-94AL85000.

Sandia National Laboratories

Issued by Sandia National Laboratories, operated for the United States Department of Energy by Sandia Corporation.

Available to DOE and DOE contractors from
U.S. Department of Energy
Office of Scientific and Technical Information
P.O. Box 62
Oak Ridge, TN 37831

Telephone: (865) 576-8401
Facsimile: (865) 576-5728
E-Mail: reports@adonis.osti.gov
Online ordering: http://www.osti.gov/bridge

Available to the public from
U.S. Department of Commerce
National Technical Information Service
5285 Port Royal Rd.
Springfield, VA 22161

Telephone: (800) 553-6847
Facsimile: (703) 605-6900
E-Mail: orders@ntis.fedworld.gov
Online order: http://www.ntis.gov/help/ordermethods.asp?loc=7-4-0#online

SAND2013-2481
Unlimited Release
Printed April 2013

History of HERMES III Diode to Z-Pinch Breakthrough and Beyond

(learning about Pulsed Power and Z-Pinch ICF)

Thomas W.L. Sanford
Diagnostics and Target Physics
Sandia National Laboratories
P.O. Box 5800
Albuquerque, New Mexico 87185-MSX1677

Abstract

HERMES III and Z are two flagship accelerators of Sandia's pulsed-power program developed to generate intense ɤ-ray fields for the study of nuclear radiation effects, and to explore high energy-density physics (including the production of intense x-ray fields for Inertia Confinement Fusion [ICF]), respectively. A diode at the exit of HERMES III converts its 20-MeV electron beam into ɤ-rays. In contrast, at the center of Z, a z-pinch is used to convert its 20-MA current into an intense burst of x-rays. Here the history of how the HERMES III diode emerged from theoretical considerations to actual hardware is discussed. Next, the reverse process of how the experimental discovery of wire-array stabilization in a z-pinch, led to a better theory of wire-array implosions and its application to one of the ICF concepts on Z--the DH (Dynamic Hohlraum) is reviewed. Lastly, the report concludes with how the unexpected axial radiation asymmetry measured in the DH is understood. The first discussion illustrates the evolution of physics from *theory-to-observation-to-refinement.* The second two illustrate the reverse process of *observation-to-theory-to refinement*. The histories are discussed through the vehicle of my research at Sandia, illustrating the unique environment Sandia provides for personal growth and development into a scientific leader.

ACKNOWLEDGEMENTS

This report resulted from the wonderful encouragement I was provided by my manager and colleague, Ray Leeper, to write this physics history of the HERMES III diode and the application of z-pinches to ICF to which I contributed to. I would like to thank not only Ray for this encouragement, but also for his recommendation to join his ICF team in the mid 1990s. I would also like to thank Wendland Beezhold for facilitating my initial employment and Juan Ramirez for suggesting I develop the HERMES III diode, and both scientists for my continued support at Sandia. I am grateful to Neal Singer, and Mary Ann Sweeney for their careful reading of this report. All inaccuracies, however, are mine. Lastly I thank Peggy Ballance for ushering this report through all of its hoops.

CONTENTS:

FIGURES:

1. Tom Sanford presenting his Science Fair Experiment to Admiral Frank Watkins at the Seattle King County Science Fair 1960.

2. Wire spark chamber.

3. Proton-Halo thesis experiment at Nevis Laboratory.

4. ACCMOR collaboration meeting at Schloss Ringberg near Munich 1980. Tom Sanford at bottom left.

5. HELIA showing the diode connected to either 19-cm or 2.2-m configuration. V1, V2, V3, V4 are capacitative voltage monitors.

6. HELA diode team, from left to right: John Halbleib, Tom Sanford, Chuck Heath, Jim Poukey, Tom Wright, Ray Mock, Dave Knott, Bob Craven, and Rich Adams.

7. HELA indented-anode diode. Arrows show electron path for each of three converter (C) locations.

8. HELIA B_θ lens diode showing average electron and radiation trajectories with no current and 70 kA in the lens.

9. HERMES III electron accelerator.

10. HERMES III Planar-Anode diode illustrating electron trajectories and radiation produced at (A) early or late time, (B) midway through the voltage rise or fall, and (C) peak power.

11. HERMES III diode team, from left to right: Jimmy Flores, Fran Current, Gerry Crowder, Ray Mock, Todd Borkey, Jim Poukey, Tom Sanford, and Tim Sheridan.

12. HERMES III short Gas Cell diode in intense bremsstrahlung mode. IA1 through IA4 and IC1 are current shunts.

13. HERMES III Compound-Lens diode. Is is a current shunt that monitors net current. Ir is a Rogowski coil that monitors the external current Ie.

14. Bill McAtee testing Compound-Lens diode.

15. Six phases of beam propagation in the long HERMES III gas cell as a function of pressure P and charge neutralization fraction f.

16. Long Gas-Cell transport using Extended-Planar-Anode diode as injector. IA1 through Ia5 are current shunts.

17. (A) Long Gas-Cell transport using Compound-Lens diode as injector. (B) Detail of upstream surface of the

graphite calorimeter. (C) Detail of the TLD array showing TLD placement. (D) Detail of a collimated Compton diode.

18. Tom Chaves adjusting Compound-Lens injector to long gas cell.

19. (A) Saturn configuration showing location of current diagnostics I_{stack}, I_{mitl}, I_{load} with respect to the insulator stack, MITLs, Adder, Feed, and Load sections. (B) Detail of Adder and Feed sections. (C) Detail of Load section showing position of Compact cathode wire array with respect to the eight anode current return posts. (D) Experimental arrangement showing location of radiation diagnostics.

20. (A) Experimental arrangement in the r-z plane showing the position of the wire array, the current return path in the anode housing, the load current monitors, and the post-hole convolute. (B) Load fixture for wires with inter-wire gaps of 0.6 mm and greater. (C) load fixture for arrays with inter-wire gap of 0.4 mm.

21. Terry Gilliland, Roberta Hanes and Ray Mock loading world's first high wire-number load at bottom of Saturn accelerator.

22. (A) Conversion of PBFA II to Z. (B) Z insulator stack and MITLs.

23. Z-pinch driven Static-Wall-Hohlraum ICF concept.

24. One-sided Static-Wall-Hohlraum arrangement on Z illustrating (A) side-on view with NIF-scale hohlraum, (B) end-on view, (C) off-axis diagnostic aperture, (D) 3° anode glide plane, (E) reduced scale hohlraum, and (F) shock-breakout diagnostic with reduced-scale hohlraum. The cylindrical target and radiation entrance hole are indicated by T and REH, respectively.

25. (A) Baseline wire-array drive on Z (B) using baseline target, and (C) pedestal target.

26. (A) Flop-Over fixture, (B) Hang-Down fixture, and (C) Weightless fixture.

27. Illustration of current shunting from wire core to surrounding vapor when localized ionization occurs. Er is the radial electric field at the surface of the wire.

28. Prof. Malcolm Haines, Dr. Thomas Sanford, and Prof. Valentin Smirnov after Malcolm's presentation of the Alfven Prize Lecture in Barcelona, Spain, where we each received the prize June 2005

NOMENCLATURE

ACCMOR	Collaboration
AK	Anode Cathode
APS	American Physics Society
BNL	Brookhaven National Laboratory
CDR	Collision-Dominated regime
CERN	European Organization for Nuclear Research
CL	Compound-Lens
CP	Charge conjugation-Parity
CPD	Cherenkov Photodiode
DA	area-weighted dose integrated over the forward hemisphere
DH	Dynamic Hohlraum
DOE	Department of Energy
EPA	Extended Planar-Anode
FB	Free Bound
FFA	Filtered Fluorescer Array
FFPHC	Fast Framing Pin-Hole Camera
FWHM	Full-Width-Half-Maximum
HELIA	High-Energy Linear Induction Accelerator
HEP	High-Energy Physics
IA	Indented Anode
ICF	Inertial Confinement Fusion
IFR	Ion Focus Regime
ITS	Integrated Tiger Series
LANL	Los Alamos National Laboratory
LAMPF	Los Alamos Meson Physics Facility
LLNL	Lawrence Livermore National Laboratory
MABE	Meg-Amp Beam Exp.
MAGIC	PIC electromagnetic code
MCNP	neutron Monte Carlo transport code
MIT	Mass. Instit. of Tech.
MITL	Magnetically Insulated Transmission Line
MS	Magneto-Strictive
NRL	Naval Research Laboratory
NYC	New York City
NYU	New Your University
P	Parity
PBFA	Particle Beam Fusion Accelerator
PCD	Photo-Conducting Detectors
PIC	Particle in Cell
PRS	Plasma Radiation Source
PSI	Pulse Sciences Inc.
PST	Pulse Shaping Target
QM	Quantum Mechanics
REH	Radiation Exit Hole
RMHD	Radiation Magneto Hydro-Dynamic
RT	Rayleigh Taylor
SGC	Short Gas Cell
SNL	Sandia National Laboratories
SPD	Scintillator Photo-Diode
SPEED	Short-Pulse Experimental Electron-Device
SWH	Static Wall Hohlraum
TIP	Total Immersion Particle
TLDs	Thermo-Luminescent Dosimeter
UC	University of California

1. INTRODUCTION

In the last few decades Sandia has successfully produced two unique pulsed-power accelerators, HERMES III [1] and Z [2] for the study of nuclear radiation effects, and for ICF (Inertial Confinement Fusion) in the laboratory [3], respectively. The heart of each accelerator is the mechanism that converts the generated electrical power into radiation. In the case of HERMES III, it is an electron beam diode, and in Z, initially, the implosion of wire arrays to form an axial Z pinch. At Sandia I have been responsible for developing the HERMES III diode, and later the discovery that stabilized wire-array z pinches enabling their application to ICF on Z. There I contributed to the understanding of one of the ICF concepts, the DH (Dynamic Hohlraum), and uncovered the mechanism behind the unexpected axial radiation asymmetry measured.

This report is a history of the science and technical issues behind these developments from a personal perspective. It is somewhat tutorial in nature in that the science necessary to understand some of the issues is also explained. The manuscript complements that told by Anne Van Arsdell in her manuscript *"Pulsed Power at Sandia National Laboratories--the first 40 years*" [4], and Neal Singer's book *"Wonders of Nuclear Fusion--creating an ultimate energy source"* [5].

Secondly but importantly, Sandia provides opportunities for a physicist to develop and evolve into a scientific leader in areas that are not necessarily taught in many graduate schools, but are of benefit to the nation. What follows then is a description of how that process worked for me developing the HERMES III diode, the z-pinch breakthrough, and the latter's application to one of the loads being considered for ICF--the DH. My hope is that some of my experiences and lessons learned will benefit others. The path to meaningful contributions to science is winding, but with tenacity and vision one does find a place.

Briefly, my career at Sandia evolved from my start as an experimental particle physicist into that of an intense electron-beam and plasma physicist. In my formative years, I was fortunate to be associated with key scientists that help set the stage for the current understanding of elementary particles. After this rigorous apprenticeship, Sandia offered me the opportunity to develop the Hermes III electron-beam diode, which enabled world record radiation-fields to be generated for the simulation of nuclear radiation effects. Later, following my sharpening instincts, I discovered the key to stabilizing imploding z-pinches, which led to a renaissance in z-pinch ICF. In all cases, Sandia provided the framework and sufficient resources to do quality R&D. Here, some of the techniques and

insights uncovered, and the colleagues who helped to achieve these successful outcomes are mentioned. I show the excitement of solving difficult problems together with ones collaborators. Finally, looking back over the road taken, I conclude with wisdom learned.

Before we start, my early training is mentioned, because it has had a profound effect on my approach to experiments, including the importance of including theoretical collaborators, and my reasons for coming to Sandia. Those readers interested only in the evolution of the HERMES III diode or z-pinch ICF development with the DH, may skip to the relevant sections without loss of continuity. An associated bibliography is included for those interested in more of the technical details then offered here.

The remainder of the report is divided into four main sections. In the first titled EXPERIENCE, my early training up to a few initial pulsed-power experiments at Sandia is discussed. In the second, titled HERMES III R&D, the initial research leading to the HERMES III baseline diode is discussed followed by a discussion of diodes having capabilities that improve downstream radiation fields, as well as, improving subsequent beam propagation in long drift cells for needed transport to an outdoor test cell. In the third, titled Z-PINCH ICF, the breakthrough stabilizing wire-arrays for z-pinch ICF, and its application to the SWH (static-wall-hohlraum) concept is discussed. In the forth, titled DYNAMIC HOHLRAUMS, the dynamics of the DH together with the experiments and modeling that unraveled the unexpected measured up-down axial radiation asymmetry is discussed. A CONCLUSION summarizing the discussions completes the report.

2. EXPERIENCE

2.1 Early Period

Interest in science was stimulated at an early age by my father who introduced me to the joys of understanding nature through observation. As a physical chemist, he tried first to interest me in chemistry by buying me an elementary chemistry set. However, to me it seemed like cook-book stuff and was of little interest. Later, he introduced me to the fun of amateur radio. By the age of 13, I was sufficiently motivated to get the General License (W7CFG), and to build a transmitter. In the process, I became fascinated with electronics. Dad taught me every thing from Morse Code to calculus. This led to an interest in microwaves and Maxwell's equations. As a junior in High School, I developed a project for the King County Science Fair that connected the measurement of dielectric constants using microwaves, with an interpretation by Maxwell's equations. The equipment, which included sliver-plated wave guides and klystron tubes, was scoured from used radar equipment at the Bremerton Naval shipyard for 10 cents a pound, just a short ferry boat ride from Seattle where I grew up. Luckily, I won first prize, and a 10-day trip to see science in the Navy (Fig. 1). As a result, by the time I left high-school, I knew that I wanted to be a physicist. Moreover, that to be a physicist one needs a solid foundation in mathematics. This set my life course.


THE SIXTH ANNUAL

KING COUNTY SCIENCE FAIR

STUDENT UNION BUILDING AND PIGOTT AUDITORIUM
SEATTLE UNIVERSITY
900 BROADWAY, AT MADISON

MARCH 17, 18, 19, 1961

Tom Sanford, First Prize Winner of Fifth Annual King County Science Fair, explains the fruits of his genius to Rear Admiral Frank T. Watkins, Commandant 13th Naval District

I recommend that talented young people make their lives an adventure of the mind.
HYMAN G. RICKOVER,
Vice Admiral, USN

The future of our Country depends on the young people—especially those who will man the frontiers of science.
FRANK MCLAUGHLIN

Fig. 1 Tom Sanford presenting his Science Fair Experiment to Admiral Frank Watkins at the Seattle King County Science Fair 1960.

2.2 Education

I entered the University of Washington in 1961, majoring in physics and mathematics. In 1965, I graduated magna cum laude with both degrees, being also elected to Phi Beta Kappa and Pi Mu Epsilon fraternity. This gave me the credentials to enter one of the better grad schools. However, I did not know what subfield of physics to pursue, let alone what university to attend. Columbia accepted me with a full fellowship, with MIT and UC Berkley offering teaching assistantships. Going to the east coast seemed like a grand adventure, but which

of the two schools? Prof. Fred Schmitt, my QM (quantum mechanics) teacher, said he loved NYC (New York City) and disliked Boston. That was how the decision to go to Columbia was arrived at. Besides it was a full scholarship.

I remember my first interaction with my advisor Prof. James Rainwater (Nobel Prize Laureate). Looking at my transcript, he said “what do these As mean? Here at Columbia an A is tough to get.” Well I was quickly put in my place. Then I learned that getting in was only the first step in the doctoral program. At the beginning of the second year there was a "qualifying" exam. As Prof. Polycarp Kush (another Nobel Laureate) said to us when we sat to take the 3-day exam, “look to the right and then the left, only one of you will be here next year”. After a follow-up oral exam with the future Nobel laureate Prof. Jack Steinberger and two others, designed to firm up the faculty decisions made, I finally received a small letter in the mail from Prof. Carlos Wick (author of the Wick Theorem and later my QM teacher) indicating that I had passed. What a relief!

Now in the club, what field of physics to enter? A trip to Columbia's Nevis Cyclotron Laboratory, about 20 miles north of the city, on the former estate of Alexander Hamilton, over looking the Hudson river, convinced me that I wanted to be a high-energy physicist. This was heady times for particle physics. New discoveries were almost being made daily. The anti-proton, anti-deuteron, the muon neutrino, the K-long, P (parity) violation in weak decays, CP (Charge conjugation-Parity) violation in neutral kaon decays all had been found in the previous half-dozen years, and Columbia was at the heart of many of these Nobel Prize discoveries. The symmetry and structure of mater was being pealed apart by high-energy particle accelerators. This is where I wanted to put my talent.

Prof. Leon Lederman, then director of Nevis and later of Fermi Lab and a Nobel Prize winner, was a key player in this expanding frontier, and was willing to take me on as one of his grad students. With guidance from Prof. Alan Sachs, I got my feet wet developing and designing Nevis's first MS (Magneto-Strictive) spark chambers, which would later be used in my thesis experiment (Fig. 2).

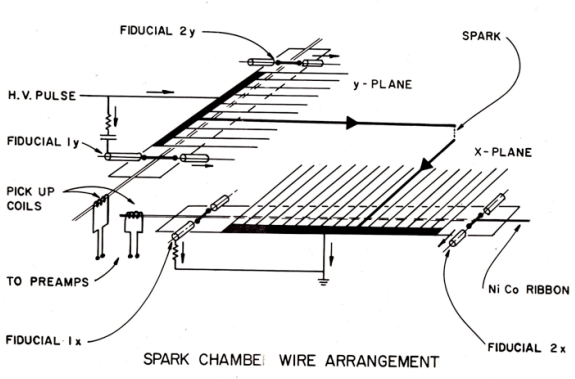

Fig. 2 Wire spark chamber.

Before I got there, Leon suggested I explore the ins-and-outs of the new MWPC (Multi-Wire Proportional Chamber) that Dr. George Charpack had developed at CERN (European Organization for Nuclear Research). (He

later received a Nobel Prize for his work, which revolutionized the speed which particles in HEP [high-energy physics] experiments could be detected and recorded.) A long training in experimental detector development and exploring proposals led finally to a suggestion for a thesis experiment in 1969.

At that time, Leon had returned from CERN after hearing a lecture on the discrepancy of the Lamb Shift with measurement, which could possibly be due to the proton having a small amount of its charge extending to a large distance from its central core--in short the proton may have a *halo*. He suggested measuring the outer charge radius of the proton using muon's from the Nevis cyclotron, by scattering muons from a hydrogen target. Muons were ideal because the heavy mass of the muon eliminated bremsstrahlung corrections to the scattering process relative to electrons. Electrons had been used to measured the radius of the proton earlier at the Stanford Linac, but not the outer radius with the precision needed, because of the large bremsstrahlung corrections. Within a short time I developed the concept, with Leon's input, for a scattering experiment, using MS spark chambers, to measure the incoming and scattered trajectories of muons from the outer region of the proton (Fig. 3).

There was significant development work that was required to produce the necessary 195-MeV/c muon beam and scintillation-counter trigger, needed to separate the weakly-interacting muons from the strongly-interacting pions produced from the cyclotron. Decay of the pions give rise to the muons in the

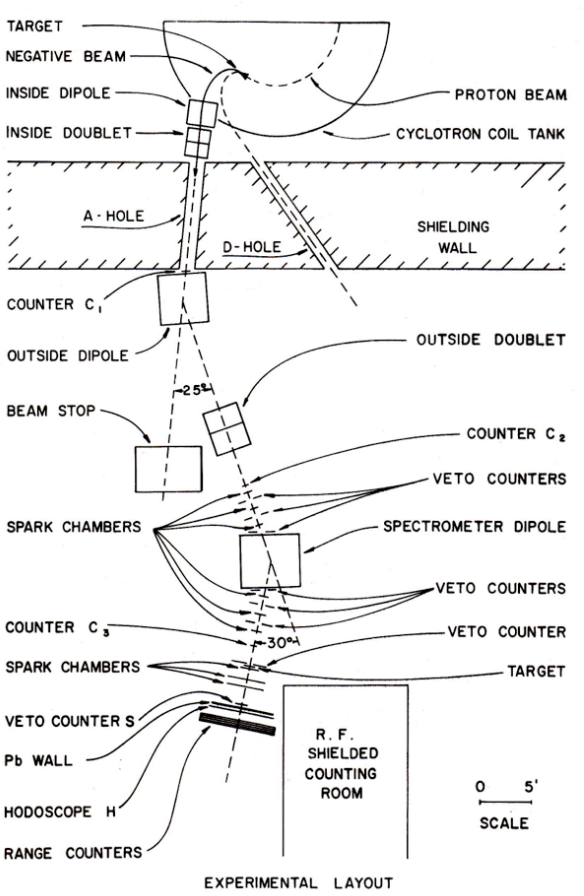

Fig. 3 Proton-Halo thesis experiment at Nevis Laboratory.

first place. Additionally, a new data acquisition system was required to handle the high event-rate expected from the counting room to the IBM 360 model 44 computer in the next building, far from the radiation field. After giving an in depth briefing of the proposal to faculty and outside users, the experiment was approved late 1969.

Construction of the chambers started immediately. I had thought of a cleaver way to save money by imbedding the Ni Co MS ribbons in the G-10 wire chamber frames itself (Fig. 2). Before fully testing the concept, I had all 9 chambers build with this *improvement*, being absolutely confident that by symmetry this would work. Well, the 1/4 inch frames were too thin and the MS signals at crossing points interfered with one another. Fortunately there was an easy fix. *But this near disaster taught me to always test an innovation before mass producing it.*

The liquid hydrogen target was again an other matter. Such targets had been built at BNL (Brookhaven National Laboratory), but never at Nevis. When it arrived for installation, its structure was a foot higher than the beam line. Leon observed that if we reverse part of the structure it would just fit. The hydrogen cryo-system, however, was found to have solder in its lines. There was no time to fix the problem and complete the experiment before the accelerator was scheduled for its planed upgrade in 2-3 weeks. Leon quickly made the decision to rip out the target and associated pluming, and to replace it with a plate of pure graphite. We would search for the halo on protons within the carbon nucleus. This then became my thesis. *This taught me, if possible, not to rely entirely on a new technology, leaving room for a backup in case it fails.* Years later at Sandia, you will see how this philosophy saved my first wire-array experiment.

A few more points. We set up many independent checks that proved that we could measure the muon momentum and scattering angle with the absolute precision required, such as measuring the known pion-decay spectrum and establishing the consistency of the results using differing target thicknesses and geometries. The purity of the muon signal was established by redundancy in the time-of-flight trigger and consistency with an independent range-chamber. Importantly, Leon showed, by example, the attention to detail, persistence in verification, and the unlimited enthusiasm required to run a successful experiment. He was inspirational. For example, while he was helping out with this experiment by running night shifts, he would drive to BNL the following morning, to run his now famous di-muon experiment that almost saw the J/Phi particle.

With the data in the bag, I spent the next year writing fortran programs to analyze the data, extracting limits on the proton *halo*, and showing that muon-electron universality still held in this low momentum-transfer region. By the end of 1972, I had completed my thesis, passed my thesis defense, wrote up the experiment for publication in Phys. Rev. C, where it was published September 1973 [6].

I have spend time discussing these early events, because they have

influence *my own style at Sandia, which consisted of combining theoretical motivation and analyses with experiment, and multiple checks with redundancy.* Columbia exemplified the success of this approach with the many Nobel's generated often inspired by the close relationship between the experimental and theoretical professors.

2.3 Post Doctoral Experience

I had just finish four years as an under grad, going to summer school as well, and now seven years getting a PhD. I needed a change. A post doc position at Rutherford Laboratory in England for a few years was a possibility. Aside from working at England's highest energy physics lab, this provided the break I needed for some traveling in Europe. At Rutherford I became part of a large team, under the leadership of Gordon Walker (later Director of Rutherford), to study the formation of new resonances in the neutral kaon-lamda system, produced by the collision of pions on protons over the range 1.4 to 2.4 GeV/c, with now an operational hydrogen target [7]. The talent I brought was knowledge of MS spark chambers and MWPC for the hardware being built, as well as data analyzing skills. Within two years the opportunity to continue in a international team at CERN presented itself. Prof. Samuel Ting of MIT was looking for post docs to join one of his small groups working within the team, on a recently approved experiment at the CERN ISR (Intersecting Proton Storage Rings). The experiment was designed to verify if Feynman Scaling was valid over the range 23- to 63-GeV in PP collisions, by measuring the spectrum of low-momentum pions produced in the central collision region. This was cutting edge science on the worlds most energetic proton collider. So I picked up and moved to Geneva, accepting a new post doc position at MIT. My knowledge of MWPCs and pions from Nevis was instrumental. At MIT I learned how to debug and setup the digital system used to store and convert the MWPC signals to a PDP6 in the control room 10-m above our PP intersection region. Analysis showed Feynman Scaling was seriously violated contrary to expectations [8].

There was never a dull moment working for Sam. At the spur of the moment, for example, I was asked to fly to BNL to help with his di-electron experiment [9]. The di-electron experiment was similar to Leon's earlier BNL experiment, but with improved spatial and momentum resolution on the leptons. The motivation for both experiments was to search for vector bosons (the Z and Ws) postulated to mediate the weak decay. As we know now, the energy of both experiments was too low. Nine years later, vector bosons were discovered by Prof. Carlos Rubbia's team on the proton anti-proton collider at CERN, having masses of 91 and 80 GeV, respectively. For this discovery, he

shared the Nobel Prize. Meanwhile at BNL, Sam's experiment, showed an unexpected narrow-resonance at 3.1 GeV in the electron-positron mass spectrum. Now called the J/Phi. It was unlike any other resonance, because of its narrowness. Analysis showed it to be a composite of a new quark (called charm) revolving around its anti-quark. This observation proved convincingly the existence of quarks, and was called the November 1974 revolution. Its simultaneous discovery by Sam's group at BNL and Prof. Burt Richter team looking at the inverse process at the Stanford Collider, resulted in a Nobel Prize for both men.

Despite the excitement of being involved with the Nobel Prize experiment and related work, such as the magnet design of another di-muon experiment for the ISR [10], I was not making progress in obtaining a faculty position. Prof. Jim Christenson, who was on the original Nobel wining CP violating experiment, was developing a high-energy physics group at NYU (New York University). We knew each other well from Columbia days. He offered me yet another post doc position at NYU, working on a experiment at BNL to better measure a key CP violating parameter in neutral kaon decay. Importantly, this held out the opportunity of eventually becoming a faculty member.

After three years, this was not to be the case. In the process I learned a great deal of physics and had the excitement of measuring the CP violating parameters in neutral kaon decay and experiencing first hand the quantum interference of the K long decay with the K short decay that violated CP symmetry; the mechanism possibly behind why we live in a matter universe and not one with both matter and anti-matter [11,12].

These were tough times to find an acceptable academic job. Not sure how to proceed academically and still wanting to exploit by skills as a particle physicist, I managed to secure another three-year contract returning to CERN, this time being employed by the Max Plank Institute in Munich. The 15 member German group I joined was part of the larger ACCMOR Collaboration: Amsterdam-Bristol-CERN-Cracow-Munich-Rutherford (Fig. 4).

Fig. 4 ACCMOR collaboration meeting at Schloss Ringberg near Munich 1980. Tom Sanford at bottom left.

It was a delight to be working again with many of my former Rutherford and CERN colleagues.

The collaboration was loosely organized and was a pleasure to work in. We all found our area of interest and

contributed accordingly. Because I came into the collaboration after the hardware was under construction, I concentrated on analysis of the data being generated. All 50 of us shared in the day-to-day running of the experiment and had specific equipment responsibilities. For example, one of mine was to tune the 120- to 200-GeV pion beam incident on our tiny Be target. The beam line was kilometers long, filled with hundreds of bending and quadrupole magnets that brought the extracted pion beam generated at the underground SPS (Super Proton Synchrotron) proton target to our Be target. The experiment was designed to produce and study the decay modes of possible D mesons in pion collisions with the nucleons in the Be target. Such mesons were predicted to be made up of the newly discovered charm quark and a normal up or down quark.

It was the toughest experiment I had ever worked on. For a year of solid data taking we saw no evidence of the D, only background. Eventually, with the right set of data cuts a small statistical D signal emerged. In this analysis, I played a significant role and earned my stripes. Out of $4x10^9$ triggers we found ~50 D mesons. Such mesons had been searched for in Sam's lower-energy 30-GeV proton on Be experiment at BNL that I had been associated with earlier, but with no success [9]. Here with shear fortitude and dogged determination and trust in our approach we proved the existence of the D and then determined its decay modes for the very first time [13,14]. *We had built new matter out of the newly discovered charm quark!*

Obtaining a real tenure position at a University was becoming problematic. I made a month-long coast-to-coast trip to America in 1979, giving lectures on our CP violating BNL experiment, to seriously look for a faculty position. Nothing of substance out side the usual offerings of Post Doc positions materialized. I had thought that continuing to work on cutting edge science at the best laboratories with some of the best researchers, that something would finally open up. This appeared not to be the case again.

In the mean time, I began to question the effort required to do this kind of research with so little near term pay-off to society. The gas shortages of the late 1970s and the need to find long term solutions to the worlds energy needs grabbed my attention. I thought that with my extensive technical background I should be able to make a contribution. In the summer of 1979, Prof. Richard Wilson of Harvard invited me to attend the Third International School on Energetics in Erice, Sicily, Italy, which was devoted to the subject Energy for the year 2000 [147]. The school brought together world experts in energy production from high-tech fast breeder-reactors to many forms of green energy production, with discussions of associated environmental issues, such as the consequences of the increasing CO_2 in the atmosphere and ocean. Sounds

timely now, does it not? It was an intimate atmosphere of a little over 30 students and teachers combined in a congenial setting, in an medieval town 1000 meters above the Mediterranean Sea. By the time the school ended I became excited that here is where I could usefully put my expert training. Now, how to get retrained and find a paying job was an other matter?

That year I made another month-long coast-to-coast trip to America, again giving lectures along the way at a number of universities. This time, however, stops at many National Laboratories engaged in both HEP as-well-as energy research were included. Returning to Geneva I found I had a number of serious job offers that included tenured staff positions at Fermi Lab, LANL (Los Alamos National Laboratory), LLNL (Lawrence Livermore National Laboratory), and Sandia among others.

For a continued career in particle physics, Fermi Lab was the obvious choice. Leon had called me and made an offer hard to ignore. But I had found that the environment where I lived and worked had became almost as important to me as the job. There were no mountains in Illinois. There were at Los Alamos, including a nearby ski area. At Los Alamos many groups offered me positions. Deciding to continue my particle physics career, I joined the meson-physics team at Los Alamos to promote the construction of LAMPF II (Los Alamos Meson Physics Facility), a high-intensity kaon factory.

I set up workshops, inviting physicists from all over the country, to study the possibility and help to promote the project, and design a possible experimental program. I myself looked into the new physics that could be done in the areas of rare kaon-decays and hyperon production, writing a number of detailed reports [148-150]. In a few months I came to the conclusion that this research could equally well be addressed at Fermi Lab or BNL, if there was sufficient interest, by simply building a new high-intensity kaon-beam line. The beam line would be a fraction of the $500,000,000 that LAMPF II was projected to cost. Moreover, there appeared to be insufficient physics interest in building such beam lines at either lab. I thus came to the conclusion that this project to keep LAMPF alive would not happen, and became concerned that the wrong decision had made. The position at Sandia was still open, which I took.

2.4 A New Start

On one of my lecturing trips westward, I saw a poster at the Albuquerque airport showing a picture of Sandia's PBFA I. PBFA I (Particle Beam Fusion Accelerator) was being developed to produce fusion energy in the laboratory, a potentially clean energy source for mankind. This was the first I

ever heard of Sandia, let alone this approach to fusion energy. This intrigued me, so during my hunt for a permanent job I sent a letter of enquiry along with my resumé to Sandia.

At that time Wendland Beezhold was building up his radiation effects group to help design and support the development of high-current and high-voltage electron accelerators to simulate the effects of nuclear weapons in the laboratory, using bremsstrahlung radiation from intense beams of electrons. My letter caught Wendland's attention, firstly I think, because I had attended the same Roosevelt High School in Seattle as he had four years later. Seriously, however, the previous year Wendland had hired Jim Lee, who was an experimental HEP from Cal Tech and Fermi Lab. Jim had done well in his group. As a result, I was asked to come for an interview on my last trip across America, which resulted in a job offer.

Wendland pointed to a large patch of high desert, indicating that in a few years this would be transformed into a state-of-art nuclear radiation simulation facility, and I could be a major player in its evolution. The accelerator development required was similar to the technology being used at PBFA I. *Here then was the potential to learn a new technology that had application to ICF, which is where I wanted to be in the future.* I had to first learn the business, however, if I was going to make any contribution to ICF. Here was the door. Most importantly, Wendland turned out to exhibit all the characteristics I had come to admire in many of the great leaders I had the opportunity to work with.

Accordingly, when I saw that LAMPF II was unlikely to be funded (which turned out to be the case), I jumped at the second chance to learn a new field that had the potential to make a difference to the energy issue. In hindsight, I never had to looked back.

2.5 Early Pulsed-Power Research

Wendland's major responsibility was to have developed in Sandia's Nuclear Simulation Division within James Powell's Department, and in collaboration with Sandia's Pulsed-Power Department under Ken Prestwitch, the required radiation sources to be ready for installation in the late 1980s for the Nuclear-Radiation Simulation Laboratory. The laboratory was still under design when I joined Sandia in May of 1982. Two major accelerators were envisioned, one named Saturn, designed to simulate the environment of x-rays from a nuclear explosion; the other, named HERMES III, to simulate associated ɣ-rays. A new fusion pulsed-power accelerator (PBFA II), was just coming online, which meant that PBFA I was available. Calculations showed that the conversion of the high-current, low-voltage PBFA I to an x-ray generator would be ideal to meet the requirements of Saturn. Diode development, however, was needed to

convert the electrons to the necessary x-ray yield and pattern. The case for the ɣ-rays was not quite so simple. In contrast to the x-rays being produced by MeV electrons, as available in PBFA I, bremsstrahlung ɣ-rays require electron energies an order-of-magnitude higher. This meant both the development of a new accelerator, as well as, diodes to convert the electron energy to the desired radiation pattern.

2.5.1 Frustum Diode

One x-ray diode that was under early consideration was the 18-blade Frustum Diode, suggested by Pace VanDevender, Director of the Fusion Program and later Vice President of Research at Sandia. Jim Lee graciously transferred the project over to me, where I became responsible for its continued development on the 1-MeV 2-MA accelerator SPEED (short-pulse experimental electron-device) [151]. Here, I got my training in Pulsed-Power Technology working closely with Phil Spence at PSI (Pulse Sciences, Inc, San Leandro, California). Phil was one of the pioneers in the field, and became my mentor. Although the design proved feasible [15], an alternative diode, consisting of concentric annular rings, was chosen, for its simplicity.

2.5.2 MABE

MABE (Meg-Amp Beam Experiment) was a prototype accelerator for the ɣ-ray requirement [152]. It consisted of nine electron-beams, each being generated in a foilless diode fed by a common driver. The beams were transported in vacuum through three post-accelerating gaps, and magnetically bent inward to bremsstrahlung targets to create the desired radiation pattern.

On MABE, I showed that, combining radiation measurements with simulations of electron flow incident on the target with simulations of the subsequent electron-photon transport in the target, provided a powerful tool in estimating electron angles and corresponding beam temperature [16]. The electron-flow calculations were done by Jim Poukey using the PIC (particle-in-cell) electromagnetic MAGIC code [17], and those of the subsequent electron-photon shower in the target were done by John Halbleib, using his Monte Carlo ITS [18] code. Both codes were state-of-art programs that had been developed at Sandia. Jim was in Ken Prestwitch's organization and John in Jim Powell's. Over the next decade, these two well-known theorist, together with Phil Spence, became my close associates in all my pulsed-power research. My earlier experience in developing personal skills working in both small and large groups helped in facilitating this successful and delightful collaboration in association with our other colleagues among differing departments and divisions.

3. HERMES III DIODE R&D

3.1 HELIA test bed

An alternative accelerator to the complexity of MABE, was HELIA (High-Energy Linear Induction Accelerator) [19]. In HELIA, the outputs of four induction cavities are fed into a MITL (magnetically-insulated transmission line) and an electromagnetic wave is repeatedly voltage amplified in four stages along the length of the MITL, producing a 3-MV, 150-kA electron beam incident on an anode target (Fig. 5).

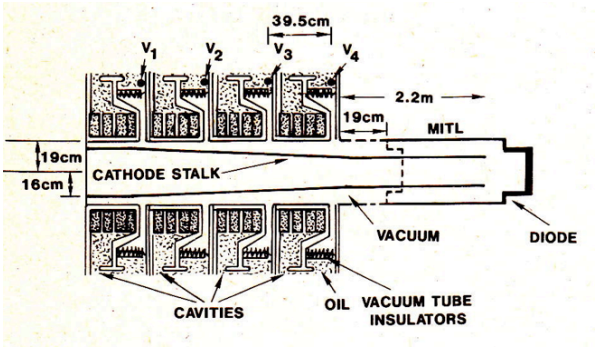

Fig. 5 HELIA showing the diode connected to either 19-cm or 2.2-m configuration. V1, V2, V3, V4 are capacitative voltage monitors.

In contrast to MABE, the pulsed power in HELIA performed beautifully. The concept was an elegant innovation developed by Sandia's Juan Ramirez and Pulse Sciences. Because of its reliability, Ken Prestwitch, made the tough decision to drop the MABE approach (in which much effort had been placed) and to back the novel HELIA design to generating the necessary radiation fields for HERMES III. *At this time, however, no one knew how to build a suitable diode that would both be matched to the impedance of the accelerator and create the desired radiation field!* As a result of my experience on MABE and with the Frustum Diode, Juan suggested that the diode became my responsibility. Agreeing, I quickly put a team together (Fig. 6) to explore diode possibilities, first on HELIA, before latter adapting them to HERMES III.

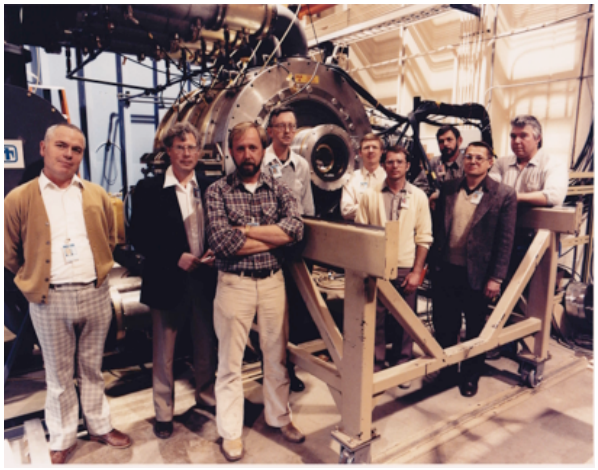

Fig. 6 HELA diode team, from left to right: John Halbleib, Tom Sanford, Chuck Heath, Jim Poukey, Tom Wright, Ray Mock, Dave Knott, Bob Craven, and Adam Chaves.

Jim Poukey's computer simulations of the electron flow in the AK (anode cathode) gap at the HELIA exit, just like at a MABE target, showed that the beam forms a weak pinch, due to shorting of its radial electric-field at the target [155]. This pinch produces an undesired nonuniform radiation pattern downstream, forming a hot spot on axis. By indenting the anode, the radial electric field is increased and the beam can be

made to impact the target at more shallow angles, producing the more uniform and forward directed radiation pattern desired (Fig. 7). Moreover, the advantage of this scheme over that of a planar anode is that the diode impedance, pinch angle, and radial impact position at the anode can be partially decoupled [155]. The concept proved to be a success on HELIA. I named the diode the IA (Indented Anode) diode [20].

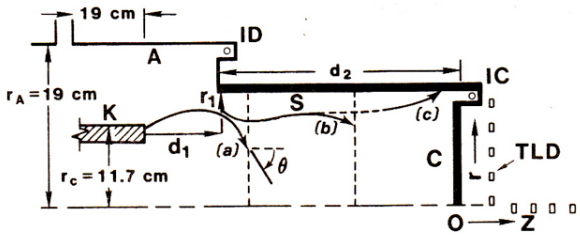

Fig. 7 HELA indented-anode diode. Arrows show electron path for each of three converter (C) locations.

By extending the anode we showed that the IA diode operates in either a *load* or *line-dominated* regime [21], depending on AK gap spacing. In the *load-dominated* regime, which corresponds to to small AK gaps, the diode impedance is controlled by an effective AK gap, and the flow is approximately axial. In the *line-dominated* regime, which corresponds to large AK gaps, the impedance is independent of the AK gap and corresponds to the impedance associated with the minimum current-solution of the MITL, with the flow becoming more radial as the AK gap is increased (Fig. 7). At vary large gaps, the diode is referred to as the EPA (Extended Planar-Anode) diode when the indentation is removed.

In all cases, detailed measurements confirmed our semi-empirical impedance and radiation models. *The modeling and measurements disproved the previously held view that the diode impedance would increase indefinitely for large gaps.* I was now bringing the kind of rigorous science I grew up with to the arena of diode physics at Sandia. These experiments were Nevis size and a shear delight to develop.

We had time to explore another option, before a diode design needed to be finalized for HERMES III. A third concept tested was the B_θ lens diode (Fig. 8).

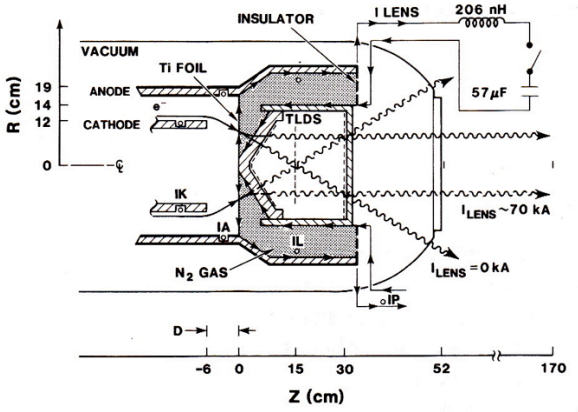

Fig. 8 HELIA B_θ lens diode showing average electron and radiation trajectories with no current and 70 kA in the lens.

The lens actively controls the electron beam as it passes through a charge-neutralizing gas cell filled with an imbedded B_θ magnetic field [22]. In

contrast to the IA or EPA diodes, which only passively control the beam, the B_θ lens diode produces better radiation uniformity, for less beam loss. It generated an incredibly uniform pattern, but now at the expense of the complexity of the external magnetic field.

The high currents were measured using, self-integrating Rogowski coil segments, current shunts, or B-dot monitors. The high voltage was measured directly using resistive voltage dividers and capacitive voltage monitors where possible, and was reliably inferred at the diode using currents measured in current shunts (developed by PSI) along the cathode and anode surfaces of the MITL together with John Creedon's para-potential flow theory [23]. These were standard techniques, save for the latter. The absolute maximum voltage, was confirmed with a range-filter that used CR-39 film to record the number of protons transmitted through Al foils of varying thickness. The protons were generated at the anode (which in large numbers could short-out the radial electric field) and accelerated toward the interior of the hollow cathode, where the filter was positioned. In the small numbers measured here, they provided a novel diagnostic. The range-filter technique had been pioneered by Bill Stygar and Ray Leeper for use in PBFA I.

Measurement of the electron distribution at the target was measured with 4-chlorostyrene radio-chromic film [24] and segmented graphite calorimeters. The downstream spatial radiation pattern was measured with arrays of CaF_2 TLDs (thermoluminescent dosimeter) and a p-i-n diode measured the temporal radiation pulse on axis. In the simulations, the steady-state electron flow in the AK gap at 3 MV (peak power) as calculated by MAGIC and the measured electron KE (kinetic energy) distribution was used as input to the ITS code, which tracked the electrons and calculated the resulting electron-photon shower in the target and TLDs. As with the impedance measurement-modeling comparisons, these measurements confirmed the simulation approach within the expected uncertainties and gave us confidence in using this approach, together with our impedance model, to design the HERMES III diode.

3.2 ITS Code Verification

Our radiation predictions were based on the ITS code calculations [25]. These had significantly differing spatial distributions than had been calculated from the empirical Charley Martin Equation [26], which was used earlier to estimate the voltage and current requirements needed for HERMS III. Moreover, ITS calculations were used to design the converter, the target that optimally converts the incident electrons to γ-rays. Accordingly, it was imperative to verify the ITS code calculations. This was done using the radiation from monochromatic pencil electron beams,

one at 0.75 MeV on the Sandia Pelletron [27], and an other on the Santa Barbara Linac, operating between 5 and 25 MeV in 5 MeV steps [28]. The measurements covered the entire forward hemisphere using a variety of electron equilibrated TLDs and absorber thicknesses. Corresponding ITS simulations agreed with the measurements over this entire range, typically within the 6% uncertainties of the measurements. We found that the Martin Equation provides a good description of the angular dose profile from an optimized target only for angles less than 15°, but significantly underestimates doses for angles greater than 15°. Moreover, use of the Martin Equation to calculate the DA (area-weighted dose integrated over the forward hemisphere) underestimates the actual result by a factor of 2.4. In the process we developed an improved Martin Equation [29], which can be used in lieu of expensive calculations to aid designers of flash x-ray facilities. As a by-product, the absolute comparisons made provided an independent check on the validity of the Sandia TLD lab calibrations used in the high-energy photon fields characteristic of HERMES III.

3.3. Electron Energy Deposition Limit Established

A killer in any diode concept was the creation of ions at the anode surface, due to the thermal desorption of adsorbed gases. These ions can short-out the radial electric field (like what occurs naturally as an electron beam approaches any anode as mentioned earlier) and cause the electron beam to pinch destroying the uniform radiation pattern desired. Accordingly, I put a great deal of effort on HELIA into determining what was the maximum electron energy density we could get away with at a target before ions were created. Thus we knew the bounds we needed to stay within on any HERMES III design. In case we had an unexpected problem, our measurements showed that we could replace the front surface of the target, normally made of Ta to maximize the conversion of electrons to photons, with Ti or C, to gain a safety factor of 4 or 6, respectively [30].

3.4. HERMES III Baseline Diode

Estimates indicated that HERMES III (Fig. 9) needed to produce a ~20-MeV electron beam at the target on the order of ~700-kA in ~20 ns to produce the desired radiation dose rate of ~5 Trad/s over a useful area of 500 cm^2 [156, 25]. These electrical and radiation parameters became the HERMES III design goals. Based on our HELIA experiments and modeling, I felt that we could design a baseline HERMES III diode and target with confidence to meet the required radiation goal [155,156]. My choice was to use the simplest and most robust of the concepts, namely the EPA diode (Fig.

10). The two codes, MAGIC and ITS were again used extensively in the EPA design.

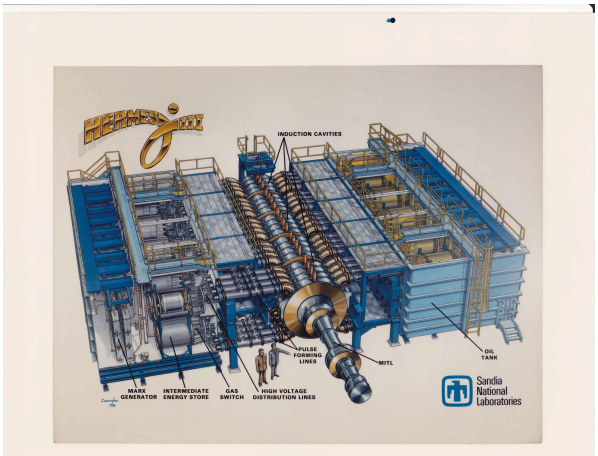

Fig. 9 HERMES III electron accelerator.

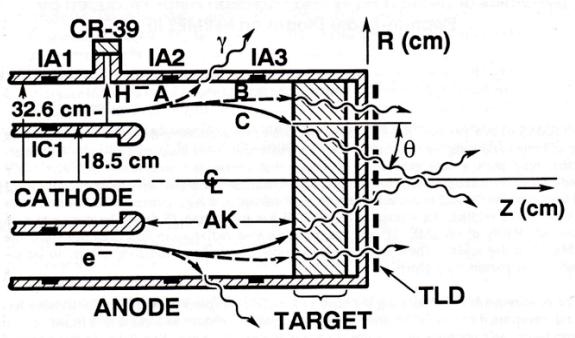

Fig. 10 HERMES III Extended Planar-Anode diode illustrating electron trajectories and radiation produced at (A) early or late time, (B) midway through the voltage rise or fall, and (C) peak power. AK gap > 50 cm.

I remember the day the first integrated accelerator-diode test came, February 26, 1988. Juan Ramirez, who was in-charge of the HERMES III design and construction felt that the 10^{-4} Torr vacuum so far achieved was sufficient to test the facility. I was apprehensive, because if the vacuum was not in the 10^{-5} range, where we usually ran our diodes, there was a likelihood that ionization of the residual gas could cause the beam to pinch at the anode. Before the shot, I remember Pace VanDevender asking me what the AK gap of the diode was. *"Almost a meter"* I replied. On HELIA our AK gaps were typically only a few centimeters, as had been Pace's experience as well. He was flabbergasted: *"are you sure this will work?"* I had confidence in our HELIA research, even though the extrapolation in voltage and current was 7 and 5, respectively. And I assured him with a solid *"yes"*. Well, as Juan expected, the shot went off with out a hitch and the accelerator performed beautifully. *Reading the TLDs placed on the downstream target face showed a different story for the diode. The radiation field indicated that the beam had severely pinched!*

Over the next few weeks, tests showed that the beam continued to pinch despite the fact that the quality of the vacuum improved past the 10^{-5} Torr range. I had faith in our design and its demonstration on HELIA. Something else was the problem! Subsequently, I found out that the crate containing the large heavy graphite target being used had been left out in the rain before being installed. The crate had leaked and the graphite likely contained moisture. This could easily explain why the beam

pinched. The incident beam would have heated any moisture creating ions. Extensive external heating of the target to drive out the moisture, however, had no effect on the quality of the beam. Likewise replacing the front surface of the target with a titanium foil had no beneficial effect. The beam continued to pinch and my migraine continued.

Then one morning, John Corely, one of Juan's chief technicians, came rushing in. He had found extensive electrical burn marks a half meter inside the front cathode tip of the MITL (Fig. 10), where a thick tantalum shield was placed to shield the forward current monitors from the high radiation field being produced. The shield had not been secured and was arcing. Ken Prestwich suggested that ions were being generated and being swept into the AK gap, resulting in beam pinch. This was the case. *The shield was removed and the beam immediately snapped into the calculated position and my migraine disappeared.* What a trial of development faith.

Subsequently, we quickly produced the required radiation pattern with a target optimized for radiation production, making HERMES III one of the most successful pulsed-power facilities completed at Sandia [32]. *The success of the facility (Fig.9), and in particular the diode (Fig. 10), was based on extensive computer modeling [155,156], pretesting on smaller devices, multiple and redundant diagnostics insuring that each of the many components worked as designed, and a dedicated technical staff (Fig. 11).*

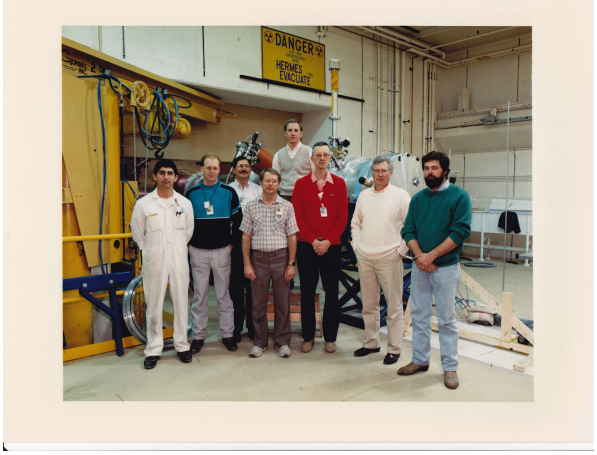

Fig. 11 HERMES III diode team, from left to right: Jimmy Flores, Fran Current, Gerry Crowder, Ray Mock, Todd Borkey, Jim Poukey, Tom Sanford, and Tim Sheridan.

3.5. Baseline Characterization

The early success of the program allowed time to fully develop techniques to characterize Hermes III as a high-power electron beam generator [33], as well as, a high-power radiation source [34], and to develop methods for controlling the beam to produce radiation fields for other useful applications.

For example, using the preliminary techniques explored on HELIA, we showed that when the diode was operated in the EPA mode (which became the standard operating mode for users of HERMES III) the diode is matched in impedance with the upstream MITL. About 75% of the electrons are emitted along the MITL. This sheath flow,

together with the shank flow near the tip of the cathode, leads to a well defined annular ring of electrons that flows towards the target (Fig. 10). As the voltage ramps up, this annular ring, which is formed from the electrons in the sheath propagating down the MITL toward the diode, sweeps radially inward at the anode, reaches a quasi-steady state near peak power, and the sweeps radially outward as the voltage ramps down. Additionally, an enhancement of electrons is formed on axis at the target. These electrons originate from the inside of the annular tip early in the pulse and remain for its duration.

At peak power, a total current of 693±12 kA at the diode with 190±6 kA in boundary current is measured. (The uncertainties refer to RMS shot-to-shot variation, unless other wise stated.) The corresponding voltage calculated from the measured current using para-potential flow theory peaks at 20.6±0.3 MV for a set of 20 shots. The peak voltage extracted by comparing the measured dose-area products in the TLDs located at the target with our model gives 18.1±0.6 MV. The measured range of measured H^- ions gives 18.5±0.6 MV Fig. 10). The absolute uncertainty on each measurement is estimated to be 5 to 10%. The measurements illustrate the stability of HERMES III between shots, as well as, the consistency among the three radically differing techniques for establishing voltage in this extremely hostile radiation environment, confirming the soundness of this unique design to meet the electrical goals.

In order to measure the temporal behavior of the radiation in both the near field down stream of the target, where dose rates are high, and the far field, where dose rates are low, we developed two types of detectors [35]. One is a CD (Compton diode) designed by Gary Carlson that is used with or without a collimator to control the radiation incident on its sensitive volume [36]. The other type is a photodiode that measures the light generated when the incident bremsstrahlung strikes a plastic scintillator or Lucite Cherenkev radiator [35]. These are standard techniques used in the HEP experiments that I had been involved with years earlier. The CD gives an electrical signal related to the rate of production of secondary electrons - especially Compton electrons - following interactions of the incident radiation. It is capable of operating at high dose-rates. It is low cost, requires no bias, and is mechanically rugged and was used in underground nuclear testing. In contrast, the SPD (scintillator photodiode) saturates at high dose-rates and is more complex, but provides a signal known to be proportional to dose rate with a high sensitivity making it suitable for measurements in the far field. The CPD (Cherenkov photodiode), on the other hand, had the potential for operation at high dose-rates without shadowing the downstream field to the degree the CD does. Like the SPD it is physically

smaller, so that it measures the radiation field with higher spatial resolution.

The measurements and modeling confirm the dynamics of the electron flow within the diode, which leads to the dependents of the temporal variation of dose rate on spatial location in the near field. All detectors show that the FWHM (full-width-half-maximum) of the dose rate pulse near the beam axis in the far field is 23.5±0.5 ns. In the near field, the FWHM decreases to 17.5±1.5 ns. The location of the minima corresponds to the maximum amplitude of the radiation cone at peak power. The exact shape of the radiation pulse is well predicted by our MAGIC-ITS modeling.

The target optimized for radiation production [37] was made of 305-μm thick foil of titanium, followed by a tantalum converter of 3.06-mm thickness, an electron absorber of 5.08-cm thickness of graphite, and an aluminum of 1-cm thickness that defines the vacuum chamber. The thin Ti foil minimized the probability of forming a beam pinch as previously discussed. (Please see Section 3.3.) The thickness of the tantalum and graphite were chosen to maximize the calculated radiation output, while still stopping the beam electrons. Measurements confirmed our calculations and showed the insensitivity of the forward radiation fluence to the thickness of the tantalum. The tantalum converter was made up of a stack of 51-μm-thick foils to lessen the chance of spallation. With well over 500 shots, neither spallation nor evidence of of anode plasma formation had been observed, with the target available for the next shot without damage. With this configuration, HERMES III could shoot repetitively at the rate of one shot per hour with out the need to open vacuum to replace the target.

Using this target operating at the exit of the EPA diode with AK gaps ranging from 40 to 100 cm, radiation fields of 5.6 Trad/sec to 1.2 Trad/s over useful areas (area where dose is greater than 50% of peak dose) of 700 cm^2 to 3100 cm^2 were achieved, respectively [38]. These fields exceeded our design goal and gave the added flexibility of enabling large-area exposures at high dose-rates as well. The extensive characterization of the radiation fields, with the radiation diagnostics developed, permitted test objects to be studied in well-defined and controlled environment with unique dose-rate area and volume products. This diode target arrangement became the standard operating point for the users of HERMES III.

3.6. Beyond HERMES III Baseline Diode

3.6.1. Short Gas Cell

By adding a gas cell between the anode and the radiation producing target we were able to produce record breaking radiation intensities without destroying the target, thus extending the capability of HERMES III (Fig. 12). The high electric

fields inductively generated by the beam rapidly ionize the gas, resulting in complete charge neutralization and nearly complete (>90%) current neutralization of the incident beam in the gas [39]. This neutralization results in

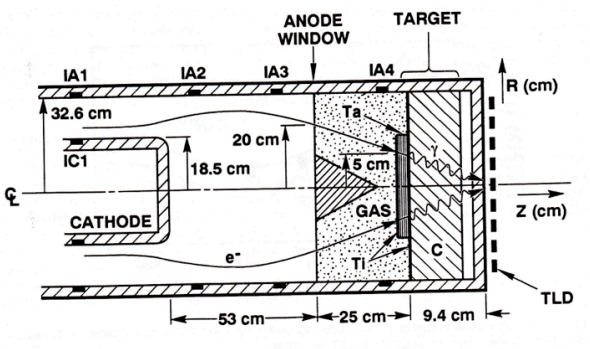

Fig. 12 HERMES III short Gas Cell diode in intense bremsstrahlung mode. IA1 through IA4 and IC1 are current shunts.

approximate ballistic propagation in short cells. The introduction of the gas cell thus permits the annular beam (generated in the diode) to impact the target at small radii, with little dispersion from self-fields [40]. With this design, the radiation dispersion at the focus is minimized and the high intensities are possible. Additionally, concern over forming an anode plasma that would lead to radial collapse of the beam at the anode is not an issue because the high surface deposition from the upstream beam occurs on the upstream surface of the target, which is inside the gas cell.

This configuration produced nondestructively peak doses and dose rates of 370± 60 krad and (3.5±0.7)x10^{13} rad/s over a useful area of 80 cm^2 [41], which are a factor of six and three time greater, respectively, than that achieved previously on HERMES II. HERMES II had held the previous record for dose-rate produced in the laboratory. Importantly, we showed that the standard TLD used to measure the radiation dose are shown to be dose-rate independent within ±15% up to these high levels.

The SGC (short gas cell) also provided a unique source of pulsed electrons. Again, the EPA diode is used to extract a large radius annular electron beam from the accelerator. The resulting beam is injected at a small angle into a low pressure gas cell of 3 Torr N_2. This pressure maximized current neutralization. As in the above gas cell, the beam propagates ballistically to a focus where objects can be placed for irradiation and study. This design is similar in concept to the very intense γ−ray focus discussed above, except here the focus is made with the primary electrons inside the gas cell. The configuration is capable of delivering energy depositions on the order of 200 J/g (20 Mrad) over useful area of 70 cm^2 and 4 cm depth in graphite in 25 ns, for example. Increasing the injection angle by reducing the AK gap permits higher dosed to be achieved over smaller areas. Such beams are of interest for the study of material property changes from high instantaneous energy deposition and for the study of the response of electronic components to thermal mechanical shock.

An other application of the SGC is for the production of a non destructible intense source of photo-neutrons [42]. Placing either natural lead of depleted uranium at the radiation focus of the high-intensity radiation source, 0.5 or $1x10^{14}$ neutrons in a 15-ns pulse from natural lead or depleted uranium, respectively, is produced. Here we showed that nuclear activation foils, which are often used to characterize the neutron spectrum from fast-pulse reactors, can also be used to characterize the neutron spectrum from pulsed electron accelerators, provided the flux is at least of the order of 10^{11} n/s. Importantly, we developed a steady-state numerical model of the source and showed that the model predictions of the electron, photon, and neutron fields agree qualitatively with those measured. The model included the inputs from MAGIC, ITS, and now MCNP (the neutron Monte Carlo transport code) [43] with a special algorithm [42] designed to convert the photons to neutrons for input to MCNP. The quality of the agreement suggests that the model can be used with confidence to predict photo-neutron production from other pulsed-power systems, particularly the 50-MV EDNA (Electron Driven Nuclear Assembly) being designed at Sandia by Jim Lee [44]. At this voltage, the neutron production from the incident bremsstrahlung is maximized. The success of our effort rested on the shoulders of both Jim Poukey and John Halbleib, but now also on the skills of Len Lorence who modified MCNP for the unique bremsstrahlung inputs, and John Kelly and Pat Griffin who were experts in measuring neutron fluxes using the activation foil technique.

A side benefit of the model was the development of yet another technique to measure the peak voltage of HERMES III over the range 10 to 20 MV, namely that from the photo-neutron fluence [45, 46]. Voltage extracted from our measured fluence using the model agreed to a precision of 5% with that measured from para-potential flow theory, the range of H^- ions and bremsstrahlung from the electron target, giving 18.7±0.7 MeV. Here the uncertainly is systematic.

3.6.2. Compound-Lens Diode

In the standard HERMES III operating configuration, which uses the EPA diode, the accelerator produces the most powerful source of flash x-rays in the world. However, the useful exposure volume that can be achieved in this configuration is limited by the excessive axial non-uniformity. This limitation occurs because the electron beam, as I have discussed, forms a weak pinch in the diode due to radial electrical fields being shorted at the target. The pinch, characterized by the pinch angle, θ, causes the radiation to be focused on axis, which leads to a pattern having non-uniformity with depth (Fig. 10).

The CL (Compound-Lens) diode is an alternative diode that significantly extends the capability of HERMES III beyond this limit (Figs. 13 and 14).

In the CL diode [47], the electron beam is made incident on a thin, conical foil window (305 μ of Ti) followed by a

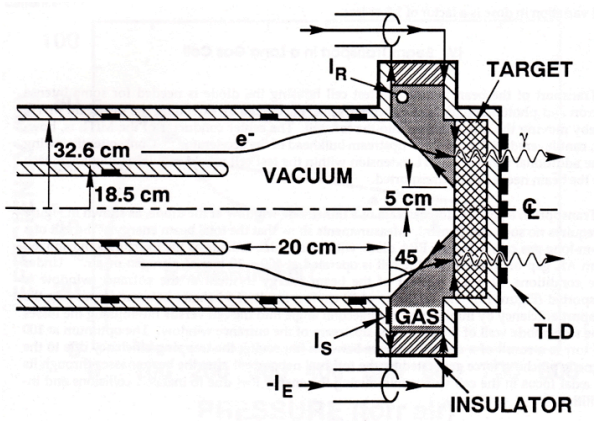

Fig. 13 HERMES III Compound-Lens diode. Is is a current shunt that monitors net current. Ir is a Rogowski coil that monitors the external current Ie.

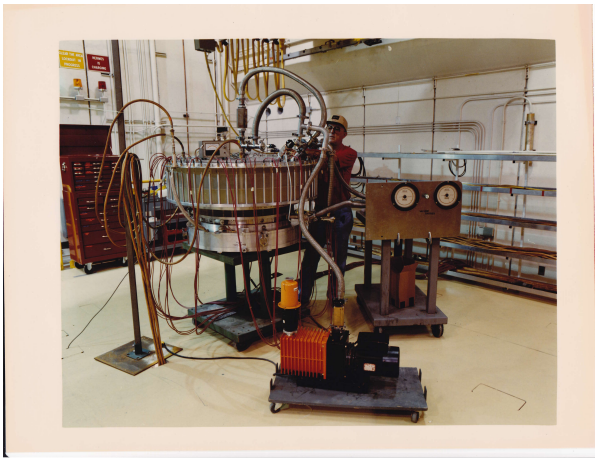

Fig. 14 Bill McAtee testing Compound-Lens diode.

low-pressure gas cell and bremsstrahlung target (Figs. 13 and 14). The gas (3 Torr of N_2, as in the above gas cells) provides rapid charge and current neutralization of the incident beam. When an external current Ie is applied across the lens, a B_θ field is generated. By adjusting the current, the beam can be made to impact the target at the desired small angle. Because the B_θ field decreases inversely with the radial distance from the axis, the curvature of the trajectories of the electrons at smaller radii is greater than at larger radii. Additionally, the angle of the electrons at the window increases with radial distance from the axis. By angling the entrance window of the gas cell at 45°, the electrons at larger radii remain in the magnetic field longer and the simultaneous effects of the decreased in field strength and higher injection angles at large radii are partially compensated. The MAGIC-ITS modeling shows that this compensation can be optimized, enabling the bulk of the electrons to impact the target with trajectories nearly parallel to the accelerator axis within the ±2° annular spread of the beam at a given radius for the geometry of Fig. 13, with Ie=112 kA. This condition of paraxial impact angles (θ=0°) approximately optimizes the uniformity of the radiation pattern and maximizes the dose in the far field [48].

Increasing the AK gap of the EPA diode increases the radius and simultaneously decreases the angle as discussed. This adjustment enables injection angles as low as 20° to be achieved before significant beam is lost to the side wall upstream of injection. This restriction in injection angle limits the subsequent transport efficiency

achievable in downstream drift cells, to be discussed shortly.

By tapering the Ti window at 45°, the electrostatic force generated between the conical surface and the beam in the AK gap reduces the pinch angle at the foil. This reduction is similar to that generated by introducing an indentation in the anode of the IA diode. The reduction decreases the external current required to achieve paraxial conditions. Relative to the 53-cm EPA diode, the conical surface reduces the average pinch angle at the anode from 32°±8° to 15°±4°, and the external current of 128 kA reduces the 15±4° entrance angle to 0±4° at the target. Because of the two-component mechanism for controlling the beam (electrostatic from the orientation of the conical surface and magnetic from the external current), I called the arrangement the compound lens [47].

Current is provided by a 6.4-kJ power supply with a 1/4 cycle rise time of 3.7 μs. The lens in conjunction with this supply provided robust operation with little damage except for electron bombardment of the Lucite insulator (Fig. 13). At early and late time, the low energy electrons are swept into the insulator. After 50 shots, significant damage to the insulator (Fig. 14) from the resulting dendriting had developed. Little damage to the insulator has been observed, however, subsequent to replacing the UV shield with a 2.52 cm thick annular ring of Lucite to absorb the low-energy electrons and by replacing the Lucite insulator with one made of cross-linked polystyrene. Under these conditions the insulator has accumulated over 350 shots. After 300 shots, however, breakdown across the absorber, between the windows, was found following passage of the beam pulse. Operation returned to normal after replacement of this inexpensive component (which now absorbs the bulk of the radiation damage).

A newly minted 100 element graphite calorimeter mounted adjacent the downstream face of the lens and which acted as a target, together with TLD arrays at the downstream target face and x-ray pinhole camera and a fast-framing ɤ-ray pinhole camera viewing the downstream radiation generated downstream of the target are used to estimate the time integrated and time dependent radial profiles, respectively, of the beam at the lens. The calorimeter was developed in collaboration with George Proulx at PSI, and the state-of-art framing camera was developed by Bill Stygar. Both instruments worked impeccably well with minimal background in the extremely high radiation environment generated.

As with previous comparisons, the MAGIC-ITS modeling provided an excellent comparison with the measurements when the parameters of the lens were varied, enabling a well define electron source to be setup for a given radiation exposure. The variations permitted the peak dose, useful area, and useful volume of irradiation to be varied

from 100 krad, 600 cm^2, and $20x10^3$ cm^3 to 20 krad, 3400 cm^2, and $200x10^3$ cm^3 in a 19 ns radiation pulse [48].

3.6.3. Long Gas Cell using EPA Diode Injector

In addition to these capabilities, versatile transport of the HERMES III beam within the test cell and to an out door test cell at the test cell exit, 10.8 m down stream of the diode, was required for intense electron and photon applications. Such transport is possible by extending the upstream MITL, thereby moving the beam-generating diode farther into the test cell. The center conductor of the MITL is, however, cantilevered 18.7 m from the upstream bulkhead of the accelerator (Fig. 9). Consequently, owing to the additional weight, extension within the test cell would require frequent, time-consuming realignment of the MITL.

Electron transport in a gas cell downstream of a thin anode window at the diode (similar to the above cells discussed, but now of considerable length) requires no such realignment. This technique is well known and has been used previously to transport lower-power electron beams. Preliminary computer simulations of the HERMES III beam using the IPROP code [49], by Dale Welch of Mission Research Corporation, indicated that such propagation should be possible within aluminum walled cells with modest radii, such as that with the outer radii of the HERMES III MITL filled with air. Specifically, he showed that the azimuthal magnetic field generated by the net current, defined as the sum of the incident beam and plasma currents in the gas, was sufficient to contain a substantial fraction of the beam as it propagates through the gas and that potential instabilities such as plasma two-stream (Fig. 15C), resistive hose (Fig. 15F), and hollowing (Fig. 15D) should not increase beam emittance to the point where significant beam losses to the side wall occur. IPROP is an electromagnetic PIC computer code that includes gas chemistry subroutines, which allow the scalar conductivity to be computed self-consistently.

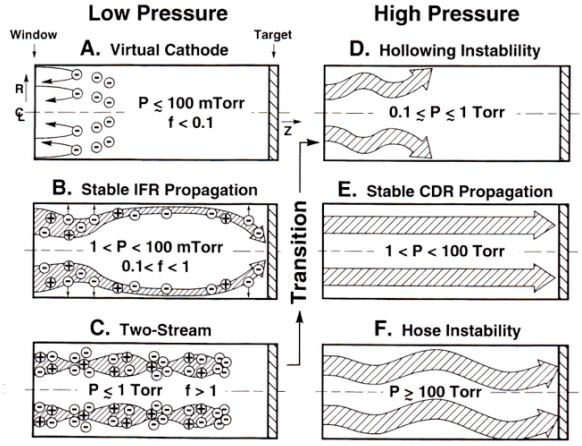

Fig. 15 Six phases of beam propagation in the long HERMES III gas cell as a function of pressure P and charge neutralization fraction f.

Preliminary axisymmetric IPROP calculations indicated that the transport efficiency of the beam through the gas cell would be maximized if the injection angle (transverse momentum) could be

minimized. Accordingly, injection using a AK gap of 70 cm (minimum angle with minimum scrape off) in the EPA diode held the best expectation for maximum beam transport, and the bulk of our measurements of transport efficiency in the 10.8m gas cell were taken there (Fig. 16).

Holding the pressure at the optimum value for transport, and varying the AK gap verified that 70 cm indeed maximized the transport [50]. A gas pressure of 100 Torr of either air or N2 maximized the energy transport. At this maximum, the energy transport efficiency is 71± 2.4 %.

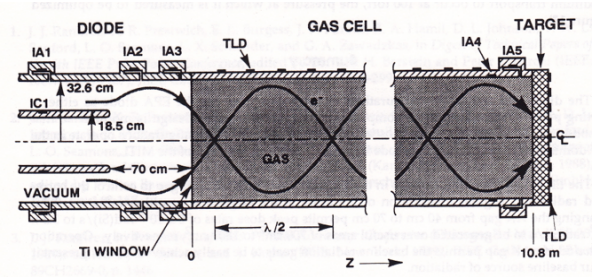

Fig. 16 Long Gas-Cell transport using Extended-Planar-Anode diode as injector. IA1 through Ia5 are current shunts.

Our measurements and modeling show that the optimum at 70 cm is a result of a balance between improving the transport efficiency by minimizing the injection angle into the cell versus minimizing the losses to the side anode wall of the diode just upstream of the entrance window. The optimum at 100 Torr is the result of a delicate balance between improving the trapping efficiency due to the magnetic pinching force generated by the residual net current after the beam passes through its first axial focus in the cell versus minimizing the subsequent energy loss due to inelastic collisions and instabilities as the beam propagates to the target.

3.6.4. Long Gas Cell using CL Diode Injector

Replacing the EPA diode with the CL diode (Fig. 17 and 18) as an injector [51] eliminates the current loss upstream of injection for small injection angles, and thus permitted the possibility for increased energy transport. At this theoretical injection optimum, we explored in detail the behavior of the annular beam as a function of gas pressure over the range 0.5-640 Torr for two injection radii, showing both experimentally and theoretically that the region of useful energy transport lies in a *propagation window* between two regions of instability caused beam plasma interactions [52]. The maximum transport within the *propagation window* (as with the 30° EPA injection) results from a tradeoff between a reduced self-magnetic pinch force as the pressure is decreased and the increase collisional and inductive losses as the pressure is increased.

In addition to our standard radiation and calorimeter diagnostics, several new diagnostics were employed. These included TLDs surrounding the perimeter of the cell and along its length, which are sensitive to localized beam loss at the Al wall of the cell by direct beam deposition and radiation, a MW

(microwave) detector sensitive to presence of strong plasma-electron oscillations induced by beam-plasma interactions, and net-current diagnostics, all of which are sensitive to the beam behavior within the cell.

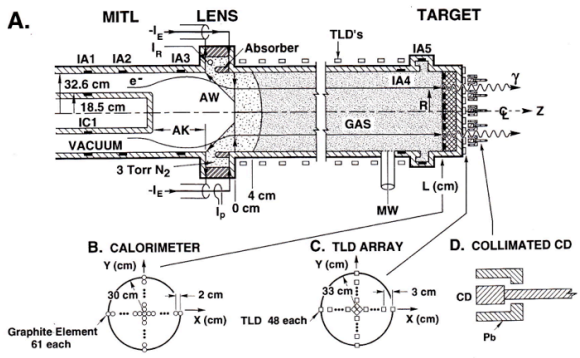

Fig. 17 (A) Long Gas-Cell transport using Compound-Lens diode as injector. (B) Detail of upstream surface of the graphite calorimeter. (C) Detail of the TLD array showing TLD placement. (D) Detail of a collimated Compton diode.

Below ~1 Torr as the collision frequency decreases relative to the plasma and cyclotron frequency, these diagnostics show that the plasma-return-current instabilities disrupt the beam. These instabilities have two-stream instability characteristics in the beam front (Fig. 15C), and resistive instability characteristics back in the beam body, where the plasma electron population has thermalized. In contrast, above ~100 Torr, as the plasma-electron population is reduced by dissociative recombination with positive ions and the electron avalanche is diminished, the resistive hose (Fig. 15F) instability enhances transverse oscillations in the beam centroid. The resistive hollowing instability (Fig. 15D) exists below 40 Torr for the HERMES III parameters, but is weak, except for pressures below 1 Torr, where the number of betatron oscillations in the 10.8 m long gas cell becomes significant. Thus in the region between

Fig. 18 Tom Chaves adjusting Compound-Lens injector to long gas cell.

~1 and ~100 Torr, where the number of betatron oscillations is less than three, the beam propagates without significant instability growth in this *resistive* CDR (collision-dominated regime) (Fig. 15E).

Within this pressure propagation window, the maximum energy-transport efficiency for our paraxially injected beam is measured to be 79±1.5%, in reasonable agreement with the 74% simulated. This measured optimum occurs between 20 and 30 Torr, and is the same for either of the injected radii used [52]. At these pressures for the 20-cm radius injection, the annular structure is preserved over the drift length, owing to the strong on-axis plasma return current. Both the measurements and

simulations show that for this injection radius of 20 cm, the beam at peak power is injected near equilibrium and, thus, propagates with little radial oscillation in the gas cell. In this case, a large fraction of the beam loss (9-20%) occurs within the first 29 cm following injection. Injection at the 12 cm radius, on the other hand, reduces this loss to only 2-4%. However, under this condition the beam is injected out of equilibrium and loss from the resulting radial oscillations that occur downstream of injection offsets the gain at injection. With the improved energy transport efficiency, the CL diode became the injector of choice for intense radiation exposures in the outdoor test cell.

In the data just below 0.5 Torr there was a hint that there may be another propagation window. Accordingly the range between 0.001 and 1 Torr was also examined, where a second *propagation* window was found between ~1 and 100 mTorr that is dominated by propagation in the *semi-collisionless* IFR (ion-focused regime) (Fig. 15B). Here the annular beam is guided by a plasma channel produced by its own ionization near the wall of the gas cell. In this regime the maximum energy transport is 33±2.3%, which occurs at ~5 mTorr for a cell of 10.8 m length. The final spatial phase of the IFR propagation, however, is different than in the collisional regime. Namely, it involves the contraction of the annular beam at the target. Approaching the conducting target, the repulsive electric fields are rapidly shorted out (as in a vacuum discussed earlier), with the magnetic attractive force unaffected. Thus the beam receives a sudden inward impulse, which is sufficiently large to to affect the radial profile of the beam as it strikes the target. At 10 mTorr the measured sweep speed is 5 cm/ns at the target in agreement with model estimates. The associated time integrated FWHM of the radial beam profile is only 3 cm. Its on axis dose at 10 mTorr is 210 J/g, in contrast to 10 J/g at the beam radius of 20 cm at the graphite target for the CDR optimum at 20 Torr.

Propagation in both regimes (the IFR at early time and the CDR at later time) is observed between both *"propagation windows"* (ie from ~10 to ~100 mTorr), which produces two distinct bremsstrahlung pulses from the single injected beam pulse. As the pressure increases, two-stream instabilities terminate IFR propagation (Fig. 15C) and the associated bremsstrahlung pulse earlier in time. Above 10 mTorr, this instability is sufficiently quenched by gas collisions that CDR propagation in the beam body can occur, leading to second bremsstrahlung pulse.

Our measurements and analyses provide a quantitative description of this complex transport of the HERMES III beam over six decades in gas pressure [54]! This research is applicable to high-power pulsed-electron beams with currents near the Alfven limit. Operation in either *propagation window* permits the

spatial distribution, rise time, and FWHM of the radiation pattern generated at the target to be adjusted within a wide range for differing exposure applications.

3.6.5. HERMES III R&D Mini-Summary

HERMES III proved to be an incredibly reliable high-power pulsed accelerator of electrons providing a repeatable peak current of ~700 kA and peak voltage of ~19 MV, to better than ±3% from shot-to-shot, with out breaking vacuum. These characteristics together with the robustness of the EPA diode and optimized Ti/Ta/C target at the accelerator exit permitted the initial radiation design goals of the Radiation Effects Program for TW ɣ-ray exposure to be met in early 1988, on schedule and under budget.

As a result Juan Ramirez, the program manager of HERMES III in Ken Prestwitch's Department, was promoted to a Senior Manager of yet a more powerful weapons-effect facility at Sandia named Jupiter, based on Saturn and PBFA II technologies. The driver would implode foil targets in a z-pinch driven by 60-MA currents to produce both soft and hard x-rays and those in between needed for weapon effects simulation. Later Juan and Wendland Beezhold pushed a promotion for me, making me a Distinguished Member of Technical Staff in 1990. The citation read:

In recognition of his outstanding contributions to Sandia's weapons effects simulation program. His research into the generation and transport of high-voltage, high-current, short-pulse, electron beams developed a fundamental understanding of the physical processes controlling the behavior and performance of intense bremsstrahlung sources. His research has been instrumental in establishing and sustaining Sandia's reputation for excellence in above ground radiation effects testing.

After we met our initial radiation goals, I had the opportunity and joy to expand on the HERMES III capability to met the other Sandia needs discussed above. These requirements facilitated the development of cleaver diode and transport configurations to control the beam, necessitating new areas of plasma physics to be explored, exploited, and fundamental research to be carried out with this world class facility [55].

Still being of a university mindset, I tried never to miss an opportunity to explain our research to others at Sandia and in papers and talks at conferences, and journal publications. For example, after Juan's success in building HERMES III, Juan was asked to give an invited talk at the 7th International Conference on High-Power Particle Beams titled *HERMES III-a 16 TW, Short Pulse, Gamma Ray Simulator* held in Karlsruhe, Germany July 1988 [56]. Juan, together with Pace VanDevender, now the Director of the ICF program, supported my presenting a related contributed talk titled *Test of Extended-Planar-Anode Diode on*

HERMES III, at the conference [57]. This was a real honor. In the years following, I was able to attend the 8th, 9th, and 10th Conferences held in Novosibirsk USSR July 2000, Washington DC May 1992, and San Diego CA June 1994, respectively. At the 8th conference, I gave a poster paper titled *Temporal Characterization of the 19-MeV, 700 kA HERMES III Electron Beam* [58]. At the 9th, I was asked to present an invited talk titled *Generation, Control, and Transport of a 19-MeV, 700-kA Pulsed Electron Beam* [59], and at the 10th I gave the contributed talk titled *Intense Electron-Beam Transport in the Ion-Focused Regime Through the Collision-Dominated Regime* [60]. The talks and associated conference proceedings nicely summarized our HERMES III research and brought it to a wide audience. In 1994, I was further honored by being admitted to the Marquis *Who's Who in Science and Engineering*.

4. Z-PINCH ICF

4.1 Transition: Beams to Z-Pinches

In 1989 the Berlin wall came down and by 1994, this had resulted in a shift in our funding from DOE and the need for continued HERMES III R&D. It was also time to transition into the ICF program, as I had now developed and demonstrated skills that could be applied there. This, however, was not to happen directly, as this program was also going through a downsizing. In the aftermath of HERMES III, I was offered a job by Juan Ramirez to demonstrate the viability of a concept, developed by David Mosher of NRL (Naval Research Laboratory), to generate warm x-rays (10 to 100 keV) in a z-pinch as might be produced on Jupiter between the soft and hard x-ray regime. The experiments were to be done on the 5-MA Saturn, now converted part time from its standard 1-MV bremsstrahlung mode, to that of imploding z-pinch wire arrays for the simulation of keV x-rays for the study of weapons effects on material surfaces and electronic components.

The job was to pull together staff from Sandia, LLNL, together with support from David at NRL to design a comprehensive experiment with analysis to verify the warm x-ray concept for possible application on Jupiter. In this effort, Juan Ramirez, Wendland Beezhold, and Keith Matzen (manager of Sandia's z-pinch effort within the Fusion Program) did a superlative job of facilitating the necessary inter-department and laboratory connections and associated funding.

4.1.1. Compact Wire Arrays for Warm X-Ray Production

Backing up a little, the generation of terawatt bursts of warm x-rays (10 to 100 keV) are of interest for the study of in-depth material effects induced by nuclear radiation. Pulsed-power bremsstrahlung generators with MeV electron-endpoint energies that use thin, reflexing converters have the potential of generating such bursts [61]. However, the warm x-ray field is simultaneously accompanied by hard x-rays, which mask the effects produced by the lower-energy photons. Accordingly, bremsstrahlung generators are generally used to study hard-radiation effects as in the case of the 1-MeV electrons on Saturn and 20-MeV electrons on HERMES III.

At the other end of the photon spectrum, the PRS (plasma radiation source), which is a z-pinch formed from the radial implosion of an annular plasma, provides an excellent source of intense keV x-rays. Here, the azimuthal magnetic field associated with the axial flow of a large current through a cylindrically symmetric plasma creates a magnetic pressure (**J** x **B** or Lorentz force) that accelerates the plasma radially inward. The plasma x-rays are generated by thermal processes when the imploding

plasma stagnates on the axis of symmetry (the z-axis), and its radial KE is converted into internal energy and radiation. On existing PRS drivers, of which Saturn was the highest-current example at the time, the efficiency of thermal radiation production drops rapidly for photon energies exceeding ~5 keV due to the low mass required for high temperature and the growth of instabilities. The need for a practical, intense radiation source in the 10- to 100-keV between existing PRS and bremsstrahlung sources was thus the motivation for David's concept for Jupiter.

Single-wire z-pinch experiments on the 0.8-MA Gamble II showed a significant yield of warm x-rays [62]. The experiments suggested that the radiation was produced by a non-thermal mechanism. The x-ray spectra measured were consistent with a bremsstrahlung production mechanism, which scales as the square of the wire's Z (atomic number). In such a mechanism (just like electrons generated from HERMES III incident on a high Z target, but now at much reduced voltage), electrons are envisaged to be accelerated to ~100 keV by the inductive fields generated either along the wire load or within the load across collapsing pinch spots associated with the onset of the sausage instability before impact with the high Z wire plasma itself.

Gamble-II data suggested that the condition for maximizing these *run-away* electrons, and the associated radiation corresponding to this mechanism is given by the Mosher criterion: $I/(m/l) \sim 2$ MA/(mg/cm), where I is the current flowing through the wire load having a mass per unit length of m/l. At this optimum, 60 J of x-rays above 15 keV are generated in a 50-μm diameter tungsten wire of 4-cm length on Gamble II, operating at 0.8 MV. The corresponding overall efficiency is ~0.25%. Assuming that this radiation scales like I^2 (as is measured for thermal radiation), then 340 kJ of x-rays greater than 15 keV was expected for the 60-MA Jupiter accelerator. This yield was sufficient to satisfy the Jupiter testing needs in this warm x-ray energy band.

Saturn, however, is a low-inductance electron accelerator as will be Jupiter. As such, it is prone to flashover of its Lucite insulator stack at the vacuum-water interface (Fig. 19A) due to the high inductive voltage drop generated when the accelerator quickly drives a high-inductance load, as would be the case for a single-wire load mounted on axis. Thus, the rapid implosion of *compact-wire-arrays*, instead of a single exploding wire on axis was proposed by David for the Saturn experiments. In this arrangement the initial inductance of the wire array is kept low, preventing insulator flashover early in the current pulse. The radius of the wire array is chosen such that the implosion occurs early with respect to the time of peak current, enabling the wires to form a single axial slug and permitting the sausage instability to be well

established during the peak portion of the pulse.

4.1.2. The Experiment

To test David's concept for Jupiter, we designed a set of experiments (Fig. 19) to study tungsten *compact-wire-arrays* for the first time on Saturn [63]. The characteristics of the implosion were initially calculated using the fast circuit code ZORK [64], modified my me to include the radially collapsing load. Jim Hammer of LLNL using a Lagrangian RMHC (radiation magnetohydrodynamic code) [65] in ID (here denoted by L-RMHD), confirmed the ZORK results. Importantly it gave insight into the current and charge densities, the magnetic electric fields, and the particle temperatures generated during the implosion phase for the tungsten loads. It enabled the resistance of the load, which is ignored in ZORK, and its thermal radiation to be estimated and provides a starting point for calculations of the non-thermal mechanisms.

Ultimately, three criteria were used for the experiment: configure the load to resemble the single-wire plasmas on Gamble II that produce maximum non-thermal yield, maintain a low-inductance load geometry to couple efficiently to the Saturn pulse line, and satisfy predicted non-thermal scaling laws (such as Mosher's criterion) to maximize non-thermal production at high current.

At the Saturn insulator stack, current is simultaneously fed into four parallel MITL's (Fig. 19A). The current from each MITL is added in a 8-post-hole convolute (Fig. 19B) and injected into a radial feed that delivers the summed current to the imploding load (Fig. 19C).

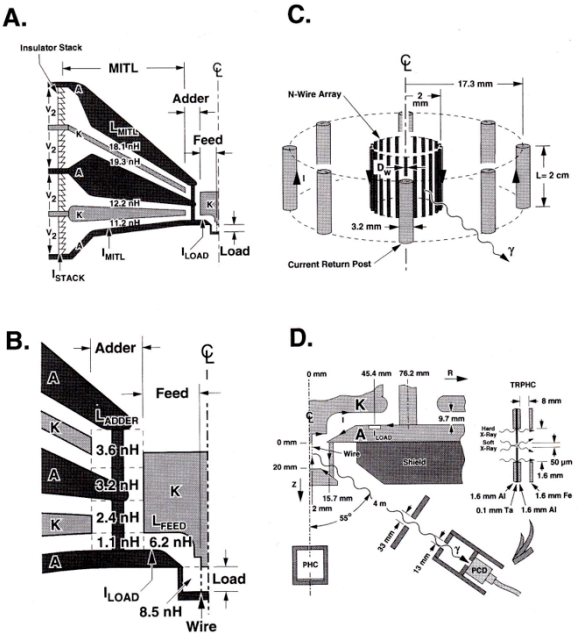

Fig. 19 (A) Saturn configuration showing location of current diagnostics I_{stack}, I_{mitl}, I_{load} with respect to the insulator stack, MITLs, Adder, Feed, and Load sections. (B) Detail of Adder and Feed sections. (C) Detail of Load section showing position of Compact cathode wire array with respect to the eight anode current return posts. (D) Experimental arrangement showing location of radiation diagnostics.

In the experiments, the radius of the wire array cathode was kept fixed at only 2 mm, and 8 anode current return posts, which surround the array, were kept fixed at the larger radius of 15.7 mm, all of length 2 cm. Scaling arguments suggested a total wire mass in the neighborhood of ~4 mg. Accordingly, the mass of the tungsten wire loads used was varied in factor-of-two steps from 1

to 16 mg. Because of the strong Z dependence of the non-thermal radiation, this dependence was checked by imploding 4-mg copper and aluminum wire arrays in addition to tungsten.

B-dot monitors measured the current in the lower MITL adjacent the insulator stack, and the total current in the radial feed adjacent the load. Outside the load region, diagnostics are positioned in three vacuum line-of-sights at 35° to the horizontal. During the rise of the current pulse (~50 ns), voltages across the MITL gaps reach MV levels and in particular, near the time of axial stagnation where the inductive loading is high, high voltages are developed in the region of the load. These high voltages combined with electron current loss lead to the generation of hard bremsstrahlung radiation. As was done for HERMES III, electron loss was modeled by Jim Poukey, and the subsequent hard bremsstrahlung by John Halbleib. This radiation represents a significant background to load radiation detectors. The time dependence of this radiation measured by an open-ended cable compares well with our calculations when using the dose-voltage scaling [153] we established earlier for HERMES III, and was easily removed from the detector signals. Bolometers, PCD (photo-conducting detectors), and a FFA (filtered fluorescer array) measured the radiation history in broad photon-energy bins ranging from 0 to ~350 keV (Fig. 19D). A time-integrated crystal spectrometer supported the measured spectra in the PCDs over the range 0.8 to 2.6 keV. A 1-ns gated FFPHC (fast-framing pin-hole camera) imaged the imploded wire array in 5 sequential frames, whose inter-space timing could be adjusted.

The FFA was a key instrument specially designed at LLNL by Paul Springer and Bob Thoe for this experiment to measure, in sixteen pairs of channels, non-overlapping coverage from 10 to 100 keV with a sensitivity optimized to measure an emission of about one kilojoule per energy band and a limit of detectability of about a Joule per channel. In the experiment, however, the non-thermal yield was an order of magnitude lower than anticipated. Moreover, the background of the hard bremsstrahlung was unanticipated, as this was the first time the instrument was being used in this harsh radiation environment.

Therefore it was necessary to field modify the instrument to increase its sensitivity and reduce its sensitivity to the background. The increase was accomplished by changing both the geometry and energy bands. The final configuration consisted of two pairs of filter fluorescers covering 10 to 20 keV and 20 to 30 keV. *Fortunately, learning from the past when bring up a new instrument, I had constructed eight additional PCDs, some using Ross filter pairs to also cover the range 0.7 to 300 keV in crude steps as a backup. Together this 10 channel assortment was able to*

clearly measure the thermal and non-thermal portion of the x-ray spectra, and saved the experiment. Bolometer and PCD diagnostics for measuring the characteristics of PRS had become a refined art form developed by Rick Spielman at Sandia. Rick was instrumental in the successful implementation of these crucial diagnostics.

4.1.3. The Results

The *compact* tungsten wire arrays, which were now being measured for the first time on Saturn [66,154], exhibit multiple implosions, in agreement with Jim Hammer's L-RMHC and our in house MHD PIC Code simulations, developed by Barry Marder at Sandia and referred to as TIP (Total Immersion Particle) [67]. Aside from the observed axial bright spots at the time of the implosion, soft radiation from these low-velocity implosions is well described in ID by Jim's L-RMHD simulations. 2D L-RMHC simulations by Steve Maxon of LLNL show that the bright spots that are formed during the first implosion are due to the growth of the RT (Rayleigh Taylor) instability, which leads to a bubble and spike phase [68]. This is the first explicit calculation of a hot spot in two-dimensions employing the full MHD equations. The bubble regions evolve into the bright spots, which corresponds to a region where the density and temperature are enhanced over the surrounding plasma regions. Although the 2D simulations were not run for more than 5 ns past the time of the first implosion, the simulations indicate that as the plasma expands, the RT instability shuts off, and the sausage instability begins to grow, which may lead to the subsequent, more intense bright spots seen later in time. Experimentally, a fraction of the evolved bright spots are observed to be the source of the warm x-rays as observed in the Gamble II single-wire experiments.

Warm x-rays from non-thermal processes are observed between 10 and 100 keV corresponding to a yield and efficiency of only 35±17 J and (0.02 to 0.08)%, respectively [66]. The similarity of the measured warm x-ray spectra and spatial structures to those measured at lower current on Gamble II suggests a common production mechanism for those processes. The lower production efficiency and the larger, more irregular pinch spots formed in our experiment relative to those measured on Gamble II, however, *suggest unfortunately that implosion geometries are clearly not as efficient as single exploding wire geometries for warm x-ray production.* These differences may arise from instabilities, azimuthal asymmetries, and inferred radial bouncing that accompanies the annular implosion geometry.

To better understand why we observed such a limited yield of warm x-rays Barry Marder (using his TIP code), Dave Mosher, Dale Welch (using his IPROP code), and I developed a model of

electron acceleration across magnetic fields in this highly-collisional, high-atomic-number plasma [66]. The model shows the existence of a critical electric field below which strong non-thermal production does not occur. The ID MDH simulations show that a significant non-thermal electron population is not expected in this experiment, because the calculated environmental electric fields are at least one to two orders-of-magnitude below the critical field. These negative non-thermal results are confirmed by the L-RMHD simulations using a non-thermal model based on a Fokker-Plank analysis at LLNL. Prof. John DeGroot of UC Davis greatly helped in this effort, and was instrumental in facilitating our collaboration with our LLNL colleagues. John had been Rick Spielman's thesis advisor. The results of the experiment, including the model were published in a Sandia report titled *X-Ray Emission from a High-Atomic-Number Z-Pinch Plasma Created from Compact Wire Arrays"* [66].

4.2 Z-Pinch Implosions For Thermal X-Ray Production

This experiment and subsequent analyses opened the door to the world of z-pinch physics. David had taken me under his wing, generously mentoring me in this new arena of physics. His typical back of the envelope approach to estimating characteristics of an implosion fit well with my philosophy of using such approaches to checking the sensibility of complex computer calculations. I encouraged him to develop and present a course in z-pinch physics for the US Particle Accelerator School, for which I was Sandia's representative at the time. This he did magnificently, using his intuitive mathematical formulations, in the summer of 1996 at the Monterey summer school.

Simultaneously to our Compact-Array research, Sandia was being reorganized with the Nuclear Simulation Department (which had been under Jim Powell) and the Fusion Directorship (which was under Pace VanDevender), both of which had been under one directorate headed by Pace, were now expanding into two directorships with Jim becoming the new director of the Nuclear Simulation part of the former organization.

Pace wanted me on the fusion side of the house, which is where I wanted to be years ago. Because of my new found experience with wire arrays, I found myself in Keith's Department within Pace's Directorate, with my funding for the rest of the FY still coming from Wendland who was now outside the overall umbrella of fusion. Keith suggested that I explore mechanisms for improving the output of thermal wire-array PRS implosions. This again set me on a new course, not quite yet fusion, but at least now I was in the fusion directorship.

4.2.1. Motivation for Breakthrough Experiment

Previous experiments using wire-array z-pinch loads as PRSs did not show significant improvement in performance when the wire number increased beyond 10-20 wires [69, 70]. Twenty-four wires were generally considered adequate to provide sufficient azimuthal symmetry for z-pinch loads. Such loads [71] were routinely used for radiation effects studies at Sandia. These loads developed unstable axial pinches that exhibited poor reproducibility, and research was accordingly directed to developing implosions of the more azimuthally symmetric annular and solid gas-puffs loads [72, 73].

In January 1995 when bringing into operation a large-FFPHC [74] to examine the implosion phase of a typical 24-aluminum wire array on Saturn, however, I clearly observed self-pinching of the individual wires prior to the implosion of the array. This lack of a measured coherent plasma shell, as was thought to be the case, prior to the radial implosion of the array, motivated the use of increased wire numbers. The data suggested that perhaps these unstable pinches could be better stabilized if more wires were added, in order to eliminate the self-pinching, by the formation of a continuous plasma shell prior to array implosion. Moreover, one-dimensional modeling of such implosions of thin plasma shells predicts much higher kilovolt x-ray powers and shorter pulses than had been seen experimentally [75-77].

Accordingly, I proposed examining the implosion as a function of wire number, keeping the array mass fixed, covering both high wire numbers, as well as, exploring the previously used numbers below 25 wires. Importantly, this extensive range permitted the effect of inter-wire gap g to be examined. Owing to Saturn scheduling, the experiment was delayed until June of 1995.

4.2.2. Experimental Setup

The general experimental arrangement [78,79] was similar to that previously used in our *compact-wire array* research (Fig. 19), except for the number of wires in the array, the array holder, the load geometry, and the diagnostics (Fig. 20). The geometry chosen was in the mass-radius range previously used for earlier PRS studies by Rick Spielman. The associated implosion dynamics modeled by ZORK calculations confirmed its suitability. Although tungsten, because of its greater number of energy transitions relative to those of aluminum, generates significantly more emission than aluminum, the spectral characteristics of aluminum wires had been well studied, and would be invaluable in diagnosing the physics of the implosion. Moreover, we could obtain aluminum wire in the sizes needed. As such, aluminum wire was chosen for the June experiments.

The loads consisted of annular cylindrical arrays of 20-mm long

aluminum wires mounted at a radius of either 8.6 or 12 mm (Fig. 20). These loads provided the electrical connection between the cathode and anode of the radial feeds of the Saturn accelerator as in the *compact*-array case. For the

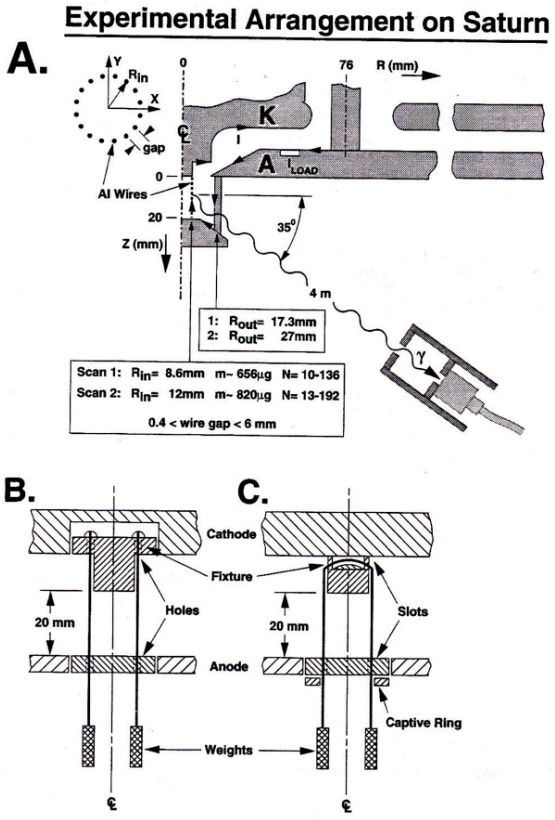

Fig. 20 (A) Experimental arrangement in the r-z plane showing the position of the wire array, the current return path in the anode housing, the load current monitors, and the post-hole convolute. (B) Load fixture for wires with inter-wire gaps of 0.6 mm and greater. (C) load fixture for arrays with inter-wire gap of 0.4 mm.

small-radius array, the mass was approximately fixed at 0.63 mg and the number of wires increased from 10 to 136 in eight discrete steps by simultaneously decreasing the diameter of the individual wire from 38 to 10 μm. For the large-radius array, the mass was approximately fixed at 0.83 mg and the number of wires was increased from 13 to 192 in discrete steps by again simultaneously decreasing the diameter of the individual wires over the same wire-diameter range. The shot geometry was randomized between shots so as not to let machine performance influence the scans.

These loads permitted inter-wire gaps of 6 to as low as 0.4 mm to be explored for both geometries. At low numbers they were held in place by threading them through small holes in the cathode-anode fixture and made taught by attaching small weights to each wire, as was done previously (Fig. 20B). At high number the distances between the wires were to small. Instead they were carefully draped over machined grooves in the fixture and again held taught by weights attached to the bottom of each wire pair (Fig. 20C). This assembly permitted the wires to remain taught during vacuum pump down, which changed the distance between the cathode and anode slightly prior to shooting the accelerator. The ultimate limit on wire number and associated inter-wire gap was dictated by the fragility of the wire and the ability to machine the wire holder with the precision needed.

The diameter of the smallest wire used was less than 1/10 the size of a human hair. I shuddered every time the wire array, which was constructed in a building 100 m away from Saturn, was transported by Terry Gilliland by hand to

Saturn. There it was installed by Terry, the wire-array assembler Roberta Hanes, and my technician Ray Mock at the center of Saturn (Fig. 21). One slight knock and all the wires would beak. This happened more than once. At this point, let me mention a few words about Ray Mock. He has been my invaluable technician, since joining my team during

July 6, 1995 SNL Albuquerque, NM
World's first high wire-number experiment.

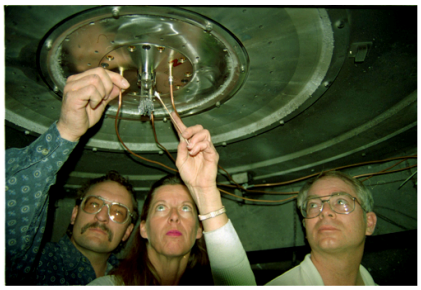

Terry Gilliland Roberta Hanes Ray Mock

Fig. 21 Terry Gilliland, Roberta Hanes and Ray Mock loading world's first high wire-number load at bottom of Saturn accelerator.

the HELA experiments, and has been with me ever since. His dedication to our work and attention to detail has greatly contributed to its success.

Either a collection of eight cylindrical-steel rods (Fig. 19C) or a cylindrical stainless-steel can, with eight slots of width 10 mm symmetrically positioned in azimuth, provided the current return path. The rods were used for the 0.6 mm and greater inter-wire gap loads, while the can was used for the 0.4 mm gap loads. The rods and can were located at a radius of 17.3 mm for the 8.6 mm array radius shots and at 27 mm for the 12 mm radius shots. The large distance between the array and current return minimized the perturbation the gaps in the current return would have on the compressing magnetic field at the wire array.

The azimuthal gaps permitted 70% of the radiation from the load to be measured in an extensive array of detectors located 4 m downstream of the load at the ends of three vacuum lines of sight positioned 35° with respect to the normal to the pinch axis (Fig. 20A). These detectors included a spatially integrating time-resolved nickel bolometer, filtered XRDs (x-ray diodes), and filtered PCDs that covered x-ray energies from ~10 to 7000 eV. Two FFPHCs were also used. One camera is referred to as the small-FFPHC. It was filtered by 25-μm Be and was sensitive to photons greater than 1 keV, with 1 ns temporal, and 150 μm spatial resolution. The other camera, the images of which helped motivate the experiment, is referred to as the large-FFPHC. It was filtered by 5.6 μm of Kimfol, and was sensitive to both 200-300 eV photons and to those above 1 keV. It had a 0.1 ns temporal and a 75 μm spatial resolution. In addition, a time integrating KAP (potassium-acid-phthalate) crystal spectrometer measured the K-series x-ray spectrum.

All XRDs and PCDs were duplicated with an independent set of detectors to provide redundancy and a corresponding check on signal levels.

Before and after the measurements, the relative sensitivity of each PCD diamond element was established to a precision of 13% by exposing each element to the same filtered x-ray fluence from aluminum wire shots. The absolute response of a given element is tied back (via this relative technique) to detectors calibrated at the Brookhaven National Synchrotron Light Source to a precision of 20%.

4.2.3. Observations

The improvement in pinch quality with N (wire number) in both geometries is evident in the x-ray FFPHC images and manifests itself as increased inductive current notches at peak compression, increased radial compression in the x-ray images, reduced radiation rise-time and pulse-width, and increased x-ray power [78, 79]. Measured, for example, for the emitted K-shell x-rays (greater than ~1 keV) is an impressive reduction in rise time (from 48 to 2.3 ns) and pulse width (from 60 to 3.2 ns), and the associated increase in power (from 0.7 to 5 TW), when N is increased from 10 to 90 in the small-radius loads. For both loads, the radial compression improves from less than 10:1 for inter-wire gaps of 6 mm to more than 20:1 for gaps of 0.4 mm. Over this range, the total radiated energy increases from ~175 to ~350 kJ for the small-radius load and from ~240 kJ to ~440 kJ for the large-radius load. The peak values exceed the calculated KE for a 20:1 compression by about 25%.

Most importantly, when the various radiation characteristics are plotted versus gap, the data for the two geometries fit a single curve dependent on gap alone! Below a gap of ~1.4 mm, the increase in power with decreasing gap becomes rapid in all x-ray channels, suggesting a transition between two different kinds of implosions. The gap where the change in slope occurs coincides approximately where the observed kink instability vanishes with decrease gap. Such instabilities have been inferred for low wire number, higher-Z implosions, like those for copper wires where an apparent helical shape of the implosion is discerned. At the smallest gap explored of 0.4 mm, both loads generated an incredible level of ~40 TW of x-ray power. *This discovery of a factor of ~20 increase in power from the largest to smallest gap explored, would have a profound effect on the ICF, program, as it suggested that fusion might be realized using wire arrays.*

Experimentally, the radial convergence is defined as the ratio of the initial diameter of a wire array to its FWHM on axis, obtained from a radial lineout of time-integrated images of the kilovolt emission. When the radial convergence is plotted as a function of gap, the data suggests that the convergence is approximately independent of the initial radius. The increase in measured total x-ray energy [normalized to the KE calculated by ZORK using a fixed 10-to-1 radial

convergence] with decreasing gap is also consistent with this normalized KE being a function of gap alone.

The KE difference between the two loads arises from improved energy coupling between the accelerator and the larger-radius load, which stagnates ~10 ns later than the small-radius load. The larger-radius load generates ~23% more KE for identical convergence ratios, in agreement with the increase in total radiated energy measured. The longer implosion time is closer to the time that peak current can be delivered to a short-circuit load. The measured radiated energy is also consistent with the log of the measured radial convergence, as expected if the radiated energy scales with the KE.

4.2.4. Explanation in R-θ Plane

Early in the experiment, I realized that we had no model to explain our measurements and to provide a guide as to the underling physics mechanisms. So just like in the process in designing the HERMES III diode, where I brought the talents of Jim Poukey and John Halbleib together to predict the electron flow at the diode-target and subsequent radiation output from the target, I interested George Allshouse and Barry Marder in modeling our z-pinch measurements. In HERMES III, the output of Jim's MAGIC code was used as input to John's ITS code. Here, George modeled, using the L-RMHC code in 1D, the radial dynamics of an isolated single-wire from the solid state, using the measured current, including its 100-ns-long current pre-pulse. The early-time radial distributions from these calculations were then used as initial conditions for an x-y RMHC simulation of the array configuration in the r-θ plane by Barry using his TIP code.

In the L-RMHD code, for a current-per-wire equivalent to that of $N < 20$, the expansion of an individual wire plasma is reversed by the self-magnetic field before the array implodes to the z-axis. For the lower current per wire when $N > 80$, the expansion would continue for longer than the implosion time time. The x-y TIP simulations showed that the 1D behavior of individual wire plasmas is not substantially altered in the array configuration. For our experiment at $N = 40$ ($g = 1.4$ mm), the expanding individual wire plasmas are calculated to merge with adjacent wire plasmas to form a continuous plasma annulus prior to implosion. For smaller N, individual wire plasmas do not merge during expansion because of the increased gap, and the self-pinching due to the high wire-plasma current. For larger N, a more symmetric annulus is formed by the densely packed, expanding wire plasmas.

The more effective plasma merger with larger N (decreasing g) helps explain the improvement in implosion quality for g less than 1.4 mm. The calculated transition is consistent with the first large-FFPHC images that helped motivate the experiment in the first place. Then the load used was made with 25 wires (1.3

mm gap) in what we now call the transition region. In the images, individual wire plasmas were observed to neck-off in the form of bright spots 20 ns prior to radiated power, when the array had only imploded a fraction of a mm radially. Ten nanoseconds later, after the array had imploded an additional 1.5 mm, the observed plasma emission becomes a continuous distribution, with no evidence of individual wire structure, suggestive of plasma merger.

The above analyses, however, are insufficient to elucidate the mechanisms responsible for the reduced implosion quality observed in the FFPHC images at small N, as even the discrete-wire implosions of N = 10 display impressive radial compression in TIP. Dave Mosher pointed out that when N is small, large-amplitude sausage instabilities can grow as the individual wire plasmas self-pinch, forming axial asymmetries that are uncorrelated with their neighbors [81, 82]. Once unstable wire plasmas merge, the resulting 3D asymmetries represent a large perturbation for RT growth and contribute to low implosion quality, poor shot-to-shot reproducibility, and low radiated power.

Both single-wire experiments and modeling of nonlinear sausage growth show that some axial regions of pinched, un-merged wire plasmas will retain radial extents comparable to that at maximum expansion throughout the implosion, leading to stagnated-plasma radii much larger than simulated by TIP. Thus, both azimuthal asymmetry and wire-plasma instability sausage growth are required to explain the poor observed implosion quality in the large-gap regime. As N increases beyond 40, pinching and the associated large-scale sausage instabilities become less important.

This physical picture supports the observed scaling of implosion quality with N and is consistent with the FFPHC measurements: For gaps as small as 1.4 mm, wires were seen to implode as separate entities until just before plasma assembly. Accordingly, I named this region the *wire-plasma* regime [78]. High-power, small-gap shots less than ~1.4 mm showed, on the other hand, formation of well defined plasma shells prior to implosion. This high wire-number region I named the *plasma-shell* regime.

4.2.5. Explanation in R-Z Plane for *Plasma-Shell* Implosions

In the plasma-shell regime, 1 and 2D RMHD simulations of an imploding plasma shell could now be compared to the measurements for the first time. This possibility continued the interest of Jim Hammer in these experiments, and now also Darrell Peterson of LANL, whom I had meet at an earlier z-pinch meeting. Additionally, Ken Whitney and John Apruzese of NRL, whom I also had meet then, were also keen to apply their sophisticated spectral analysis, including a detailed atomic model in their 1D RMHC calculations, to interpreting our measured time resolved K-shell spectra

[84-87]. In Jim's 2D simulations at LLNL, the multi-photon-group Lagrangian code L-RMHD [65] was employed. Darrell at LANL used a three-temperature model in his 2D Eulerian code E-RMHC [83]. As in the previous 1D L-RMHD and 2D TIP simulations, all simulations used the ZORK circuit model of the Saturn accelerator coupled to the dynamic PRS load that enabled peak currents to be calculated to the 5% accuracy of the experiment. The current and total x-ray power measured in the high-N loads were reproduced within experimental uncertainties.

In the 2D simulations, the calculations assumed small initial random density perturbations in an initial annular plasma that was ~1 mm thick. Progressive larger initial perturbations are needed to reproduce the data as N decreases. For both 2D simulations, radial compression is limited by RT instabilities growing out of the initial perturbation. The main x-ray pulse begins when the RT bubble (inner radius of the unstable region) reaches the axis, peaks, and ends when the spike (outer radius of the unstable region) finishes stagnating on axis. E-RMHD modeled the entire load length, producing a small second radiation peak at about the same time as the data. In E-RMHC, 1-mm-wavelength RT modes grew during implosion, merged into 3-mm-wavelength modes, and seeded a 3-mm wavelength sausage instability following peak compression, all of which are observed in x-ray images. In L-RMHC, the limited axial simulation length of 1 mm reproduced the short RT modes, but prevented growth of the longer-wavelength ones.

Analysis of the FFPHC images, PCD data, and K-shell spectra shows that near peak compression, the pinch is composed of a hot core (Te ~ 1.3 keV) surrounded by a cooler (~0.4 keV) plasma. These results are in qualitative agreement with the r-z RMHC codes, although the codes predict emission localized to smaller radii than observed experimentally. The discrepancy may be due to the 3D nature of the implosion and the code assumption of local thermodynamic equilibrium.

With this single experiment we had not only achieved a significant increase in x-ray power from a wire-array z-pinch by reducing the implosion instabilities, and, because of the comprehensive diagnostics and multiple theoretical approaches, we knew why. What a thrill! Some of the research was summarized in an invited talk I gave at the *11th International Conference on High Power Particle Beams at Prague* in June 1996 [88], and later in a letter I wrote, with useful inputs from David Mosher, and submitted to PRL (Phys. Rev. Lett.) in August 1996 [78]. Its publication in December 1996 reignited the field, which had been languishing for years.

4.2.6. *Plasma-Shell* Regime Analyses

Detailed L-RMHD analyses of our three 90-wire shots, corresponding to an

inter-wire gap of 0.6 mm provided an in depth view of the energy flow within the high power implosions [89]. The current driving the implosions has a 10-90% rise time of 35 ns with an associated peak current of 6.9±0.2 MA. Peak power occurs 80 ns into the implosion, ~10 ns after peak current. The only free parameter in the 2D simulation is the size of the initially applied random-density perturbation in the 1-mm thick shell assumed. For a 5% perturbation of the initial plasma density, both the temporal shape of the measured load current and total radiated power, with a measured peak and pulse width of 30 TW and 4 ns, respectively, are all well reproduced.

In the simulation, significant radial acceleration of the load occurs after 70 ns, resulting in 320 kJ of energy being deliver to the imploding plasma (~270 kJ in KE and ~50 kJ in internal energy for an assumed 20:1 radial convergence) before the plasma begins to stagnate on axis, at which time it transfers its KE into internal energy. A 20-to-1 final radial convergence is measured for these high-symmetry implosions, which leads to rapid heating and ionization of the radially inward-moving plasma. At ~80 ns (the peak in both the measured and simulated radiated power), the simulation shows that the hot plasma begins to cool as radiation, which is now being efficiently generated by the electrons, as they are heated by the stagnating ions, escapes the plasma. As mentioned, the main radiation pulse begins when the RT bubbles first reach the axis and ends when the spikes finish stagnating on axis.

The main radial compression occurs near 81.5 ns, as in the simulation, but the data also show that a secondary weaker compression occurs about 15 ns later, at ~96 ns. Depending on the radiation rate, secondary compressions may be expected. Apparently, highly symmetric load implosions (like ours) are required for this 1D-like, multiple-implosion character to manifest itself in PRS loads. In such implosions, the inertia from the inward motion, the subsequent conversion of KE to thermal energy, and the subsequent generation of the back EMF in the circuit causes the plasma pressure to exceed the magnetic pressure at peak compression.

After the plasma stagnates on axis, the plasma therefore expands against, and does work on the magnetic field. As the plasma expands, radiates, and cools, the current increases slightly. In this situation, the magnetic pressure can again exceed the internal pressure so that the plasma is re-compressed. The process continues until either the driving current pulse decays and the pinch disperses, or the excess internal energy is radiated away and an equilibrium pinch is established. Experimentally, 30±2% of the total emission is radiated in the second implosion (92-110 ns), in contrast with 16% radiated over the same time span in the simulation. These discrepancies are probably related to the breakdown of the LTE (local

thermodynamic equilibrium) approximation. The measurements and simulations agree on the remaining12±3% radiated between 110 and 140 ns. The simulated radial convergence is also more than that measured. Likely then, the additional radiation cooling in the simulation contributes to a greater convergence in the simulation. The cooler plasma in the simulation reduces the radial expansion of the plasma following stagnation, and the plasma rapidly reaches a quasi equilibrium without going through a second compression.

The images show at peak compression the formation of a coherent pinch on axis that has an axial variation of only 11% when integrated over the radius. This line-out is well fit by the sum of an intense, high-density (~$3x10^{20}$ ions/cm^3 [90]), Gaussian core having a FWHM of 0.62 mm that is surrounded by a lower-intensity Gaussian halo with a FWHM of ~3.2 mm. Spectral analyses indicate that a significant fraction of the hot core radiation at this time arises from FB (free-bound) transitions. The halo, on the other hand, is cooler and is dominated by hydrogen- and helium-like K-shell transitions (84, 85).

The measurement of the FB x-rays from the highly stripped, K-shell aluminum ions provides a model-independent measurement of the core electron temperature owing to the long x-ray mean-free-path and to the observed FB x-ray origin in the core [91]. The time-dependent slope of this emission, which is determined from the spatially integrating filtered PCDs over the range 2.5 to 6.2 keV, is used to extract an associated spatially averaged, time-dependent, electron temperature. This temperature oscillates in time. It has two peaks that are in synchronization with the two radiation bursts and the two radial compressions. The peak value of 1.45± 0.2 keV measured at the first compression [91] is in agreement with the simulated mass-averaged electron temperature.

Analysis of the hydrogen-to-helium-like line ratios measured in the time-resolved spectrometers by Ken Whitney indicate, however, that the temperature of the surrounding halo near the first compression is only ~0.4±0.1 keV [84]. The temperatures inferred from the time-resolved spectra then rise to the value measured in the core at the time of the first compression. This behavior of the electron temperature obtained from the line ratios is indicative of a breakdown in ionization equilibrium.

Analysis of the widths of the hydrogen- and helium-like α, β, γ, and δ spectral lines from the time-resolved crystal spectrometer show that each of these widths broadens and contracts as the plasma contracts and expands at the two compressions. Prof. Itsic Maron of the Weizmann Institute pointed out that the corrected widths could be associated with pure Doppler broadening due to ion motion. Indeed the corresponding ion

velocities extracted are consistent with those measured from the FFPHC, and that simulated at the first compression. The line broadening is probably associated, however, with motion that can arise not only from coherent radial motion of the plasma, but also from micro instabilities and fluid turbulence within the plasma, and from intrinsic ion temperature. The widths are consistent with some complex mix of all three of the Doppler shifting and broadening mechanisms, and they clearly are related to the overall motion of the plasma producing the two compressions.

As mentioned, the pre-peak power images show the formation of a well-defined annular shell that exhibits the classic RT bubble and spike structure with measured wave lengths of ~3.2 mm, in agreement with the E-RMHD simulations. The plasma expands radially after peak power. During the expansion, the development of axial non-uniformities suggestive of the sausage instability are observed in all following time frames including those through the second implosion. The periodic variation in the axial line-outs suggest a wavelength of 2.6±0.3 mm for the instability. These observations are consistent with a calculated growth time for the sausage instability of ~2 ns and an estimated wavelength of ~2 mm for the fastest growing mode. The FFPHC data, as well as the simulations, thus suggest that the large-wavelength RT instability measured prior to stagnation seeds the sausage instability after stagnation.

This comprehensive research was summarized a paper I titled *Dynamics of a high-power aluminum-wire array Z-pinch implosion*, which was submitted to POP (Physics of Plasmas) in December 1996 [89]. I was both pleased and surprised to see that this paper was called out in a poster advertisement for the journal at the following DPP (Dense Plasma Physics) APS (American Physical Society) meeting held in Quebec City, Candia the following year.

4.2.7. Variation with Radius and Mass

Prior to these aluminum experiments, wire-array loads had been optimized for x-ray energy and power output only in the small-wire-number wire-plasma regime. The substantial improvement in implosion quality and associated radiated power that occurs in the *plasma-shell* regime suggested that a reexamination of the mass and radius conditions that maximize radiation output in this regime would be instructive. As was done with the three high-power shots just discussed, measurements of the more azimuthally symmetric *plasma-shell* implosions could then be more realistically compared with r-z RMHC simulations to gain additional insight into fundamental physical processes, free of the large azimuthal inhomogeneities that have limited previous detailed comparisons. Accordingly, after the initial wire-number experiment concluded in

July 1995, two additional experimental series were conducted in January 1996, both to reexamine the conditions that optimize the sub-kilovolt and K-shell output, and to explore the longer implosion-time regime. The K-shell radiation is of importance in assessing the effects of nuclear x-rays on component surfaces, and the longer implosion-time loads (larger radii) are anticipated for higher-power accelerators.

In one series, the radius was held fixed at 12 mm (which was the large-radius used earlier) and the mass was varied between 0.42 and 3.4 mg in six steps by changing the diameter of the individual wires and their number [92]. For most of the masses, the number of wires was held at 192, which fixed the inter-wire spacing at 0.4 mm. In the other series, the mass was fixed at 0.6 mg, which optimized the x-ray output in the mass series, and the radius was varied between the small-radius used previously of 8.75 mm to 20 mm, in ~4 mm steps [93]. The experimental arrangement was similar to that employed earlier except for the specific wire-load configurations.

As before, the measured current flowing in all the loads was well approximated by the 0D slug-model ZORK implosion driven by a Saturn circuit model. The implosion calculations were terminated when the slug radius reaches 1/20 of the initial array radius, which was typical of that measured earlier for the high-power shots. Darrell Peterson again modeled the implosions in r-z using the Saturn circuit model as input to his E-RMHC code. For all configurations, the ZORK and E-RMHD currents adequately agree with that measured up to near peak compression and after, respectively. *Most impressively, the E-RMHD comparisons with both the measured magnitude and shape of the total power pulse at the first compression agree within experimental uncertainties with* ***all*** *shots taken in both the mass and radius scans, using just a single random perturbation of 15% in the density of the initial plasma shell!* The overall agreement in these comparisons, which span more than a factor of two change in array radius and almost an order of magnitude change in array mass, thus provides credibility to the hydrodynamics of the simulations.

These simulations indicate that the implosions are dominated by a *two-stage* development of the RT instability. In the first stage, the instability grows until the bubbles break through the compressing *plasma shell*. The shell self-heals with little plasma being sent to the axis. Acceleration of the self-healed shell continues until the bubbles again break through the shell, this time sending significant amounts of plasma to the axis, initiating the radiation pulse. The stagnating plasma achieves sufficient temperature to radiate and grows as additional plasma accretes axis from the imploding *plasma shell*.

Over the masses explored little variation in the measured total radiation

yield of ~300 kJ is measured and expected, except at the lowest mass where coupling of Saturn can no longer efficiently couple its energy to the load. However, for masses of 1.9 mg and higher, soft radiation from the accreting axial plasma is first seen, with peak power and the generation of harder x-rays occurring midway during the growth of this accretion. For masses of 1.3 mg and less, radiation is seen not only from the initial plasma accretion on axis, but also from a hot plasma shell that, together with the accreting mass, compresses to a minimum radius near the time of peak K-shell emission images. This behavior is beautifully illustrated, where both ring emission is observed at the cathode surface simultaneously with axial emission, in a sequence of large-FFPHC images that correlates precisely with the simulated mass- and current-averaged radii of the imploding shell as its leading mass begins stagnating on axis.

As the array mass decreases at this transition: below 1.3 mg the pulse width decreases by a factor of two and the total peak power radiated rises by a factor of two from 24±4 to 44±7 TW. Reducing the mass further results in no additional power gain. Like the comparison just mentioned, these observations are qualitatively consistent with those simulated [92].

Unlike the total radiated power, the K-shell yield, shows a significant increase from about 30 to about 60 kJ as the mass is reduced through the 1.9-to-1.3 mg transition [92]. The yield increase with reduced mass agrees approximately with the Mosher one-zone scaling models of K-shell (lines plus continuum) radiation. The models show that its the increase in ion and associated electron temperature that is primarily responsible for the increase in yield. The doubling of yield together with the halving of the pulse width reflects the factor of four increase in K-shell power from 2.4±0.4 TW to 11.5±2 TW that occurs as the mass is decreased over this region. *The measurements and modeling thus show the importance of maintaining sufficient KE per ion (ie sufficiently low mass) if maximum yields are to be extracted.*

Like that measured at low mass in the mass scan, in the radius scan the x-ray pulse also shows the presence of two x-ray bursts, with the first burst being significantly larger than than the second [93]. The peak of the second burst decreases and the time between the first and second burst increases with increased radius, consistent with the reduced current available to recompress the plasma column for the larger-radii, longer-implosion-time configurations. As the radius increases from 8.75 to 20 mm at the fixed array mass of 0.6 mg, the radiated x-ray pulse width at the first compression increases from 4 to 7 ns. *The r-z simulations suggest that this pulse-width increase with radius is due to the faster growth of the shell thickness*

(that arises from the two-stage development in the RT instability) relative to the increase in the shell implosion velocity.

Over the radii explored, the measured peak total x-ray power of ~40 TW and energy of ~325 kJ show little change within the 15% shot-to-shot fluctuation, and like the mass scan are consistent with the simulations. Similarly, the measured peak K-shell (lines plus continuum) power of ~8 TW and energy of 70 kJ show little change with radius. The minimal change in K-shell radiation is in agreement with Mosher's K-shell scaling models that assume a fixed radial compression for all initial radii [94].

The results suggest that the improved uniformity provided by the large number of wires and associated small inter-wire gap in the initial array reduces the disruptive effects of the RT instability observed in small-wire-number imploding loads.

4.3. SNL Transition From Light-Ion To Z-Pinches

Following our high-power aluminum results with high wire numbers, Chris Deeney (now a staff member at Sandia, formally at PI [Physics International]) doubled the total x-ray power on Saturn to 80 TW, using high numbers of tungsten wires [95]. These results further supported the increase in x-ray power with increased wire number and small inter-wire gap.

Concurrent with this research, experiments on Saturn using z-pinch x-rays explored several hohlraum concepts for ICF applications, which showed promise [96]. This work was carried out by several members of Ray Leeper's Diagnostics and Target Physics Department within the Fusion Directorate. Members included Gordon Chandler, Mark Derzon, Tom Nash, and Rick Olson.

Despite the advances in understanding the physics of light-ion beam generation and focusing, obtaining the necessary intensity on an ICF target continued to remain an issue on PBFA II. Because of the impressive results obtained with pulsed-power driven z-pinches, the near term emphasis in the pulsed-power ICF program shifted away from light-ion beams towards z-pinches [97]. In 1996, Gerry Yonas, who was now back at Sandia in the position of VP of Research, reviewed the ICF program and made the difficult decision, together with his managers, to convert PBFA II into a z-pinch driver for ICF and x-ray physics [4, 98]. A related conversion had been done earlier in 1986, when PBFA I was converted to Saturn. Gerry had started the ICF program at Sandia two decades earlier [99].

4.4. PBFA II TO Z CONVERSION

Rick Spielman, who was a z-pinch and pulsed-power expert, was put in charge of managing the conversion of PBFA II to a z-pinch driver, now called Z

(Fig. 22A) [100]). I fully supported this effort, having some responsibility in the wire-load arena. At the same time, because of my interest in fusion, I transitioned into Ray Leeper's Department. Ray was a former HEP, and now had become an expert in ICF since joining Sandia. Coming from the same physics mold, we saw eye-to-eye on the science issues that needed to be understood. We shared the same joy in solving tough physics problems. Like Wendland Beezhold, Ray was both well versed in and loved physics, was a full supporter of my research, and delighted in discussing the results. I remained in Ray's Department ever sense.

Fig. 22A Conversion of PBFA II to Z.

4.4.1. Conversion Experiments

Spielman's main thrust was to vary the z-pinch load parameters about those expected, to maximally couple the electrical power to a z-pinch load, simultaneous with upgrades to the Z pulsed-power system (Fig. 22). The Z parameters of 60 TW, with a 16-20 MA current pulse, having a rise time of ~100 ns contrast with those of Saturn who's electrical power is only 15 TW, with three times less current of 7 MA delivered to a to a z-pinch load, but with a rise time half of Z, namely ~50 ns. Like the Saturn plasma-shell loads, the Z loads used highly symmetrical cylindrical wire arrays with wire numbers ranging from 120 to 240, corresponding to inter-wire gap spacings of 0.5 to 0.3 mm, using the machined-grove technique (Fig. 20C). Here, as in the Deeney Saturn experiments, tungsten wire is use for the increased number of radiation states available.

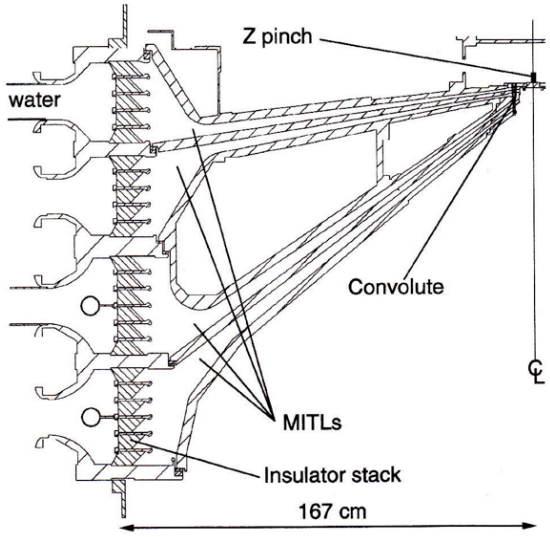

Fig. 22B Z insulator stack and MITLs.

The diagnostics were similar to many of those used in the Saturn experiments, except here the off-axis lines of sight are oriented 78° off the axis of the z-pinch. And the increased length of the diagnostic line-of-sight to 18-25 m is dictated by the extremely high source flux.

Exploring load masses from 2 to 18 mg, array diameters from 17.5 to 40 mm, and pinch lengths from 10 to 20 mm, an optimum was found using, 40-mm diameter arrays consisting of 240, 20 mm long, 7.5-μ diameter wires (4.1 mg mass). This optimum produced the unprecedented peak x-ray power of ~200 TW and an x-ray energy of ~2 MJ. The total x-ray pulse had a ~5.5 ns FWHM [100].

The optimum corresponded to an implosion time of ~110 ns. The voltage at the insulator stack between the water and vacuum of Z, typically reverses near 110 ns. Implosions that occur later than this time are less efficient because energy is flowing out of the vacuum MITLs. For implosions that occur earlier than 110 ns, the implosions occur before the electrical energy is fully delivered to the load region. Just like using ZORK to help define suitable loads for Saturn, here the Sandia SCREAMER code [101] was used by Ken Struve to model load behavior and current losses in the MITLs feeding the load. SCREAMER is much preferred over the simple lumped-element circuit code like ZORK, as it accurately treats the details of the setup of the magnetic insulation and losses in the vacuum convolute. In SCREAMER, the details of vacuum power flow react to the dynamic impedance of the z-pinch loads.

4.4.2. Wire Number Effects

Through out the scans the accelerator power was varying. A careful analyses of the data, however, showed that by normalizing the measured peak radiated power by the electrical power at the insulator stacks (Fig. 22B), doubling the number of wires from 120 to 240, but keeping the mass fixed, increased the radiated power by (35±15)% for both the 17.5- and 20-mm diameter arrays [102]. Bill Stygar, who behind the scenes was instrumental in making Z a success, provided the electrical power measurements.

George Allshouse, using the measured current as input to his 1D L-RMHD calculations, as was similarly done for Saturn [78], showed the loads are operating in a quasi *plasma shell* regime, where the individual wire plasma partially merge prior to the overall implosion of the array. In this high wire-number regime, however, the measured increase in total radiated power increase with inter-wire gap is less than half that measured for aluminum wires implosions operating in the *plasma-shell* regime on Saturn [79].

4.4.3. RMHD Simulations

Like in the Saturn experiment, Darrell Peterson, using his E-RMHD code accurately simulated the total radiated power now for two different diameters of 40 and 30 mm, with just one random density-perturbation-value [103]. The tungsten z-pinches tend to have high opacities and low temperatures, making the use of MHD approximations and the three temperature model with radiation in

the simulation adequate. Just like in the earlier simulations, as the RT instabilities grow, some of that energy ends up in non radial KE. The instabilities act to broaden the plasma sheath so that as the plasma begins to stagnate at the axis of symmetry and heat, the outer portion of the sheath is still being accelerated by the driving current. At this point the plasma is being heated not only through the stagnation, but also through pdV compression. Again the internal energy is released through radiation.

4.5. ICF Finally: The SWH

4.5.1. Saturn Data Completion

As my research on Saturn wound down and my involvement in Z increased I continued to support the spectral analyses of our Saturn aluminum data by Ken Whitney and his NRL team [84, 85], and later on Z, the spectral analyses of a few Al:Mg alloy wire array shots taken on Z. These shots were analyzed by John Apruzese and his NRL team [86, 87]. Both teams processed the extensive x-ray data collected, using their ID, cylindrical CRE model containing detailed configuration atomic structure for the Li-, He-, and H-like ionic stages of Al and Mg.

In general, the greater the mass used in a z-pinch plasma the greater the opacity of the pinch, and at some point self-absorption prevents yields from scaling linearly with mass, as the pinch transitions from a volume to a surface radiator. The results from Z indicate, for example, that this transition is well underway for the K-shell lines and continua of Al for the mass loads of 1.3-3.6 mg/cm explored. Remarkably, analysis of the one time-resolved spectrum of the 2.1 mg/cm shot, caught near the time of peak compression, yielded temperature-density profile of the pinch that approximately reproduces *all* features of the x-ray data.

Since the breakthrough, interest by other plasma physics groups, in wire-array z-pinches for fusion exploded. For example, Prof. Malcolm Haines team at IC (Imperial Colleague) was drawn into Sandia's program with Keith Matzen's strong support, bringing a great deal of technical expertise. In particular, Malcolm developed his *Heuristic Model* for wire arrays, explaining the evolution of the Saturn z-pinch with wire number from first principles [104], and Jerry Chittenden, in Malcolm's group at IC, applied his 2D simulations in both x-y and r-z geometries to providing additional insights into the wire array implosion from wires to stagnation [105]. His MD2D simulations supported Barry Marder's original division between the *plasma-wire* and *plasma-shell* regimes [78].

In these effort, I worked closely with both Malcolm and Jerry. Their work was included in an invited paper, *Wire array Z-pinch insights for enhanced x-ray production*, I presented at the 40th Annual Meeting of the APS DPP meeting

held in New Orleans 1998 [106], and later published in Ref. [117]. Over the subsequent years, like with Peterson, Apruzese, and Whitney, I continued a close collaborate with Haines and Chittenden, bringing them into the experiments I was conducting. These theorists brought tremendous insights into the data taken and helped to provide understanding of what was measured.

4.5.2. SWH Concept

As mentioned, simultaneously to Sandia's conversion of PBFA II to Z, a number of z-pinch driven ICF ideas and designs of hohlraums and capsules, for both ignition and high yield, were already underway [96, 107, 108]. The concepts employ DT cryogenic capsules (2-4 mm in diameter) that are indirectly driven by radiation fields generated by z-pinch hohlraum radiation sources. The approach is similar in concept to the indirect-drive laser approach to ICF being carried out at the NIF (National Ignition Facility). For example, Rick Olson [109] had designed a configuration, referred to as the SWH (Static-Wall Hohlraum) for the next generation accelerator, which is envisioned to have the capability to drive z-pinches to currents of 60 MA and produce x-ray yields of 15-20 MJ with powers exceeding 1000 TW. If 5-10% of this x-ray energy could be directed onto the ablator of an x-ray driven ICF capsule, Rick showed that, with his capsule design, it might be possible to obtain thermonuclear yields of ~100-500 MJ.

In his concept the ICF capsule is located in a hohlraum, sandwiched between two imploding z-pinches (Fig. 23). Here, the x-rays enter the hohlraum through REHs (radiation entrance holes) on either side of the hohlraum. Because the source region outside each REH is necessarily hotter than the interior of the hohlraum, symmetry shields are placed so as to ensure that the capsule is not driven in an excessively *pole hot* manner. In order to achieve adequate implosion symmetry, the hohlraum walls are placed at a radius that is three times the capsule radius. The two wire arrays are initially located at a diameter of ~40-50 mm and made of tungsten as in Z. Each wire array is ~10 mm long and driven with currents of ~50-60 MA.

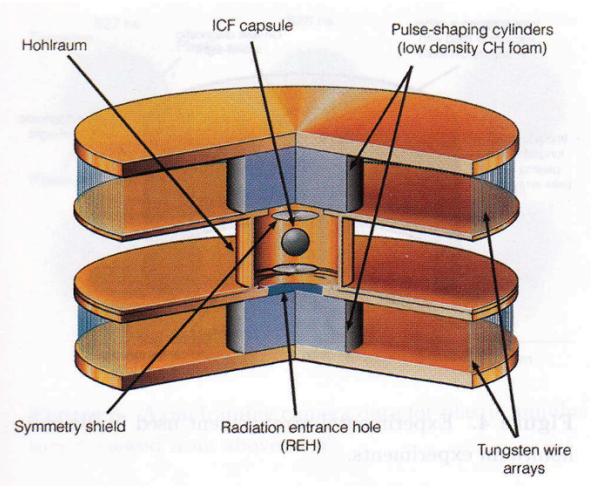

Fig. 23 Z-pinch driven Static-Wall-Hohlraum ICF concept.

As we have discussed, when the current rises, the wires are Ohmiclly heated into a plasma state at ~20-40 eV

and are accelerated radially inward by the rising magnetic field pressure to cylindrical PSTs (pulse shaping targets) which have a diameter of ~6-12 mm. When the incoming tungsten plasma strikes the PST, the interior surface of the target is heated to ~100 eV. The x-ray radiation from this moderately hot interior flows through a low Z foam of the PST and out the REHs at either end of the cylinder, heating the interior of the hohlraum to a 70-90 eV level. This process provides the 10-20 ns long *foot pulse* that is necessary to create the initial shocks of ~1 Mbar that are required to provide initial compression of the DT fuel layer. Meanwhile, the combined mass of the wire array and target wall continues to implode, providing the necessary sequence of high-intensity *peak pulses* of x-ray input as it stagnates on axis. The x-ray input from the *peak pulses* needs to be in the range of ~300-600 TW in order to heat the hohlraum to peak radiation temperatures of ~250 eV, which is that required to achieve the final implosion velocity necessary for ignition.

4.5.3. One-Sided Drive Experiment

This approach, where the optimization of the z-pinch x-rays is isolated from the optimization of the radiation field imploding the capsule, made sense to me. Rick Olson and I decided to join forces: I knew about z-pinches and Rick ICF physics. Once Z became available for users, we launched an set of experiments to first demonstrate that a z-pinch could indeed heat a NIF-scale hohlraum to temperatures characteristic of a *foot-* and a *first-peak* pulse and later to a *second-peak* pulse in a reduced size hohlraum. In these experiments only a one-sided drive was explored (Fig. 24).

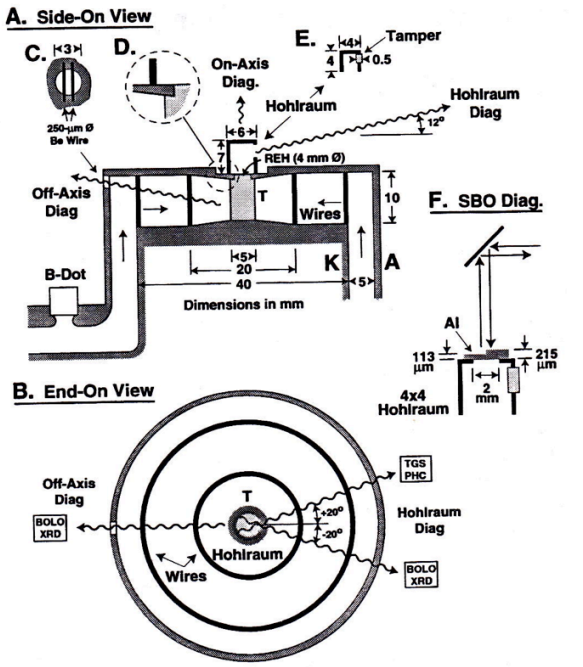

Fig. 24 One-sided Static-Wall-Hohlraum arrangement on Z illustrating (A) side-on view with NIF-scale hohlraum, (B) end-on view, (C) off-axis diagnostic aperture, (D) 3° anode glide plane, (E) reduced scale hohlraum, and (F) shock-breakout diagnostic with reduced-scale hohlraum. The cylindrical target and radiation entrance hole are indicated by T and REH, respectively.

The hohlraums used are 25.4 μm thick walled gold cylinders, measuring either 6-mm in diameter by 7-mm in hight (NIF ignition scale) and later 4-mm in both diameter and height. The hohlraums are empty except for the small hohlraum.

The hohlraum temperature is measured with two independent diagnostics, each of which views the interior wall of the hohlraum through the same aperture (~3-mm diameter for the 6x7-mm hohlraum or 2-mm diameter for the 4x4 mm hohlraum). One measurement uses a TGS (transmission-grading-spectrometer), and the other uses a total-energy bolometer and filtered x-ray diodes (Fig. 24 B). The peak measurements agree to ±3%. The spectrometer was developed by John Porter and fielded by both Larry Ruggles and Walt Simpson in his group. Plasma closure of the diagnostic hole with time is measured with a multi-filtered, FFPHC sensitive to x-rays in four discrete spectral channels covering 100 to 600 eV. For the measured temperatures, a correction for the reduced hole size with time based on these images is used. For the 4x4-mm hohlraum a 5-mg/cm^3 CH foam is placed in the hole to retard hole closure (Fig. 24E). For this hohlraum, the temperature was confirmed by an active shock-break-out technique (Fig. 24F) developed by Rick Olson [110].

The radiation entering the hohlraum through the REH is measured by an additional suite of on-axis diagnostics, developed by Tom Nash, when the hohlraum was not present. These diagnostics include include a total-energy bolometer, a filtered XRD set, and a filtered FFPHC similar to those detectors of the horizontal diagnostic sets.

The first PST used a 2-μm thick copper cylinder with a diameter of 8 mm. The interior of the PST cylinder contains10-mg/cc CH foam fill. The diameter is matched to the calculated implosion velocity after (the tungsten shell impacts the PST (first strike) in such a way that the *foot-pulse* radiated is generated for >10 ns before final stagnation occurs. Copper is selected because its high density thermalizes the incident wire-plasma kinetic energy in a short radial distance, and for its sub-keV opacity characteristics, which allow the PST interior to fill with radiation before final stagnation occurs. The power being produced in compressing the foam helps to maintain the duration and temperature level of the foot pulse prior to stagnation. The radiation exits the imploding PST through a top, 5.8-mm diameter REH that connects the PST with the hohlraum.

After trial experiments with a few tungsten-wire load geometries, we settled on a load configuration that permitted the hohlraum to be adequately heated for the duration required for the foot pulse. The configuration used a nested array of tungsten wires mounted at diameters of 40 and 20 mm, having a length of 10 mm [111]. The outer and inner arrays are composed of 240 and 120 wires, and have masses of ~2 and ~1 mg, respectively. This load configuration had been found by Chris Deeney to generate 40% higher powers than a single array when the wires stagnate on axis without a target. The associated inter-wire spacing

is ~0.5 mm of both arrays, and forms a quasi *plasma-shell* in the outer array prior to first strike on the inner array. The inner array resets the RT instability in the imploding outer array.

With this arrangement, we produced a hohlraum temperature of 85±5 eV, for a duration of ~10 ns prior to final stagnation. The energy distribution is measured to be Planckian. Importantly, the initial temperature profile generated prior to stagnation corresponds approximately to the conditions required for a f*oot-pulse* drive. With such a *foot-pulse* source, ablator physics, helium-filled wall tamping, hole closure, and other issues associated with ICF implosions on NIF could be studied under realistic pulse-temperature, pulse-length, and hohlraum-size conditions on Z [112, 113].

With this success we explored other PST configurations necessary to simulate the higher-power next temperature steps. With a 5-mm diameter foam target of higher density 14 mg/cc (but no copper shell) and now with a 3-mm diameter REH, for example, we produced a peak hohlraum temperature of 122±6 eV with a pulse shape characteristic of the next *first-step* pulse in the NIF scale hohlraum. The use of the low-density foam target decreases the radial extent of the final pinch at stagnation by roughly two, relative to that measured for targetless (bare) pinches to only a ~2-mm diameter. The target likely acts to mitigate the RT instability much like the inner array does when impacted by the outer array of the nest. Because of the radial-size reduction, similar x-ray powers are generated through a 3-mm diameter REH when using the foam target, as are generated during a bare pinch viewed through a 6-mm REH.

Again, using the foam target with a 3-mm REH, the small 4-mm diameter hohlraum, was driven to a peak temperature of ~158±8 eV, characteristic of the *second peak* temperature drive needed. Over the range of x-ray powers (P) of 0.7 to 13 TW exiting the REH that we explored in four discrete steps, the associated hohlraum temperature (T), of 60 to ~160 eV measured in our two sized hohlraums, scaled beautifully as the Plankian relation $T \sim (P/A)^{1/4}$. This expectation gave us confidence in these difficult measurements. A is the surface area of the hohlraum.

The experiments showed, *for the first time*, that the x-ray outputs available in pulsed-power driven z-pinches enable hohlraums of full NIF ignition size to be heated to radiation temperatures and time scales comparable to those required for the lower-power *foot-pulse* drive and for a *first-step* pulse drive, as well as a reduced-scale hohlraum to be heated to temperatures corresponding to a *second pulse* drive. The initial results were summarized in a letter, titled *Z-pinch-generated x-rays demonstrate potential for indirect-drive ICF experiments*, which I submitted to PRL in July 1999. Publication followed 5 months later [112].

4.5.4. SWH Understanding

Following our initial measurements, we expanded our measurements and analyzes bringing in Darrell Peterson, and now also Richard Bowers and Walter Matuska, also from Los Alamos [114]. As before, Darrell simulated the implosion using his E-RMHD code [103], but now Richard was able to continue the evolution of the radiation and material flow into the hohlraum and the subsequent heating and motion of the of the hohlraum walls using the L-RMHC code. Walter evaluated the resulting closure of the small side hohlraum diagnostic hole. And again Ken Struve provided help with the SCREAMER simulations of the power flow to the load. In SCREAMER the implosion of the two arrays and target are handled with a 0D model that calculates the acceleration and collision of infinitesimally thin plasma shells consistent with the drive current and increasing load inductance. When the two shells collide, momentum is assumed conserved and the mass of the of the inner shell is accrued to the outer one, which continues to accelerate inward to the next collision with the PST. Up until the measured peak current of ~21 MA and well past, both simulations give remarkably good agreement with the measured current. As was done earlier in the Z simulations, Darrell used a simplified version of the SCREAMER circuit model of the Z accelerator to drive the implosion.

The RMHD models provide insights into the dynamics of the wire-array implosion, target compression, heating, x-ray generation, and plasma flows, and now the subsequent heating and motion of the hohlraum wall. The modeling suggests that the impact of the outer array on the inner generates a low-level radiation pulse that gives rise to ~30 eV radiation temperatures within the hohlraum that lead to diagnostic hole closure rates of ~0.02 mm/ns for the ~15 ns prior to the combined arrays impacting the PST. After impact, the closure rates increase to 0.02-0.07 mm/ns and are in agreement with those measured. The upper end of these measured rates is within a factor of two of the ~0.14 mm/ns calculated motion of the gold-vacuum interface within the hohlraums. The calculations show that the wall motion can be significantly reduced by the addition of low-density foam without a significant drop in hohlraum temperature, as measured. Using 6 mg/cm^3 CH fill in the small hohlraum, for example, reduces the calculated wall motion by ~40% and the calculated and measured temperature by only 3-5%.

The simulations also suggest that the hohlraums remain relatively free of z-pinch plasma until after stagnation occurs. The plasma fill that does occur is principally that of the lower opacity foam with densities typically of the order of 10^{-3} g/cc.

These additional measurements and simulations reaffirm the utility of these hohlraums as useful environments for studding the characteristics of ICF relevant hohlraums under *first*- and *second*-step temperature conditions. The results were summarized in a paper titled *Dynamics of a z-pinch x-ray source for heating inertial-confinement-fusion relevant hohlraums to 120-160 eV,* which I submitted to POP July 2000, and which was accepted for publication the following month [114].

4.6. Recognition

At the 40th APS DPP Meeting of November 1998 in New Orleans, over dinner David Mosher suggested that he would like to nominate me for Fellowship in the APS. I was greatly humbled by his suggestion. David followed through on his suggestion, and at the 42nd APS Meeting in October 2000 Quebec City, Canada I found myself elected as an APS Fellow, in large part due to David's efforts. The Certificate of Fellowship read:

For fundamental advances in understanding of wire array z-pinches, which led to improved load symmetry and greatly increased radiative power, and opened up the possibility of using wire arrays as drivers for inertial confinement fusion.

Hearing of this news, Gerry Yonas (now VP of Research at Sandia) wrote me this brief letter:

Dear Tom,

Congratulations on your recognition by the APS. You made the discovery that changed the entire field, and you should be very proud. I am personally very grateful.

Sincerely,

Gerry

This meant a great deal to me, as Gerry was the mover-and-shaker of the fusion effort he initiated at Sandia several decades ago [99]. Moreover, this recognition meant that I had finally arrived at making a contribution to the fusion program, which I had dreamed of contributed to, so many years earlier. In my wildest thoughts, however, I had never conceived that z-pinches could be at the heart of the current Sandia fusion program.

5. DYNAMIC HOHLRAUMS

After our initial studies with the SWH, my interest migrated to understanding the radiation generated within the PST and exiting the top REH itself. Rick Olson returned to his earlier NIF studies. *The intense radiation leaving the 3-mm diameter REH using the 5-mm diameter foam target was unique, being the brightest x-ray source available in the laboratory to date.* It was of utility to a Los Alamos's Experimental Group, under Bob Chrien and Bob Watt including Darrell Peterson, for study of high energy-density physics and radiation transport issues at drive temperatures in excess of 200 eV.

The PST is basically a DH (Dynamic Hohlraum), one of the geometries being considered for imploding an ICF capsule when placed at its center [107,108]. Because of the high temperatures produced within its interior, this concept is a leading candidate for ICF using z-pinches.

Completing our SWH studies, it was thus natural to turn my attention to characterizing and understanding the radiation flow within the SWH PST (now referred to as the DH) interior and later to optimizing the wire-array drive itself. It is in this part of the ICF program that I spent the remainder of my years at Sandia. Understanding its characteristics and unlocking one of its secrets, namely the *up-down radiation asymmetry*, occupies the rest of this report.

5.1. Geometry and Modeling

Here I worked closely with the Los Alamos team and again with Darrell, who had become a close associate in all of my z-pinch research. At this point, Ray Lemke of Sandia also joined my team, bringing the capability of running a different Eulerian RMHD code to the study of the physics of the implosion in the r-z plane. Darrell's code, as mentioned, used a three-temperature (one each for ions, electrons, and radiation) approximation along with radiation diffusion. Ray's code, in contrast, employed multi-group, flux-limited diffusion in its radiation transport. This second code may be expected to more accurately model the radiation transport, and is referred to as MG-RMHD. In either model, it is assumed that the wire arrays can be represented as annular plasma shells with initial temperature of ~1 eV, and an initial random density perturbation is applied to only the outer shell.

Again, the geometry used for our DH characterization studies used the standard nest of 10-mm high tungsten wire arrays having masses 2 mg and 1 mg at radii of 20 and 10 mm, respectively. And again, the target was made of a solid cylinder of 14 mg/cc CH foam with a diameter of 5 mm. Its mass approximately equals the combined mass of the two tungsten arrays. As with the SWH experiments, this research was made possible by the generous support

of both Keith Matzen and now John Porter. Keith fostered the Los Alamos connection, and John was now managing the over-all Dynamic Hohlraum effort.

5.2. Current Return Shell

Commonly, current-return metallic shells surrounding pinches have been constructed with periodic slots to enable viewing the radiation generated off-axis to the pinch. Such structures introduce periodic azimuthal variations in the magnetic field accelerating the wire arrays. They may introduce degradation in the quality of the implosion. Periodic structure in the imploding shell is both measured [115] and expected [116]. Because we were primarily interested in the axial radiation, this periodic structure was initially eliminated by replacing the standard current return shell with one having no slots (with only a small hole to monitor the radiation from the pinch [Fig. 24C]). The diagnostics were thus designed to measure primarily the axial radiation exiting the REH. These diagnostics, which were similar to those used in the SWH experiments, provided a view of the interior of the hohlraum itself as it imploded.

Further investigations revealed, however that no axial power loss resulted from the azimuthal perturbation when return conductors with twice the standard number of slots (a total of 18) were used. Thus in subsequent shots, the solid current-return shell was replaced with one having the increased number of slots. The replacement allowed measurement of the radiation emitted external to the pinch in the radial direction from the base-line DH target (Fig. 25 A and B) as well as diagnostic access for measurements of the imploding plasma as it impacted the inner array. Again, the diagnostics employed were similar to those used for the axial measurements.

5.3. Measurements

The measurements [118] indicated that the implosion exhibits three distinct phases once the tungsten plasma impacts the target, referred to as FS (first strike). In the first of these, referred to as the *dynamic hohlraum* phase, radiation is trapped within the converging target. The second phase, referred to as *stagnation*, includes the deceleration of the tungsten plasma and the thermalization of the KE of the combined tungsten and target plasma on-axis. In the third phase, referred to as *expansion*, the hot plasma expands against the compressing magnetic field. Later compressions and expansions may follow as observed earlier in the Saturn *plasma-shell* implosions [89].

Stagnation corresponds to the peak of the radial emission, which is typically 140±31 TW. Despite the 20% variation in peak value, the shape of the radial pulse is stable. FS occurs ~4.9 ns prior to stagnation, with the peak of the measured axial power occurring near the

end of the *dynamic hohlraum* phase, when the *stagnation* phase begins to set in. The inside radius of the hohlraum is ~0.35±0.15 mm at this time, the average temperature of the hohlraum interior is ~230±15 eV, while that of its exterior is ~190 ±15 eV. At this time the high-opacity tungsten at the tungsten-CH interface begins obstructing the flow of radiation through the DH and out the top REH.

The associated axial power pulse is remarkably reproducible, having a rise-time of 2.7±0.3 ns, a pulse-width of 4.5±0.7 ns, a peak value of 9.7±1.8 TW, and energy 52±10 kJ. For the most part, the field exiting the REH is consistent with that of a Planckian distribution. Above 1.5 keV, however, the distribution deviates from Planckian. At peak axial power, this high-energy portion of the spectrum contains about 6% of the power.

5.4. RMHD Simulations

The RMHD simulations [118] indicate that the axial radiation is dominated by emission from a radially converging shock in the foam generated from the FS. The radius of this annular shock as well as the radius of the DH exterior photo-surface as a function of time are in excellent agreement with those measured prior to stagnation. Experimentally, however, the hohlraum converges to only a fraction of the simulated radii, namely 0.5 mm. In the simulations the load remains compressed, whereas, experimentally, the load expands after stagnation. This difference may be indicative of current shorting at the AK gap or 3D effects not included in the 2D simulations or the approximations used in the radiation modeling discussed earlier.

At earlier times in the experiments, the impact of the outer with the inner array (denoted by O/I) occurs within 2 ns of that calculated by the SCREAMER and RMHC models. The energy radiated at the O/I collision is consistent with that simulated by either model, but not its peak power. Here the collision is assumed to be inelastic *hydrodynamic.* The radiation continuum measured prior to and under the O/I radiation peak, is also significantly higher than that calculated arising from Joule heating and interactions with the inner array and target plasma blow-off. The measurements are thus suggestive of imploding array plasma interactions with a possible pre-fill of plasma injected into the interior of the array at early time. (More on this later.)

In the simulations, target preheating arises from radiation generated from the Joule heating and from the O/I collision. In the E-RMHD model, the O/I radiation generates a radiatively driven shock in the target that converges on the z-axis ~4 ns prior to final stagnation. Experimentally, a weak enhancement in the on-axis emission is measured at this time. In the MG-RMHD model this enhancement is reduced

owing to the more distributed nature of the heating arising from the spectral range of the emission. In general, either model tends to overestimate the magnitude of the pre-FS emission, implying that the target blow-off is less than that calculated.

In general, the two RMHC models provide relatively consistent descriptions of the implosion, as well as qualitative agreement with the measurements prior to the stagnation. Both models, however, required a significantly reduced RT seed (relative to that previously used to simulate the radial radiation power from targetless pinches) to adequately describe the shape and magnitude of the axial radiation power, which is produced by shock heated foam. Under this condition, however, the calculated magnitude of the peak radial radiation is significantly higher than that observed. The overestimation may relate to details of the array-foam plasma interaction, and/or 3D effects (especially near the z-axis) not included in the 2D modeling.

5.5. Azimuthal Structure

In fact, a careful examination of the axial emission near stagnation exhibit a 6±2 azimuthal mode structure in shots having a solid current return shell (Fig. 24C) [119]. This mode number was observed in both the targetless and foam target implosions. In the loads (as in all our Z loads) the wires are held in position within narrow slots at the given radii to a radial and azimuthal tolerance of ±75 μm. This uncertainty in azimuthal location could lead to as much as a ±30% variation in inter-wire spacing. Within this tolerance, groups of wires could also be systematically pulled to to one azimuthal side of a slot or the other side of a slot with a mode number of between two and four. In contrast to the high-degree of azimuthal symmetry of the current flow, the discrete nature of the wire array itself has the potential to provide substantial seeds from which instabilities in the r-θ plane could grow.

To investigate the r-θ asymmetries measured, a series of 2D numerical simulations was conducted by Prof. Norman Roderick of the University of New Mexico, using the MACH3 code [120]. The simulations followed the implosion all the way through the collision with the inner array and to the final compression of the target on axis. The simulations indicated that if a six-fold mode number was present in the initial density distribution it would remain, amplifying as stagnation is reached. Alternatively, the simulations showed that if a random density with a slightly higher mode number were initially present (as could possibly be generated from the wire array itself), the associated mode number would be reduced during the implosion, and approach the experimental mode number of about 6±2. Interestingly, a similar mode structure developed in some of the earlier TIP numerical simulations of the Saturn aluminum wire arrays,

which assumed a random density distribution in the initial plasma shell [80,106]. The underlying mechanism that develops these azimuthal asymmetries is not understood, however, whether it is caused by simply radial convergence effects arising from imperfect wire-array shells, or from the growth of some RT instability. The impact that these measured and simulated azimuthal asymmetry observations have relative to the instabilities known to develop in the r-z plane, in terms of potentially reducing radiation output at stagnation or spoiling the radiation symmetry needed for ICF applications, was not further evaluated at this time.

5.6. Single vs Nested Arrays

As mentioned earlier, the radial power power was measured to increase with the addition of an inner array to form a nested array of wires for targetless pinches [111]. This arrangement, where the inner array has half the diameter and mass of the outer array had become the standard driver for much of the DH research at Sandia. The addition of the inner array, however, complicates practical designs of many ICF concepts that utilize two z-pinches to drive a secondary hohlraum. (See Fig. 23 for example.) In such configurations, the secondary is sandwiched between the pinches. Moreover, our earlier comparisons of the NIF-scale hohlraum temperature, when driven by either a single array with that of the standard nested array showed only similar temperatures within large uncertainties [112]. In this case, the target was a copper-clad foam target of length 20 mm, used for the *foot-pulse* simulation. It thus made sense to recheck if the use of the nest, with its complications, still provided a superior driver for our 10-mm high DH.

As an additional motivator, the MG-RMHD simulations showed that the single array might potentially generate ~50% more axial power when the mass of the single array was doubled beyond that which matched the total mass of the nested array [121]. The E-RMHC simulations indicated some what less gain, perhaps as much as ~20% depending on the roughness of the inside surface of the W/CH interface assumed within the hohlraum. The increase results from the improved radiation trapping due to the thicker tungsten shell and the reduced RT growth.

Accordingly, after our single wire mass scan from 2 to 3.5 mg in 0.5 mg steps, using the 5-mm foam target we extended our scan from 4 to 6 mg in 1 mg steps [121]. The small increase in axial power and radial power measured of (23±15) and (16±15)% , respectively, with the nest relative to the single-array with a mass of ~3 mg was consistent with either model, depending on the size of the random density seed used. *The factor of two decrease in the measured axial and radial power for masses of 4 mg and greater, however, was completely*

unexpected from either model [121]. They had never failed to provide good insight in the past. Based on the modeling, I had strongly advocated extending our scan up to 6 mg, and had made a bet with Keith Matzen that we would significantly increase the axial power by doubling the mass to ~6 mg. *I lost the bet big time, and had to buy Keith a double decker ice cream cone, the wager of the bet.* This was a serious blow to our understanding, and suggested that important physics was being left out of our modeling. I will come back to this difference near the end of the report, where we investigated if our assumptions of a *hydrodynamic* collision between the outer with the inner and of power increase with wire number was correct.

5.7. Length Scaling

In an effort to study the scaling of the axial radiation power with length, and better understand its production, the length of the 10-mm long DH was varied from 5 to 20 mm, keeping the mass/unit length constant [122]. The basic configuration is that used before with the solid current-return can having a small peep hole to permit the radial emission to be observed (Fig. 24C). Not previously mentioned, but used for all the previous hohlraum experiments, the target foam extends into and tamps the REH to retard aperture closure. The slope of the array glide plane between the inner array and the REH is set to 3° to prevent sliding of the tungsten plasma across the REH (Fig. 24D).

E-RMHC simulations suggested that the axial power might be increased by as much as ~30% if the length were to be reduced from 10 to 5 mm. A maximum in axial power of only ~10 TW is measured, however, at a length of ~7.5 mm. This power is only slightly higher than the typical power for the 10-mm length baseline (Fig. 25B). The linearly decreasing axial power measured for lengths longer than 7.5 mm at a rate of 0.65 TW/mm is, never-the-less, nicely bounded by the E-RMHC simulations that include variations in the roughness of the tungsten-foam interface. *Like the large decrease in power at high mass, however, the precipitous decrease in measured axial power of a factor of two, for the 5-mm length was unanticipated based on the modeling* [122]. At the time, we thought the decrease may be due to electrode and associated instability effects, which would spoil the quality of the implosion near the REH, and which may dominate the bulk of the pinch at the shorter length measured.

5.8. Unexpected Axial Asymmetry Measured

5.8.1. Expectation

Our simulations of the z-pinches employ the MHD approximation. This assumption is reasonable because the bulk dynamics occur in plasmas with sufficiently high density that charge-

separation effects and intrinsic polarity-dependent electrode effects are thought to be small. Under these approximations, our RMHD simulations show no systematic difference in powers exiting an REH, independent of whether the REH is located in the anode (top) or cathode (bottom) . Because the bulk of the power exiting the top REH comes primarily from the upper 5 mm of the target, the addition of a bottom REH should have no effect on that being emitted from the top. Because of assumed up/down axial symmetry then, a measure of the power exiting a bottom REH should thus provide a measure of the power exiting the top REH (Fig. 25A), and be a useful diagnostic for establishing the power exiting the top REH. So our reasoning went.

5.8.2. Measurements

Tom Nash of Sandia had developed a diagnostic suite to measure the radiation exiting a bottom REH, similar (but not absolutely identical) to that he had developed for the top REH. Contrary to expectation, our initial measurements, using the bottom diagnostic suite showed a significant asymmetry. These early measurements were done during our single-array mass scans [121], and were not the focus of the scans. I felt fairly confident in the measurements, but not all that confident to publish the results until they could be rigorously verified. Such an asymmetry, if true would be a big deal, and imply new physics associated with the implosion not included in the simulations. Unexpected symmetries in particle physics had always lead to big discoveries, such as CP violation, which indicated that weak interactions in matter differ subtly from those of antimatter.

Moreover, my Los Alamos experimental colleagues were convinced that I was making a mistake some where in our analyses of the measurements. The detectors were not at the same distances or angles with respect to the z-axis from the respective REHs, nor did they have similar sensitivities.

Accordingly we rebuilt the bottom diagnostics to be physically as close as possible to those of the top suite and dedicated four-shots to establishing the validity of the asymmetry. The load geometry used was what now had become our standard DH configuration for our Los Alamos experimenters, namely the 5-mm diameter, 10-mm high CH target driven by the standard nested array (Fig. 25 A and B). In the shot sequence, the detectors on top were exchanged with those on the bottom in alternate shots. T*he average of the measured top-to-bottom ratio of the peak power and energy for the four shots were 2.0±-0.2 and 1.2±0.2, respectively.*

These measurements confirmed our earlier observations of a factor of two difference between top and bottom powers made during the mass scan. Interestingly, the shapes of the top and bottom signals up until ~2 ns past

stagnation look remarkably similar. It was as if something was covering the bottom aperture during the implosion. For these shots (72±3)% of the radiated energy is emitted earlier than 2 ns (after stagnation) through the top REH, whereas up to this time only 49%±2% is emitted through the bottom REH. The excess late-time emission, relative to the top, compensates, in part, for the lower initial emission, bringing the total energy emitted on the bottom to near that measured on the top.

5.8.3. POP Publishes Anomaly

I thought that this experimental result deserved a submission to PRL. Although we proposed several possible mechanisms responsible for the asymmetry, we had no proof that any of them could be responsible. As a result, despite the potential importance of the asymmetry to the ICF and the plasma physics community, the submission was rejected by PRL. Implicit in many ICF applications is the assumption that relative to the center of the hohlraum, the generation and flow of radiation would be symmetric about the z axis.

Not detoured, I quickly reformatted the letter without a word change, and sent it off to POP in January of 2003. It was accepted as a letter the following month [123]. We clearly had our work cut out for us, however, if we were going to get the observation into PRL.

5.9. Understanding

5.9.1. Tungsten Measured in REH

To gain understanding of the nature of this unexpected axial asymmetry the instrumentation of the top and bottom diagnostics suits were spruced-up [124]. This instrumentation included both time-resolved and time-integrating crystal spectrometers covering the range 1.4 to 4 keV, and a FFPHC. Al and Mg tracers, symmetrically placed about the mid-plane of the target together with measurements of associated K-shell line absorption spectra, enable the energy dispersion of the spectrometers to be calibrated [125]. Additionally, the diameters of the top and bottom REHs have been expanded to from 2.4 mm (traditionally used for the high-temperature radiation flow experiments of Los Alamos) to 4 mm to facilitate greater spatial viewing of the implosion.

The shots taken with these additions show a preponderance of tungsten radiation originating near the bottom of the REH relative to the top REH in both the time-integrating and time-dependent spectrometers. This radiation is easily identified by the characteristic M-shell emission (2-2.4 keV) from hot tungsten plasma superimposed on a Planckian continuum. The top spectra indicate little M-shell tungsten emission through peak axial power, whereas significant M-shell emission is measured at the bottom for all times.

In general, peak axial powers, whether measured from the top or bottom, anti-correlate with the amount of M-shell tungsten measured at peak power. Another feature of the data, is that at early times (8 ns prior to stagnation) M-shell tungsten emission is observed in both the top and bottom spectra. However, always greater tungsten emission is observed earlier in time on the bottom than on the top.

5.9.2. Pedestals Limit Tungsten

Adding annular pedestals (thin metal rings raising the cylindrical foam target away from the electrode surface) just outboard of the REHs (Fig. 25C), intended to prevent tungsten wire-array plasma near the electrode surface from prematurely crossing the REH, significantly reduced the M-shell emission on the bottom relative to the top [124]. The resulting improvement in top-bottom radiation symmetry measured with these pedestals suggests that the asymmetry measured in the baseline configuration may be due, in part, to localized opacity effects near the given REH resulting from differing amounts of tungsten that attenuates the internal emission from the DH and reduces the radiation exiting the REH.

Initially, 3-mm high pedestals were mounted above and below the cathode and anode, respectively, and the target was then held within the pedestal structure in a manner similar to that used for the baseline target, For this arrangement, the AK gap was increased from ~10 mm to ~14 mm, to accommodate an 8-mm long target. As we discussed, this reduced target length had previously been found to maximize the top axial power [122]. The shorter target also helped to minimize the increase in load inductance due to the addition of the pedestals. Other pedestal lengths of 0.4, 1, and 2 mm were also fielded on the bottom with no pedestals on the top.

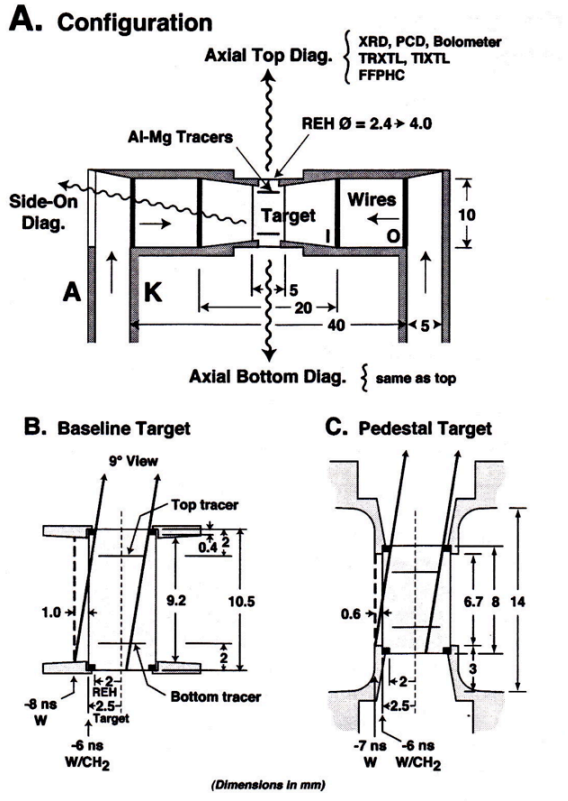

Fig. 25 (A) Baseline wire-array drive on Z (B) using baseline target, and (C) pedestal target. Dimensions in mm.

M-shell emission earlier than 4 ns prior to stagnation results from tungsten sliding along either electrode surface a

few millimeters in front of the main body of the plasma shell. The effect of this plasma is removed by the use of the 3-mm high pedestals. The 3-mm pedestals generally equalize the top and bottom axial powers. Pedestals 2-mm high on the bottom were approximately sufficient to normalize the top and bottom pulse shapes. On average, the application of the 3-mm high pedestals on both electrodes resulted in an average peak power reduction of (36±13)% out of the top, relative to the previous baseline geometry. With these pedestals on both electrodes, four shots gave an average top-bottom power ratio of 1.08±0.1. Even with the pedestals, however, a slightly greater tungsten fraction is inferred to be present on the bottom, which gives rise to the increased rise time of 0.5±0.1 ns of the bottom axial power and the delay of its peak axial emission of 1.1±0.3 ns relative to the top.

5.9.3. Nash Model

Tom Nash developed a three-component temperature model sufficient to simulate the major spectral features measured [124]. The model demonstrates that if less than 2.5 % of the initial tungsten mass were covering the bottom REH, then this fraction would be sufficient to reduce the over all thermal emission from the hohlraum by the measured factor of two, and generate the general spectral features seen above 1.3 keV. The model in combination with the spectral measurements thus gives credence to the suggestion that it is the difference in the magnitude of the tungsten plasma obstructing the REH that is the likely mechanism for the variation in top-bottom axial powers.

The mechanism responsible for the excess tungsten appearing at the bottom, however, is unknown. Instabilities between the wire-plasma and the electrode walls, and or those induced by asymmetries in the radial power feed offer potential explanations, but are somewhat inconsistent with other aspects of the data. Specifically, high-spatial-resolution simulations of the plasma-wall instability, by Ray Lemke and Darrell Peterson, suggest little axial power asymmetry resulting from such interactions within the radius of the inner array, and in particular at the REHs. These simulations ruled out the suggestion by Malcolm Haines that Hall currents could effect the plasma dynamics at the REHs [123, 124].

5.10. Continued Understanding

5.10.1. New Experimental Arrangement

To further elucidate these observations, FFPHCs were mounted exactly on the z axis above and below the target, and a variety of Al and Mg tracer combinations and positioning within the DH were used in conjunction with our spectrometers [126]. Placement was at either the REH exit (outer) or 2-mm interior (inner) to the exit, or at both locations. Both the baseline as well as

the pedestal targets were used. Now the purpose of the tracers was to also asses the temperature of the surrounding foam plasma and to look for any temperature differences between the top and bottom of the target, which might signify other differences in the implosion dynamics.

Detailed atomic modeling by John Apruzese, using his numerical model [125], shows that during the *DH phase* of the implosion (6 ns prior to stagnation to stagnation), the temperature and density conditions of the target (and associated tracers) are such that He- and H-like K-shell line emissions and absorptions in the spectrum can both be generated and observable in our spectrometers, before being blocked by the increasingly higher opacity of the tungsten-compressed foam between the tracers and the REH. Tom Nash, using 1D L-RMHC simulations showed that the radiation temperature at the position of the tracer layers quickly equilibrates to that of the surrounding foam. Complementing these tracer temperature tracer measurements, the on-axis FFPHC (within the two axial suits) provides images interpreted as the imploding shock viewed from either end of the hohlraum.

5.10.2. Temperature

As previously discussed the intense annular rings measured in the FFPHC have been correlated with the position of the imploding shock, with the FWHM of line-outs of the rings corresponding to the radial position of the W/CH interface, and with the shock preceding the interface by 0.3-0.5 mm. These expectations are again born out here (using the top diagnostics with the pedestal target) by the excellent agreement when the FWHMs are compared in detail with Darrell's E-RMHD simulations during the DH phase of the implosion. Moreover during this phase, the *brightness* temperature of the shock extracted from the images, like the radial comparisons, are in excellent agreement with his simulations.

Additionally, a *color* temperature of the hohlraum interior is obtained from a fit of the shape of the Planckian distribution to the measured continuum between 1.4 and ~2 keV. A detailed comparison of this *color* temperature, with the brightness temperature with the *tracer* temperature extracted from John Apruzese's numerical model of the measured spectra are all in agreement within experimental uncertainties, during this *DH phase* of the implosion. Over this phase, the temperature increases from ~160 eV, 6 ns prior to stagnation, to ~250 eV, 2 ns prior to stagnation.

The general agreement among the differing techniques and with the RMHC simulations, supports the accuracy of the *tracer* technique itself and increases confidence in the inferred over-all high temperature of the DH [126]. The techniques all break down once peak power is reached. After this time, and as stagnation is approached, local hot spots begin to dominate the emission, as the

tungsten plasma begins to thermalize on axis. Fortunately, it is the behavior of the DH up to peak power that is of importance to ICF and radiation flow experiments that utilize the radiation exiting the REHs.

A numerical model analyses of all 16 tracer measurements, gives an average of the ielectron temperature at the DH center of 259±15 eV, with the electron temperature at the REH of 200±8 eV and associated radiation temperature of 205±7 eV, at peak power [127]. Here the uncertainties correspond to the uncertainty of the averages. These averages suggest the presence of an axial temperature gradient within the hohlraum. This is to be expected. Such a gradient arises, because the loss of radiation through the REHs cools the plasma near the ends of the hohlraum. And again, the average temperatures measured are consistent with and bounded by the E-RMHD simulated axial temperatures at peak axial power.

5.10.2. Shock

The measured diameter of the inferred W/CH interface of the top and bottom REH images track each other throughout the *DH phase*, independent of target type [126]. For example, the interface crosses a 2-mm diameter at 3.3±0.3 and 3.0±0.3 ns (prior to stagnation) for the top and bottom images, respectively. No difference outside of ±0.3 ns between either target type is noted. The eight measurements used for these averages illustrate the typical shot-to-shot reproducibility of the interface diameter with respect to stagnation.

Like the diameter of the interface, the diameters of the imploding shock measured from the top and bottom images track each other, and show a remarkable degree of azimuthal symmetry. Here the shock diameter is defined as the average distance between the left and right peaks in the x and y line-outs that pass through the pinch center.

Like the measured radii, the top and bottom *brightness* temperatures agree with one an other at the time of peak axial power, except when there was excessive tungsten plasma measured in the bottom REH degrading the brightness temperature. When the *brightness* temperatures are contrasted with the *tracer* temperatures near peak axial power, there is qualitative agreement. On average, for all five comparisons using the *tracer* technique, the top-to-bottom ratio of the *tracer* radiation temperature is 1.02±0.04 near peak axial power.

5.10.3. Top-Bottom Dynamics Similar

The pedestal target exhibits minimal tungsten opacity effects in contrast to the base-line target, yet the dynamics between top and bottom of either target appear similar. I*n general, the similarity of these top-bottom W/CH interface and shock radii and temperatures continues to support the contention that it is the asymmetry in*

opacity from the small fraction of the tungsten wire array plasma near the REHs, rather than any significant axial asymmetries in the basic dynamics of the implosion that is responsible for the bulk of the axial power asymmetry [126].

The introduction of the pedestals to remove any wire-array plasma from prematurely crossing the REH close to the electrodes, has improved the shot-to-shot reproducibility of the axial radiation pulses and their top-to-bottom symmetry, and reduced the power profile rise times. These improvements suggest that the quality of the imploding plasma shell, which forms within the central 50-60% of the axial length, is superior to that which forms closer to the electrodes, in particular, the bottom (cathode).

5.10.4. Early Shock Observed

In all top and bottom FFPHC images at times on the order of 6 to 4 ns prior to stagnation, a significant simultaneous enhancement of x-ray emission is measured on axis prior to stagnation of the mass driven shock. Related emission has been observed in the top REH, using two FFPHCs viewing the pinch stereoscopically at 6° to the z axis in the earlier experiments discussed. In those experiments, a hot radiating axial cylinder (as would be observed from a radially converging shock) is observed as a line source because of the finite viewing angle, instead of a point source as observed here.

This radiation had been tentatively identified as that arising from a radiation driven shock beginning to stagnate on axis, which resulted from radiation produced when the outer array collided with the inner. The new measurements illustrate this effect well. The early enhancement on axis now has been measured not only on the top, but also from the bottom of the hohlraum. Its peak axial emission at 4 ns prior to stagnation is in excellent agreement with the E-RMHD expectation. In principle, radiation generated by this type of collision, external to the target, might be used to shape the radiation pulse driving an ICF capsule, and ideally the radiation and shock should be accounted for in ICF-capsule experiment design.

5.11. Array Fixturing Clue

5.11.1. Array Types

While much of this research was going on, two new methods for fixturing the arrays had been developed [128]. The redesigns were motivated by the need to simplify array construction and to remove the superstructure above the array fixture, which often interferes with lines of sight placed adjacent the top REH and used to view experiments. In the design of the original Saturn and now Z high wire-number experiments a great deal of care had been taken to insure excellent current contact between the wires and electrodes.

As previously mentioned, the contact issue arises because the distance between the anode and cathode electrode, between which the fine wires of the array are stretched, changes during vacuum pump down of the accelerator. If the thin wires were to be rigidly attached to both electrodes, they would break. This change requires the wires to slide within the wire fixture itself, while still making electrical contact.

Like the previous high wire-number loads, the Z arrays are assembled by draping each wire over a fixture through slots. In Z, a small copper weight (900 mg) is attached to to each end of the wire, forming two wires in the fixture 180° apart. The weights apply the tension. In contrast to Saturn experiments, because of differences in the geometry of the power flow to the load, once the wires have been assembled, the entire fixture is flopped over, such that the weights now reside above the anode (Fig. 26A). As in Saturn, the tension presses the wires firmly to both electrodes adjacent the inner electrode surfaces the plasma shell implodes on. This arrangement is referred to as the *flop-over* design, and has been in used in all my research on Z.

In the second arrangement, first used by Mike Cuneo in his ICF experiments, the individual wires are simply wrapped around small posts embedded in the anode with the wires left to hang down down through the cathode structure (Fig. 26B). Here, in contrast to the *flop over*, a solid current contact with the cathode is made substantially below the cathode surface, at the transition between the radial and axial feed to the load. Again the wires are tensioned by weights, and this arrangement is referred to as the *hang down* array.

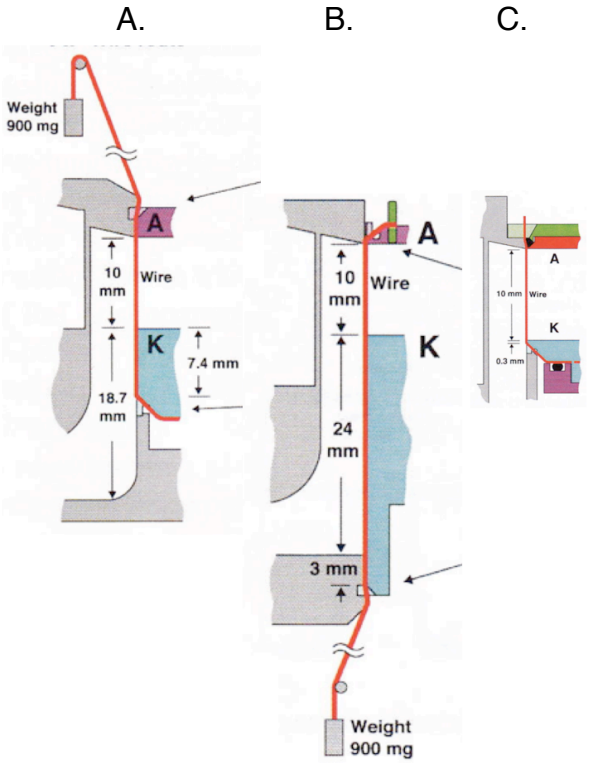

Fig. 26 (A) Flop-Over fixture, (B) Hang-Down fixture, and (C) Weightless fixture.

The third configuration is constructed similarly to the *flop-over*, except O-rings are used to hold the wires in position against the given electrode (Fig. 26C). Ideally, the pressure between the O-ring and electrode is such that the wires slide when the AK gap increases. Once constructed, the wires are cut below the anode, the tensioning weights

and associated structure removed, and then the array is inverted. Accordingly, it is referred to as the *weightless* array.

The major advantage of the *hang-down* and *weightless* over the *flop-over* is the absence of significant superstructure above the anode. An additional advantage of the weightless over the other two is its portability from its construction site to its installation on the accelerator. However, often the O-ring pressure is such that not all wires are held tightly enough against the electrode surfaces, resulting in slack wires and poor electrical contact once the weights are removed and the wire tension relaxed. The disadvantage of the *hang-down* relative to the *flop-over* and *weightless*, however, is its ill-defined wire-cathode current contact.

5.11.2. Big Power Differences

To date, minimal attention had been payed to the fixturing of the wires in high wire-number configurations between the anode and cathode structures. Because the voltage across the wire array is large, rapidly rising to MV levels, the general view had been that the quality of the electrical connection is of little importance. *Measurements with these three loads was to prove this attitude very wrong.* The measurements were all made using the standard nested wire configuration with the baseline or pedestal hohlraum target. The data now discussed was generally taken in a tag-along-mode, where the radiation from the top REH was used for radiation flow experiments by Los Alamos, although a few shots were taken in dedicated experiments where measurements of the axial power was measured from both a bottom and top REH were made. The primary diagnostics that were available, then measured only the radial and bottom axial powers. *No one thought that we would see any difference between the loads as they were all so similar*, except for the current contacts, but like the up-down symmetry, it was worth checking.

On average, the *flop-over* generates 153± 21(±7) TW of peak radial power and the hang-down 97±28 (±9) TW. (The uncertainty in the parentheses correspond to the statistical uncertainty of the mean.) The higher power of 1.6 of the *flop-over* relative to the *hang-down* correlates with the narrower pulse width and reduced shot-to-shot variation measured with the *flop-over*. With the *flop-over* the pulse width is 3.1±0.9 (±0.3) ns, whereas with the *hang-down* the width is 4.5±1.5 ns (±0.5) ns. The widths scale as the inverse ratio of the peak power as expected, giving credibility to the powers measured. In both fixtures, the azimuthal positioning of the wires is the same, and the method of current contact at the anode is similar. In both fixtures the horizontal forces holding the wires against the electrodes are similar. The major difference between the two is simply the wire-cathode contact point. In the *flop-over* the contact is close to the horizontal surface of the cathode

electrode; in the hang-down it is buried in the radial current feed some distance from the horizontal surface. The superior power generated with the *flop-over* thus largely reflects the difference in cathode current contact.

Because of the lack of superstructure, the *weightless* array was typically used when a clear field of view is required to access a radiation experiment placed above the top REH. Because of the benefit of the pedestal on the bottom, its marginal effect on the top, and the need to insure intimate contact between the pinch target and any top-mounted physics experiment, the *weightless* array has been fielded only with pedestals on the bottom.These comprised more than a dozen shots. Within this series of shots, four additional shots were taken with the usual top bottom diagnostics in place. Unlike the *flop-over* waveforms measured under similar conditions, there are significant differences among the *weightless* waveforms, especially 2 ns after stagnation. Moreover the power measured on the bottom was a factor of 1.5±0.2 lower with the weightless than with the *flop-over* array. The decreased axial power, and increased variation in power and pulse shape, correlate with increased wire-plasma material observed at the axial radiation holes of the DH.

These differences were also unexpected, since the wires are fixtured identically to that of the *flop-over*, with the exception that the positive tension on the wires, forcing the wires to the electrodes was removed prior to installation on the accelerator. The differences were traced to the quality of the current contacts, which often degraded during installation and prior to shooting. Single-wire data carried out by Peter Duselis [129] and Dan Sinars [130] in Prof. David Hammers group at Cornell supported the need for good wire-electrode contact (especially at the cathode) for efficient energy deposition to the wire during its initial heating phase.

5.11.3. Current Contact Important

In summary, these unexpected large differences, which related to the quality of wire-electrode current contact, especially at the cathode, began to shed light on a possible mechanisms for the origin of the pulse-shape differences and excesses tungsten measured often at the bottom REH. The thinking went as follows. Higher electric fields and arcing are more prevalent around those regions where poor contact is made, resulting in premature current shunting to the surrounding corona, which forms once current begins to flow through the wires. The ablation rate of the wire material is thus retarded, resulting in delay of the subsequent implosion from those affected regions. Mike Cuneo suggested that delays of 5-10 ns could be possible, and thus account for the multiple peak structure observed post stagnation. The arcing itself could lead to the early tungsten precursor observed to flow across the REHs. In the region of the

arcing, the wire ablation rate is likely increased.

These mechanisms may also be related to a *polarity dependent effect* reported first by Gennady Sarkisov for the explosion of single tungsten wires in coaxial geometry [131]. Namely, the higher radial electric field near the cathode relative to the anode (in the radial feed) causes the corona to breakdown earlier at the cathode than at the anode. The breakdown shunts the current to the relatively higher conductivity corona and results in a slower ablation rate of the wire material in this region (Fig. 27). The randomness of this process among the wires azimuthally, like that just described with poor wire-electrode contact, likely then degrades the quality of the implosion near the cathode relative to the anode region. In the case of slack wires, the effect appears independent of polarity, as multiple pulses are seen at both the anode as well as the cathode end of the hohlraum. The fact that multiple pulses are seen at the bottom with the weightless configuration, even with pedestals, suggests also that the effect of poor contact on wire ablation rate extends beyond the 3-mm length of the pedestals.

5.11.4. Polarity Effect?

A complementary clue came from the experiment I did next, to study whether or not the nested wire array is operating in a *hydrodynamic* or *transparent-like* mode, when the outer array arrives at the radius of the inner array [132].

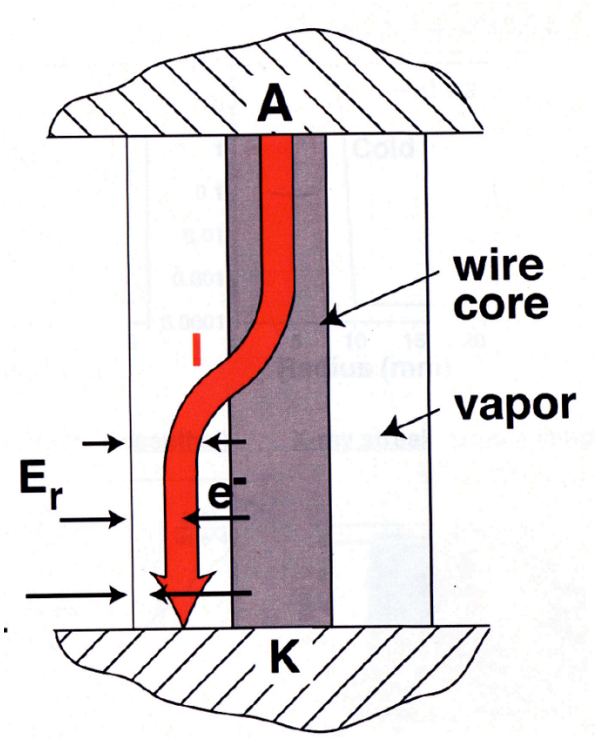

Fig. 27 Illustration of current shunting from wire core to surrounding vapor when localized ionization occurs. Er is the radial electric field at the surface of the wire.

In this experiment the diameter of the individual 240 wires in the outer array of the baseline driver was simply reduced from 7.5 μm to 5.2 μm and the diameter of the 120 wires in the inner array was increased from from 7.5 μm to 10.5 μm. In the modified outer array, the radial electric fields increased by a factor of ~1.4, resulting in greater ionization near the cathode, shunting the current earlier, and increasing the measured disparity between the quality of the coherence of

the array azimuthally between top and bottom earlier in the implosion.

With this driver, the top-bottom asymmetry, nearly eliminated eliminated by the pedestals in the baseline driver, returned big time, even when the pedestal target was used. The asymmetry was accompanied by significant M-shell tungsten measured at the bottom relative to the top REH, as observed when large asymmetries are measured for the baseline driver. This measured degradation, when only the diameter of the individual wires in the array is modified, further supports the idea that the *polarity effect* in the individual wires of the array itself may be at the root of the up-down asymmetry.

The *polarity effect* [131] was brought to my attention earlier when I met Gennady Sarkeisov, at the high-temperature diagnostics conference held in San Diego. At that chance meeting, in front of his poster, I thought that here, for the first time, was a real measured anode-to-cathode difference relating to wire expansion that surely must have an effect on the implosion process, and possibly our measured up-down asymmetry. Importantly, it seemed to fit the many clues we were turning up. Over the next few years we worked closely together with Steve Rosenthal to put meat on his observation.

5.12. Surprise

In the fall of 2003, I received an unexpected call from the American representative to the EPS (European Physical Society) program committee for the division of plasma physics asking if I would be willing to give an invited talk at the next meeting in London, UK on my research. I was deeply honored, and said certainly, submitting the title:

Progress in z-pinch driven dynamic-hohlraums for high temperature radiation-flow and ICF experiments at Sandia National Laboratories

and a short abstract of what I would talk about, as requested. Some months later I received notification that the talk was accepted. In June 2004, I delivered the lecture, which was published in a special issue of invited papers from the *31st EPS Conference on Plasma Physics and Controlled Fusion* [133].

The previous year Tom Mehlhorn of Sandia, reviewed the associated capsule dynamics in DHs and its scaling to high yields, together with other ICF approaches [134]. My paper complemented his presentation by reviewing the progress made in understanding the underlying physics of the DH and the characteristics of the resulting radiation produced. There I pointed out that he DH configuration is made up of four sequential subsystems. The first being the Z current-generator,

followed by the wire arrays, the target, and lastly the axial radiation and its utility in driving other subsystems such as a capsule or the SWH. I followed this progression in the lecture, tracking the transition from electrical to radiation power, and reviewed progress made.

Here I would like to mention a few of the items discussed there that so far I have skipped, to give a better sense of the Z driver itself, its connection to the DH, and the axial radiation generated. The Marx banks in Z are charged on the timescale of 90 s and then discharged into intermediate storage capacitors in 1 μs. These comprise the first of several stages of pulse compression. The energy conversion within the DH represents the last phase in power compression. The Z driver and its load may be represented as a high voltage source source (5.4 MV) feeding the DH in series with a low inductance (12 nH) and small resistance (0.12 ohms). The L/R rise-time of the current pulse at the DH is thus ~100 ns.

This simple model had been the bases of the input to most of our simulations, resulting in remarkable agreement with the current wave forms measured at the load. The magnetic field generated eventually results in the radial implosion of the shell. As this cylindrical load begins to converge towards the z-axis, its inductance increases, which eventually halts the rise in current, and leads to a peak current of 21.3 ±0.3 MA for the baseline DH (Fig. 25B), in agreement with the modeling. By ~6 ns prior to stagnation, the collision of the *plasma-shell* with the foam target is well under way. At 5 ns the W/CH interface is at ~2 mm and the foam has been heated to ~170 eV. For a 4-mm diameter REH, the peak axial power occurs later at 3±0.4 ns prior to stagnation. At this time, the radiation field emitted from the hohlraum can be described by a ~225-eV Planckian distribution in combination with a hard x-ray component, for x-rays greater than ~2 keV. The hard component constitutes ~6% of the total ~15 TW power at peak emission.

Despite the uncertainties in the dynamics I discussed, such as the mystery of the up-down asymmetry [123], the radiation generated internal and external to a DH has been successfully used to implode ICF capsules [135-137] as well as to heat external hohlraums, such as the SWH, to temperatures useful for ICF [112]. At the meeting, I showed the beautiful neutron signals Carlos Ruiz measured from his two nearly orthogonal scintillation detectors, which provided strong evidence for thermonuclear DD neutron production from deuterium-filled plastic capsules centered within a DH [137]. On average the neutron energy inferred from the two detectors agrees with the expected 2.45 MeV, and together with other diagnostics and null experiments [136] lead by Jim Bailey ruled out the possibility that the neutrons measured are produced by particle beams within the z-pinch itself. The average yield, from the 2-mm diameter

capsules [135] designed by Steve Slutz, filled with 12-14 atm of D2, is 3.3±1.1 x 10^{10} neutrons. At that time, this yield held the record for any indirectly driven implosion using a D_2-filled capsule. *A most impressive achievement indeed!*

In conclusion I showed that all the data taken of the internal radiation temperature of the SWH and DH, as a function of the external power used to heat the hohlraums, follow the expected Planckian relation between temperature, power, and hohlraum area over our measured useful range 60 to 170 eV, assuming hohlraum-wall albedos between 0.7 and 0.75. These albedos fall within the same range inferred from measurements of laser-driven hohlraums at 200 eV. The data indicate that the DH is about three times as efficient in producing a radiation-power environment than the SWH, as might be expected.

Assuming I^2 scaling with current, a 70-MA generator would be sufficient for reaching ignition temperatures (300 eV), scaling from the present Z results. With the optimistic assumption that the internal power within the DH could be increased by a factor of two on Z, a 50-MA generator would suffice. These estimates were made together with Rick Olson, who has been my insightful teacher on ICF issues, ever since we closely collaborated on the SWH research. I closed my talk showing Craig Olson's concept of a possible IFE (Inertial Fusion Energy) power plant based on the success of the DH as an ICF-target concept [138].

5.13. Second Surprise

Later that year, on December First, I received an email from Dr. Jo Lister, the Chairman of the Plasma Physics Division of the EPS stating that the Board has decided this year to award

The Hannes Alfven Prize of the European Physical Society' to: Prof. Malcolm G. Haines, Director of London's Imperial College Plasma Physics Dept., Dr. Thomas W.L. Sanford of Sandia Laboratories, USA , and Prof. Valentin P. Smirnov of the Kurchatov RRC, Moscow

and that would we all accept this prize for our combined work. In time we all received this email and accepted. Malcolm was at Sandia at the time, and I had the pleasure of informing him of the Boards decision. I also suggested that he should be the one to give the Alfven Lecture (as many of his friends would be in the audience) and write the draft paper, which was to be submitted to next years conference where we all were expected to attend. He was pleased to accept, and Valentin concurred.

This announcement had came out of the blue and brought tears to my eyes when I finally carefully read the letter. During my first reading, I thought that this was a solicitation for a recommendation to some award or other. I did not realize

that it was for me to accept or not. I was greatly humbled to be considered for this award along side Malcolm and Valentine, who were well recognized pioneers in plasma physics and pulsed power.

We all arrived in Barcelona, Spain the following June 2005 where Malcolm gave the Alfven Prize Lecture [139], which was well received. Following the lectures that continued that morning there was ceremony where we each received a certificate with our name that read:

"for his major contributions to the development of the multi-wire array in Z-pinch pulsed power physics; the X-ray yield was rapidly increased to the level of 2 Megajoules starting with pioneering work on the "Angara" facilities in Russia, through the "Saturn" project in the Sandia Laboratories to the present "Z" device also in Sandia, strongly supported by the rapid evolution of the underlying theory of cylindrical wire-array liner compression"

Our paper [139] titled *Wire-array z-pinch: a powerful x-ray source for ICF* was published in *Plasma Phys. Control. Fusion* December 2005 together with a picture of the three of us receiving the award (Fig. 28). This recognition meant a great deal to all of us, and the ceremony was truly a moving experience.

5.14. *Hydrodymnamic* or *Transparent-Like* Mode

5.14.1. Simulations Suggest O/I Collision Issues

Back to reality. Early E-RMHD simulations by Darrell Peterson in the r-z plane indicated that the addition of the inner array at half the radius and with half the mass of the outer could increase the axial x-ray power by as much as a factor of 2-3 relative to that produced by the implosion of a single outer array, depending on the size of the random density seed used. In the simulations, the increase arose from the suppression of the RT instability, which develops in the r-z plane when the outer array collides with

Fig. 28 Prof. Malcolm Haines, Dr. Thomas Sanford, and Prof. Valentin Smirnov after Malcolm's presentation of the Alfven Prize Lecture in Barcelona, Spain, where we each received the prize June 2005.

the inner. Implicit in these simulations is the assumption that both the outer (O) and inner (I) arrays have formed an azimuthally symmetric plasma shell by the time of impact. At the O/I impact

position the two arrays are assumed to merge and implode together as a single unit. In this *hydrodynamic* mode, radiation is generated at both the O/I collision and when the merged arrays impact the target (T).

Our earlier target measurements show, however, that the axial power increased by only (23±15)% with the addition of the inner array [121]. Matching the simulations with the experiment required reducing the seed significantly with respect to that which simulated the targetless experiments. The large discrepancy implied that the nested-array driver for the DH may not be operating in this purely *hydrodynamic* mode, as assumed in the simulations.

Previously, a *transparent-array* (or current-transfer) mode was proposed for nested implosions by Robert Terry and Jack Davis at NRL [140]. This mode assumes the inner wire remain discrete and the outer array (either as discrete wires or as a shell following the outer-wire ablation and wire merger) passes through the inner with little interaction other than rapid current switching to the inner. The switch results partly from the lower inductance path now being supplied by the former inner array.

Although this mode had been observed for low numbers of wires (large inter-wire gaps) at low current, no direct evidence for this mode with tungsten wire-arrays having high numbers of wires at high current, has been indicated until recently. Specifically, Mike Cuneo's experiments [141], with arrays half the diameter of those used for our DH, have shown *transparent* characteristics at the O/I collision. Determining which mode may be operating for the DH driver is of prime importance for understanding how the radiation is generated within the hohlraum itself and how to design configurations to maximize both the internal radiation for ICF applications and the axial radiation for the high-temperature radiation flow studies.

5.14.2 The Experiment

Accordingly, I set up an experiment [132] to definitively determine which mode the DH driver was operating in, with the support of John Porter who was now in charge of the ICF program. This time my team consisted in a number of my experimental Sandia colleagues, including Dave Bliss, Mike Cuneo, Tom Nash, Bill Stygar as well as my theoretical colleagues Jerry Chittenden, Malcolm Haines, Darrell Peterson, and Eduardo Waisman. The idea was to determine the mode by measuring the characteristic features of the radial and axial radiation pulses measured.

Features arise on these x-ray pulses when the outer array reaches the radius of the inner, when either the outer (*transparent*), or the combination of the outer and inner arrays (*hydrodynamic*) impact the foam target, and with the final stagnation of the z-pinch mass on axis. The calculated difference in timing between the x-ray bursts from the outer

array interaction with the inner array and when the outer array mass impacts the target (O/I-O/T) in the *transparent* mode, however, differs minimally (2-3 ns) from that if the collision is assumed to be *hydrodynamic*. In order to enhance timing differences, as calculated by either mode using a thin-shell array model developed by Mike Cuneo and Eduardo Waisman [141,142], measurements were made with both the baseline configuration and when the masses of the outer and inner wire arrays were reversed.

For the reversed-mass driver, all parameters such as wire number, array radii, and target remained the same; the diameters of the individual wires were adjusted to reverse the array masses. In this configuration, if the mode was *transparent*, we expected to see a radiation signal when the outer array passed through the inner array. In addition, we expected a radiation signal when the now former outer array impacted the target prior to the impact of the former inner array with the target once current had switched to the former inner array. In this case, the timing difference between the outer and inner arrays impact on the target of 14 ns is easily observable.

5.14.3. The Results

Two-dimensional resistive MHD simulations [143] in the r-θ plane by Jerry Chittenden show the collision in either configuration to be similar, and *transparent* in nature. Specifically the simulations show the outer array forms a *plasma shell* prior to the O/I collision, where as the wires of the inner array expand only slightly remaining relatively discrete at the time of the collision. *This similarity thus implies that, if a transparent mode is operating in the easily mode-identifiable reverse-mass configuration, it is also likely to be operating in the baseline configuration.* The similarity is expected because the ratio of the initial inter-wire gap to wire diameter is 70 for both arrays in the baseline and only changes to 100 and 50 for the outer and inner arrays for the reverse-mass configuration, respectively.

The experimental arrangement is similar to that discussed previously, which used the pedestal target and of course the *flop-over* array. We had a new addition of a time-resolved transmission-grating pin-diode system supplied by Bill Stygar, which was particularly sensitive to the radiation generated when the outer array collided with the inner, when viewing the outer radial position of the inner array. This radiation provided a well defined time of the O/I collision relative to stagnation.

With the reverse-mass driver, the radial radiation data clearly show the features expected from the thin-shell model only in the *transparent* mode. Moreover, the complicated shape of the measured radiation profile, which span a dynamic range of ~1000, qualitatively agrees with the MHD simulations. Although, the features of the O/T and I/T

collisions, and their timing differences, are difficult to perceive in the radiation profiles measured with the baseline geometry, they were picked out. Again they too agree with that expected assuming *transparency*. And again, in support of *transparency*, the onset of the axial radiation in the reversed-mass configuration is only consistent with *transparency* [132].

The effects of the expected current switching when the outer array passes the inner one are also observable in the discontinuities in the average radial position of the current extracted from the measured load inductance from our current monitors. The analyses shows the average radius of the current to be near the measured rear surface of the outer *plasma shell* (at the leading edge of the RT bubbles) prior to the impact with the inner array. The wave length of these bubbles leading up to the O/I collision is in excellent agreement with Darrell's r-z E-RMHD simulations.

Remarkably, despite the assumption of a *hydrodynamic* collision in the simulations, the more than doubling of the simulated wave length after the collision and at the target is also in agreement with that measured. All of which further supports the 3D nature of the implosion. *Importantly, the transparency of the O/I collision now offers a rational explanation for the limited increase in x-ray power when the inner array is added to from the nested geometry.* The predicted sizable increase in power was based on the assumption that both the outer and inner arrays were assumed to form azimuthally uniform *plasma shells* prior to the O/I collision, and that the collision was *hydrodynamic*, significantly suppressing the RT instability.

5.15. Up-Down Mystery Solved

5.15.1. My Last Experiment

The last experiment I did on Z, aside from being developed to understand the axial asymmetry, was designed to determine if our coupled system of baseline nested-array driver with pedestal target produces close to the maximal radiation power [144]. One variation changed the outer-array diameter from 24 to 56 mm in five discrete steps by keeping the implosion time constant (by keeping the product of the load mass times the square of the load diameter fixed). Over this variation, the relative Er (radial electric) increased from 0.33 to 1.75. The relative Er is defined to be the radial electric field (Fig. 27) at the axial midpoint of the outer wire normalized by the field calculated for the baseline driver, and is used as a dimensionless experimental parameter for correlating with the strength and timing of the axial asymmetry found in the x-ray emission.

In the procedure, the inner array was like that of the baseline-driver, namely: kept at half the diameter of the

outer, the inner wire number kept at half the outer, and the mass of the inner kept at half the outer. The mass of the central foam target was kept equal to the sum of the outer and inner arrays. These constraints were shown earlier by Tom Nash to approximately maximize the radiated x-ray power for the baseline driver. Additionally, because the power has been shown to depend on the wire number [102], for each diameter, the wire number changes were kept within about ±15% of the mean number or wires used.

At each step, the shot was repeated. Measurements of both the axial and radiated power tracked one-another and showed the baseline 40-mm diameter outer array still maximized both powers, with nothing to be gained by any of the changes. As the array diameter increased beyond 32 mm, however, the top-bottom asymmetry developed, systematically increasing along with increase in the associated M-shell tungsten measured in the REHs, principally on the bottom.

The other variation explored changed the outer-array wire number from 108 to 540 in five discrete steps while keeping the outer array mass the same at 2 mg/cm. Over this variation, the relative Er decreased from 1.49 to 0.67. Again the inner array was kept at half the diameter of the outer, the inner wire number kept at half the outer, and the inner mass kept at half the outer. The mass of the target was kept equal to that of the sum of the inner and outer arrays. All variations were repeated.

Again measurements of both axial and radiated power tracked one-another and showed that the baseline geometry of 250 wires in the outer array and 120 in the inner still maximized both powers, with little to be gained by any of the changes. As the outer-array wire number decreased from 540 wires, which showed no up-down asymmetry, however, the asymmetry systematically increased as the number of wires decreased. Again the M-shell tungsten tracked the increase, especially as measured on the bottom REH.

5.15.2. The Independent Variable Er

The origin of the early tungsten has been a mystery until now. With the large widely varying asymmetry mitigated by the pedestals, however, we have been able to observe here the radiation symmetry more consistently as a function of one of the independent variables of the experiment, namely the radial electric field Er at the surface of the outer wires of the outer array. The association of the asymmetry with Er was motivated earlier by the possible connection of the *polarity effect* in single wires [131] with the observation that the asymmetry greatly increases, when the masses of the outer and inner wires are reversed relative to the baseline driver [132]. In this experiment, the only change was to reduce the diameter of the outer wires from 7.4 to 5.4 μm and increase the inner

from 7.4 to 11 μm. With this change, Er increases by a factor of 1.4 relative to the baseline driver. Related effects are now seen in these experiments, namely the larger the array diameter, the larger is the Er, and the larger the asymmetry. And the smaller the wire number, the larger is Er, and the larger is the asymmetry.

When all of the two-pedestal data are plotted as a function of Er, the Er appears to be a unifying predictor of the asymmetry, with higher Er resulting in larger range of asymmetry. Above a relative Er of ~0.8, the axial powers, times of peak power, rise times, and tungsten M-shell fraction differences between top and bottom begin to significantly diverge. The phenomenon may be understood as follows. Er affects the current distribution at very early times when it can enhance the electron emission from the wire cores and generate early breakdown of the vapor surrounding each wire. The current then locally shunts to this surrounding plasma of lower resistance rather than remaining in the wire core (Fig. 27). In this way, as found in single-wire experiments [131], the wire cores remain cold near the cathode (where Er is highest) and are not as hot as near the anode. Therefore, for a given wire arrangement, the larger Er (which is always near zero at the anode end of the pinch) becomes, the greater is the energy imbalance between the top and bottom. *The data thus suggest that the axial radiation asymmetry scales with the axial energy deposition variation within wires of the outer array.*

5.15.3. Implosion Zippering

This observation turns out to fit with another important observation made using an x-ray streak camera developed by Greg Rochau. Images of the target along the z-axis as a function of time exhibit zippering of the main plasma shell at stagnation for the baseline load, with the earliest arrival of plasma at the anode followed by systematically latter arriving plasma the closer the plasma came to the cathode. We observed this also in the delay of the peak axial power on the bottom with respect to the top (Section 5.9.2).

This effect was first modeled by Steve Rosenthal, by evaluating the energy deposited in the wire, using our measured pre-pulse current at the load. In the model, when current flows in the wire it Joule heats and expands. The change reduces its conductivity, producing an increasing resistive voltage drop along the wire, and results in the development of a low-density, very low-conductivity metallic vapor layer at the wire surface. With no Er at the wire surface, which is the case near the anode, the voltage collapses when the outer metallic vapor layer Joule heats to ionization, producing a rapidly expanding hot metallic plasma [131]. *This occurs ~180 ns prior to stagnation and ~80 ns prior to the rapid onset of the main 20-MA driving current.* At the cathode, on the

other hand, the breakdown occurs when Er reaches the field emission threshold of ~300 kV/cm. This breakdown occurs ~3 ns prior to the breakdown at the anode and thus results in a colder core with a temperature difference of ~0.7 eV between the two ends of the wire.

5.15.4. The Long Wait

Incorporating the above, Chris Jennings modified (in the full base-line configuration including wires) the initial temperature of the pre-expanded gaseous wire cores in the MHD code GORDON [143] to reflect the estimated anode-cathode temperature difference. A 3D wedge geometry modeled a single wire in the array. In one simulation, referred to as the cold one, an initial core temperature corresponding to that at the cathode was used, and in the other, referred to as the hot one, an initial core temperature corresponding to that at the anode was used.

The array with the lower temperature persists as a cold core ablating tungsten for a prolonged period of time before running out of material and beginning to implode. As the implosion proceeds, precursor tungsten contained within the array is snowplowed up, essentially tamping the acceleration of the imploding surface. This situation exemplifies what may occur near the cathode because of early current shunting. The precursor plasma partly represents what we see early in time on the cathode side being blocked, in part, by the bottom pedestal.

For the high initial temperature, which represents what may occur near the anode with little or no current shunting, the wire ablation proceeds more rapidly. The higher mass ablation rate results in a lower velocity of the ablated tungsten and formation of little precursor tungsten, as seen experimentally. The core-corona structure does not persist for a prolonged period, and the implosion is more shell like. With earlier complete wire ablation, less tungsten is present within the array to be snowplowed up and the array implodes more quickly, allowing the shell to reach the axis prior to the corresponding cold-core implosion.

These two simulations represent extremes of conditions at either end of the wires. Between the ends, current shunting will gradually occur later as the anode is approached, resulting in the zippered stagnation as seen experimentally. The simulated time difference of the zipper between anode and cathode of 4.0±0.5 ns is in agreement with the 4.3±1.0 ns measured for the four shots having the streak camera in place. Moreover, the simulations correspond to other features measured in the images prior to stagnation, such as when the early plasma collides with the inner array and lower pedestal. Simulation of arcing at the cathode-electrode contact, for example, predicts the formation of an RT

bubble that impacts the bottom pedestal 10±1 ns prior to the main shell's impact, in agreement with the 14±2 ns measured.

I remember waiting along with Malcolm Haines, Chris's thesis advisor, with great anticipation for Chris's simulation results to complete, for these very long 3D calculations. Would the resulting shell reach the anode first or would it be the other way around and we would then have to throw out our explanation? Wonderfully, the shell reached the anode first and then the cathode, and incredibly Chris's simulation confirmed our model beyond any doubt.

This time, with our explanation in place, my submission to PRL with the title *Wire Initiation Critical for Radiation Symmetry in Z-Pinch-Driven Dynamic Hohlraums* was now accepted, and published February 2007 [144]. This was four years after we first measured the up-down asymmetry. *The explanation had been hard for the z-pinch community to initially accept, because the mechanism was occurring ~80 ns prior to the start of the rise of the 20-MA current pulse, when the current was less than 50 A/wire. How could this small current have any important effect relative to sudden rise of MAs of current?*

What a thrill we all had putting together the clues accumulated over years to at last solve the asymmetry mystery, and show, moreover, how the asymmetry could be mitigated. It required a team effort at every stage, bringing together both experimentalist and theorists.

5.15.5. Explanation for Lost Bet to Keith

This experiment also cleared up another mystery of why I lost my bet with Keith Matzen (please see Section 5.6). The doubling in axial and radial x-ray power when the wire number increased from 100 to 250 wires (and decreased inter-wire spacing to 0.5 μm) is related to the transition from the implosion of individual *wire plasmas* to that of a *plasma shell* where the wire coronas have merged, and to the increased azimuthal symmetry of the merging coronas. *The slow decrease in measured power for wire number greater than 250, however was not anticipated, as our earlier experiments had always shown that more wires generated more power* [102]. By 540 wires both the axial as well as the radial powers had decreased by two. It was in this high wire number region (500 to 726) that I had conduced our higher mass experiment [115]. Rather than increasing wire size to increase the array mass, I chose more wires, thinking that more wires had always improved the symmetry and resulting radiation power.

The transition from increasing power to a decrease in radiated power with wire number increase has been carefully measured by Sandia's Mike Mazarakis and his team on Z before its refurbishment [145]. They found that when wire number in his 20-mm diameter

tungsten experiments exceeds ~350 wires and the associated inter-wire gap decreases below ~0.2 μm, the radiation diminishes. These observations are close to what we experienced here for wires above 250 and perhaps unintentionally in our earlier mass scan [121].

For Mikes's experiment, the thinking by Serge Lebedev, of Imperial College, was that the plasma distribution inside the wire array, prior to the onset of core merger, enhances the pinch stability [146]. When the wire number becomes larger than the optimum number ~350, the wire cores start merging very early during the pre-pulse stage of the current pulse, the precursor plasma inside the array becomes negligible, and the wire array implodes as a thin shell, which then is prone to the RT instability earlier.

5.16. Dynamic Hohlraum Mini-Summary

Wisdom on all that we had learned exploring the compression of DHs was summarized in the invited lecture titled *Overview of the Dynamic Hohlraum X-Ray Source at Sandia National Laboratories* I gave at the *International Megagauss Magnetic Fields: Production and Application* conference held in Santa Fe, NM, November 2006, and published in *IEEE Trans. Plasma Sci.* February 2008 [115]. This review underscored the need to include wire initiation in the simulations if a predictive capability is to be achieved in wire-array z-pinch physics. In particular, the mysteries, behind why increasing the mass of the outer array diminished the radiation power, why the addition of the inner array only marginally increased the radiation, why reducing the target length below 7.5 mm killed the axial radiation, and why a significant difference exists between the axial radiation exiting the top REH relative to that exiting the bottom REH, are all related to the discrete nature of the wires. And in the last case, the mystery is related to the magnitude of the radial electric-field on the surface of the outer array of wires before the plasma shell forms. These observations are all in contrast to the predictions of the RMHD simulations.

We had solved the up-down mystery. Money had been found to refurbish the 50-TW Z, increasing its power to 80 TW. Refurbishing this ten year old work horse would take time, perhaps a year or more. It was the right time to retire, and I did. I was now 65 years old.

6. CONCLUSION

The history of the HERMES III diode told here is an example of the evolution of physics from *theory-to-observation-to-refinement*. The initial research conducted on HELIA was first motivated by theoretical modeling, then followed by experiment and interpretation, followed again by experiment on HERMES III, and so on, which led to unforeseen useful possibilities. These included the efficient propagation of the 19-MeV electron beam in the *collisional* regime 11 m to an outdoor test cell, and to the discovery of a second propagation mode in the *ion-focused* regime, which provided unique radiation testing opportunities for the nuclear radiation-effects community.

At the other extreme, the later development of the DH for ICF, beginning with the initial breakthrough in wire-array stabilization, demonstrated the evolution of physics understanding from the *observation-to-theory-to-refinement* modality. My experimental observation that x-ray power from a z-pinch increased by almost an order of magnitude with an associated increase in the number of wires employed, made plain the utility of z pinches, and opened the door to z-pinch ICF, once the process was better understood.

The successes of these research programs and developments were made possible by experimentalists and theorists who formed coherent teams that were challenged to understand the underlying physics and the joy of finding solutions to new issues our experiments raised. I learned early in the high-energy experiments that I participated in, the power of bringing in strong theoretical collaborators to motivate a given experiment (as in the case of HERMES III) or to help interpret a given observation (as in the case of the z-pinch breakthrough).

Importantly, I showed here by detailed example, that redundancy and multiple approaches to a given measurement provides confidence in the measurement itself, and is fundamental to a successful experiment. As a result *every* experiment initiated resulted in a published paper, including the *compact* wire-array experiment, which gave the unexpected low yield of warm x-rays.

As a philosophical point, my physics career illustrates the need to *adapt* to changing outside conditions. This occurred when suitable academic positions became scarce in the 1970s. Sandia offered the possibility of still doing cutting edge science, but now in areas of direct utility to the nation. And within Sandia itself there again was a need to *adapt* from HERMES III diode research to that of z-pinch research. Unexpectedly, this research led to its application in ICF, which is where I had wanted to ultimately be when first considering Sandia as a place of employment. The path to making meaningful contributions to science is thus truly winding, but with vision (and

picking the right problems to work on), my career illustrates it does happen. The key is optimism, fortitude, and the ability to *adapt.*

In conclusion, it has been both a tremendous privilege to be able to lead the efforts I have been responsible for, and an honor to work with all the wonderful individuals who have made the research possible. The research helped me grow as a scientist, first in helping to explore the frontier of intense electron beams through the use of pulsed-power technology, and later to participate in aspects of z-pinch and associated ICF developments. This research, of importance to the nation through DOE, was made possible within the frame work of Sandia, which supplied first the need and then the necessary resources to solve its problems. Crucially, the success of the work was due, in large part, to the dedicated Sandia management and technical staff who were intimately wrapped up in facilitating the R&D.

REFERENCES

1. J. J. Ramirez, K. R. Prestwich, et al (including T. W. L. Sanford), **HERMES III – A 16-TW, Short-Pulse, Gamma-Ray Simulator**, in *BEAMS '88, Proceedings of the 7th Inter. Conf. on High-Power Particle Beams* (Karlsruhe Germany, July 4-8, 1988) eds. W. Bauer and W. Schmidt, Kernforschungszentrum Karlsruhe GmbH, pp. 326-332. pp. 148-156.

2. R. B. Spielman, C. Deeney, et al (including T. W. L. Sanford), **Tungsten wire-array Z-pinch experiments at 200 TW and 2 MJ**, *Phys. Plasmas* **5**, 2105 (1998).

3. M. K. Matzen, C. Deeney, R. J. Leeper, J. L. Porter, R. B. Spielman, et al (including T. W. L. Sanford), **Fast z-pinches as dense plasma, intense x-ray sources for plasma physics and fusion applications**, Plasma Phys. Control. Fusion **41** (1999) A175-A184.

4. Anne Van Arsdall, **Pulse Power at Sandia National Laboratories the first forty years**, SAND2007-2984P, June 2007.

5. Neil Singer, **Wonders of Nuclear Fusion-Creating an Ultimate Energy Source,** University New Mexico Press, 2011.

6. T. Sanford, S. Childress, G. Dugan, L. M. Lederman, and L. E. Price, **Elastic Muon Carbon Scattering in a Low-Momentum-Transfer Region**, *Phys. Rev.* **C8**, 896 (1973).

7. R. D. Baker, et al (including T. W. L. Sanford and T. G. Walker), **The Reaction $\pi^- p \rightarrow K^\circ \Lambda^\circ$ up to 1334 MeV/c**, *Nucl. Phys.* **B141**, 29 (1978).

8. K. Guettler, B. G. Duff, et al (including T. Sanford), **Inclusive Production of Low-Momentum Charged Pions at $x = 0$ at the CERN Intersecting Storage Rings**, *Phys. Lett.* **64B**, 111 (1976).

9. J. J. Aubert, et al, (including T. Sanford and Samuel C. C. Ting), **Search for More *J* Particles**, *Phys. Rev. Lett.* **35**, 416 (1975).

10. D. Antreasyan, et al (including T. Sanford, and Samuel C. C. Ting) **Measurement of Dimuon Production at $s^{1/2} = 62$ GeV**, *Phys. Rev. Lett.* **45**, 863 (1980).

11. J. H. Christenson, J. H. Goldman, E. Hummel, S. D. Roth, T. W. L. Sanford, and J. Sculli, **Measurement of the Phase and Magnitude of η_{+-}**, *Phys. Rev. Lett.* **43**, 1212 (1979).

12. J. H. Christenson, J. H. Goldman, E. Hummel, S. D. Roth, T. W. L. Sanford, and J. Sculli, **Measurement of the Phase and Magnitude of η_{oo}**, *Phys. Rev. Lett.* **43**, 1209 (1979).

13. R. Bailey, D. G. Bardsley, et al (including T. W. L. Sanford),

Observation of $D^{*\pm}$ and $D^0/D^\pm$ Production in High-Energy π^-Be Interactions at the SPS, *Phys. Lett.* **132B**, 230 (1983).

14. R. Bailey, D. G. Bardsley, et al (including T. W. L. Sanford), **Production and Decay Properties of D and D* Mesons in π^-Be Interactions**, *Phys. Lett.* **132B**, 237 (1983).

15. T. W. L. Sanford, J. R. Lee, J. A. Halbleib, et al, **Electron Flow and Impedance of an 18-Blade Frustrum Diode**, *J. Appl. Phys.* **59**, 3868 (1986).

16. T. W. L. Sanford, P.D. Coleman, and J. W. Poukey, **Measurement and interpretation of electron angle at MABE beam stop**, *IEEE Trans. Nuc. Science,* Vol. NS-32, No 5, 3271, 1985.

17. B. Goplen et al,"**Users Manual Manual for MAGIC,"** Mission research Corporation Report No. MRC/WDC-R-068, Alexandra, Va, September 1983.

18. J. A. Halbleib and T. A. Mehlhorn, **"ITS: The Integrated TIGER Series of Coupled/Photon Monte Carlo Transport Codes,"** in Nucl Sci Eng 92 (1896) 338.

19. J. J. Ramirez, D. E. Hasti, J. P. Corley, et al, in the proceedings of the 5th IEEE Pulsed Power Conference, Arlington, VA 1985, edited by P. J. Turchi and M. F. Rose, IEEE Catalog No. 85C2121-2, 143.

20. T. W. L. Sanford, J. A. Halbleib, J. W. Poukey, et al, **Improved Bremsstrahlung Radiation Uniformity from an Indented-Anode Diode**, *Appl. Phys. Lett.* **50**, 809 (1987).

21. T. W. L. Sanford, J. W. Poukey, T. P. Wright, et al, **Impedance of an Annular-Cathode Indented-Anode Electron Diode Terminating a Coaxial Magnetically Insulated Transmission Line**, *J. Appl. Phys.* **63**, 681 (1988).

22. T. W. L. Sanford, J. A. Halbleib, J. W. Poukey, et al, **Improved Flash γ-Ray Uniformity Using a Bø-Lens Diode**, *Appl. Phys. Lett.* **54**, 1406 (1989).

23. J. M. Creeden, J Appl. Phys. **46**, 2946 (1975).

24. G. A. Mastin and T. W. L. Sanford, **Digital Image Processing Diagnostics for the HELIA and HERMES III Accelerators**, *Nucl. Instrum. Methods in Phys. Res.* **A286**, 9 (1990).

25. J. A. Halbleib, T. W. L. Sanford, and J. W. Poukey, **Radiation Environment of HERMES III**, *IEEE Trans. Nucl. Sci.* **35**, 1282 (December 1988).

26. HWH/JCM/82/8, "**Re-Evaluation of the Bremsstrahlung Production Efficiency for Optimum Targets,**" Internal Memo, Atomic Weapons

Research Establishment, England.

27. T. W. L. Sanford, J. A. Halbleib, and W. Beezhold, **Experimental Check of Bremsstrahlung Dosimetry Predictions for 0.75-MeV Electrons**, *IEEE Trans. Nucl. Sci.* **NS-32**, 4410 (1985).

28. T. W. L. Sanford, D. E. Beutler, J. A. Halbleib, and D. P. Knott, **Experimental Verification of Bremsstrahlung Production and Dosimetry Predictions for 15.5 MeV Electrons**, *IEEE Trans. Nucl. Sci.* **38**, 1160 (1991).

29. D. E. Beutler, J. A. Halbleib, T. W. L. Sanford, and D. P. Knott, **Experimental Verification of Bremsstrahlung Production and Dosimetry Predictions as a Function of Energy and Angle**, *IEEE Trans. Nucl. Sci.* **41**, 2727 (1994).

30. T. W. L. Sanford, J. A. Halbleib, D. E. Beutler, and D. P. Knott, **Bremsstrahlung Production and Dosimetry Predictions as a Function of Energy and Angle**, *IEEE Trans. Nucl. Sci.* **41**, 2727 (1994).

31. T. W. L. Sanford, J. A. Halbleib, J. W. Poukey, et al, **Measurement of Electron Energy Deposition Necessary to Form an Anode Plasma in Ta, Ti, and C for Coaxial Bremsstrahlung Diodes**, *J. Appl. Phys.* **66**, 10 (1989).

32. J. J. Ramirez, K. R. Prestwich, et al (including T. W. L. Sanford), **HERMES III – A 16-TW, Short-Pulse, Gamma-Ray Simulator**, in *BEAMS '88, Proceedings of the 7th Inter. Conf. on High-Power Particle Beams* (Karlsruhe Germany, July 4-8, 1988) eds. W. Bauer and W. Schmidt, Kernforschungszentrum Karlsruhe GmbH, pp. 326-332. pp. 148-156.

33. T. W. L. Sanford, J. A. Halbleib, J. W. Poukey, et al, **Dynamics of Electron Flow in Extended Planar-Anode Diode Operating at 19 MV and 700 kA**, *J. Appl. Phys.* **67**, 1700 (1990).

34. T. W. L. Sanford, J. A. Halbleib, J. W. Poukey, et al, **Radiation Field from an Extended Planar-Anode on HERMES III**, *IEEE Trans. Nucl. Sci.* **36**, 1931 (1989). 30.

35. T. W. L. Sanford, J. A. Halbleib, R. C. Mock, et al, **Characterization of Flash γ-Ray Detecters that Operate in the Trad/s Range**, *Nucl. Instrum. Methods in Phys. Res.* **A294**, 313 (1990).

36. G. A. Carlson, T. W. L. Sanford, and B. A. Davis, **A Solid Dielectric Compton Diode for Measuring Short Radiation Pulsewidths**, *Rev. Sci. Instrum.* **61**, 3447 (1990).

37. T. W. L. Sanford and J. A. Halbleib, **Radiation Output and Dose Predictions for Flash X-Ray Sources**, *IEEE Trans. Nucl. Sci.*, **NS-31** (6), 1095 (1984).

38. T. W. L. Sanford, J. A. Halbleib, and R. C. Mock, **Dose-Rate Field of the HERMES III Flash X-Ray Source**, *IEEE Trans. Nucl. Sci.* **37**, 1762 (1990).

39. T. W. L. Sanford, J. W. Poukey, R. C. Mock, and D. R. Welch, **Dynamics of a 700-kA, 19-MeV Electron Beam in a Short Gas Cell**, *J. Appl. Phys.* **71**, 472 (1992).

40. T. W. L. Sanford, J. A. Halbleib, J. W. Poukey, et al, **Very Intense Source of Flash X Rays**, *J. Appl. Phys.* **72**, 4934 (1992).

41. T. W. L. Sanford, J. A. Halbleib, D. E. Beutler, et al, **Production and Measurement of Flash X-Ray Dose Rates in Excess of 10^{13} rad (CaF_2)/S**, *IEEE Trans. Nucl. Sci.* **38**, 1195 (1991).

42. T. W. L. Sanford, L. J. Lorence, J. A. Halbleib, et al, **Photoneutron Production Using Bremsstrahlung from the 14-TW Pulsed-Power HERMES III Electron Accelerator**, *Nucl. Sci. Eng.*, **114**, 190 (1993).

43. "**MCNP- A General MONTE Carlo Code for Neutron and Photon Transport,"** LA-7396-M, Rev. 2, J. F. Briesmeister, Ed., Los Alamos National Laboratory (1986).

44. J. R. Lee, R. L. Coats, J. A. Halbleib (including T. W. L. Sanford) et al, **Design Feasibility of an Externally Driven Nuclear Assembly (EDNA),** Sand89-1578, May 1990.

45. T. W. L. Sanford, J. A. Halbleib, L. J. Lorence,et al, **Voltage Monitors for High-Power 10–20 MV Pulsed Electron Accelerators**, *Rev. Sci. Instrum.* **63**, 4795 (1992).

46. T. W. L. Sanford, J. W. Poukey, J. A. Halbleib, et al, **Voltage Dependence of Electron Dynamics in High-Power Extended Planar-Anode Diodes**, *J. Appl. Phys.*, **73**, 2004 (1993).

47. T. W. L. Sanford, J. A. Halbleib, W. H. McAtee, et al, **Improved Flash X-Ray Uniformity at 19 MeV Using a Compound-Lens Diode**, *J. Appl. Phys.* **69**, 7283 (1991).

48. T. W. L. Sanford and R. C. Mock, **An Intense Large-Volume Uniform Source of Bremsstrahlung for Pulsed Gamma Ray Simulation**, *IEEE Trans. Nucl. Sci.*, **39**, 2060 (1992).

49. B. B. Godfrey and W. R. Welch, **The IPROP Three-Dimensional Beam Propagation Code,** Twelfth Conf. Numerical Simulation of Plasmas, San Francisco. 1987, paperCM1.

50. T. W. L. Sanford, J. A. Halbleib, W. H. McAtee, et al, **Transport Dynamics of a 19-MeV, 700-kA Electron Beam in a 10.8-m Gas Cell**, *J. Appl. Phys.* **70**, 1778 (1991).

51. T. W. L. Sanford, J. W. Poukey, J. A. Halbleib, and R. C. Mock,

Compound-Lens Injector for a Pulsed 13-TW Electron Beam, *J. Appl. Phys.* **73**, 8607 (1993).

52. T. W. L. Sanford, D. R. Welch, and R. C. Mock, **Dynamics of a 19-MeV, 700-kA, 25-ns Electron Beam in a Long Collisional Gas Cell**, *Phys. Fluids B* **5**, 4144 (1993).

53. T. W. L. Sanford, D. R. Welch, and R. C. Mock, **Very High-Current Propagation in the Ion-Focused to Collision-Dominated Regime,** *Phys. Plasmas* **1**, 404 (1994).

54. T. W. L. Sanford, **High-Power Electron-Beam Transport in Long Gas Cells from 10^{-3} to 10^{3} Torr Nitrogen**, *Phys. Plasmas* **2**, 2539 (1995).

55. T. W. L. Sanford, **Dynamics of Electron Flows and Radiation Fields Produced by Electron-Beam Diodes on the HERMES III Accelerator**, *Phys. Fluids* **B3**, 2387 (1991).

56. J. J. Ramirez, K. R. Prestwich, et al (including T. W. L. Sanford), **Performance of the HERMES III Gamma Ray Simulator**, in *BEAMS '88, Proceedings of the 7th Inter. Conf. on High-Power Particle Beams* (Karlsruhe Germany, July 4-8, 1988) eds. W. Bauer and W. Schmidt, Kernforschungszentrum Karlsruhe GmbH, pp. 26-31.

57. T. W. L. Sanford, J. A. Halbleib, et al,**Test of Extended Planar-Anode Diode on HERMES III**, in *BEAMS '88, Proceedings of the 7th Inter. Conf. on High-Power Particle Beams* (Karlsruhe Germany, July 4-8, 1988) eds. W. Bauer and W. Schmidt, Kernforschungszentrum Karlsruhe GmbH, pp. 326-332.

58. T. W. L. Sanford, J. A. Halbleib, D. L. Johnson, et al, **Temporal Charactorization of the 19-MeV, 700-kA HERMES III Electron Beam**, in *BEAMS '90, Proceedings of the 8th Inter. Conf. on High-Power Particle Beams* (Novosibirsk USSR, July 2-5, 1990), eds. B. N. Breizman and B. A. Knyazev, (World Scientific Publishing Co., 1991) pp. 614-619.

59. T. W. L. Sanford, J. A. Halbleib, J. W. Poukey, D. R. Welch, R. C. Mock, P. J. Skogmo, and K. A. Mikkelson, **Generation, Control, and Transport of a 19-MeV, 700-kA Pulsed Electron Beam**, *BEAMS '92, Proceedings of the 9th Inter. Conf. on High-Power Particle Beams* (Washington DC, May 25-29, 1992), ed. D. Mosher and G. Cooperstein, NTIS PB92-206168, p. 119.

60. T. W. L. Sanford, J. W. Poukey, D. R. Welch, and R. C. Mock, **Intense Electron-Beam Transport in the Ion-Focused Regime Through the Collision-Dominated Regime**, *BEAMS '94, Proceedings of the 10th Inter. Conf. on High-Power Particle Beams*, 140 (San Diego, CA, June 20-24, 1994), eds W. Rix and R. White, NTIS

PB95-144317, pp. 140-143.

61. T. W. L. Sanford, J. A. Halbleib, G. Cooperstein, and B. V. Weber, **Potential Enchancement of Warm X-ray Dose from a Reflexing Bremsstrahling Diode**, *IEEE Trans. Nucl. Sci.* **42**, 1902 (1995).

62. D. Mosher, S. J. Stephanakis, et al, **Electrical Characteristics of High Energy-Density Exploding Wire Plasmas,**" *Annals of the New York Academy of Science* **251**, 632 (May 8, 1975).

63. T. W. L. Sanford, D. Humphreys, et al, **Preradiation Studies for Non-Thermal Z-Pinch Wire Load Experiments on Saturn,** *Sandia National Laboratories*, SAND94-0694, June 1994.

64. M. J. Clauser, L. Baker,, D. H. McDaniel, R. W. Stinnett, and A. J. Toepfer, "**Magnetic Implosions of Plasmas with a Short Pulse, High Power Generators,**" Sandia National Laboratories Report, SAND78-1387C (1978)

65. J. H. Hammer, J. L. Eddleman, et al (including T. W. L. Sanford), **Two-dimensional radiation-magnetohydrodynamic simulations of SATURN imploding Z pinches**, *Phys. Plasmas* **3,** 2063 (1996).

66. T. W. L. Sanford, D. Mosher, et al, **X-Ray Emission from a High-Atomic-Number Z-Pinch Plasma Created from Compact Wire Arrays,** *Sandia National Laboratories*, SAND96-0222, Mar. 1996.

67. B. M. Marder, **"GAP-A PIC-TYPE fluid code"**, Math. of Comp., 29, 434 (1973).

68. S. Maxon, J. H. Hammer, et al (including T. W. L. Sanford), **MHD Solution for a Z-Pinch Showing the Production of Hot Spot**, *Phys. Plasmas* **3,** 1737 (1996).

69. N. R. Periera and J. Davis, *J. Appl. Phys.* **64**, R1 (1988).

70. J. J. Ramirez, *IEEE Trans. Plasma Sci.* **25**, 155 (1997).

71. R. B. Spielman, et al,. *In Third Int. Conf. Dense Z Pinches, London, UK, AIP Conference Proceedings* 299, pp. 404-420.

72. N. R. Pereira, Ed. *In Second Int. Conf. Dense Z Pinches, Laguna Beach, CA.* AIP Conference Proceedings 195, New York: AIP (1989).

73. M. G. Haines & A. Knight, Eds. In Third Int. Conf. on Dense Z-Pinches. London, UK, AIP Conference Proceedings 299, New York: AIP (1993).

74. L. E. Ruggles, et al, *Rev. Sci. Instrum.* **66**, 712 (1995).

75. K. G. Whitney, et al, J. Appl. Phys. 67, 1725 (1990).

76. J. W. Thornhill et al, J. Quant. Spectrosc. Radiat. Transf. 44, 251 (1990).

77. J. W. Thornhill, et al, Phys. Plasmas 1, 321 (1994).

78. T. W. L. Sanford, G. O. Allshouse, B. M. Marder, at al, **Improved Symmetry Greatly Increases X-ray Power from Wire-Array Z-Pinches**, *Phys. Rev. Lett*. **77** (25), 5063 (1996).

79. T. W. L. Sanford, R. C. Mock, T. J. Nash, et al, **Systematic Trends in X-Ray Emission Characteristics of Variable-Wire-Number, Fixed-Mass, Aluminum-Array, Z-Pinch Implosions**, *Phys. Plasmas* **6,** 1270 (1999).

80. B. M. Marder, T. W. L. Sanford, and G. O. Allshouse, **Numerical simulations of annular wire-array z-pinches in (x, y), (r, θ), and (r, z) geometries**, *Phys. Plasmas* **5**, 2997 (1998).

81. D. Mosher, in *Proceedings of the 10th International Conference on High power Particle Beams*, SanDiego, 1994, edited by W Rix and R. White, NTIS PB95-144317, p. 159.

82. D. Mosher and D. Colombant, *Phys. Rev. Lett.* 68, 2600 (1992).

83. D. L. Peterson et al, *Phys. Plasmas 3,* 368 (1996).

84. K. G. Whitney, J. W. Thornhill, et al, (including T. W. L. Sanford), **Analyzing Time-Resolved Spectroscopic Data from an Azimuthally Symmetric, Aluminum-Wire Array, Z-Pinch Implosion**, *Phys. Rev. E,* **56**, 3540 (1997).

85. K. G. Whitney, P. E. Pulsifer, et al (including T. W. L. Sanford), **Trends in plasma conditions inferred from an analysis of x-ray data from high wire-number, z-pinch load implosions**, *Phys. Plasmas* **8,** 3708 (2001).

86. J. P. Apruzese, P. E. Pulsifer, et al (including T. W. L. Sanford), **K-shell radiation physics in the ultrahigh optical depth pinches of the Z generator**, *Phys. Plasmas* **5**, 4476 (1998).

87. J. P. Apruzese, J. Davis, et al (including T. W. L. Sanford), **The physics of radiation transport in dense plasmas**, *Phys. Plasmas* **9,** 2411 (2002).

88. T. W. L. Sanford, G. O. Allshouse, B. M. Marder, et al, **X-ray Power Increase from Symmetrized Wire-Array Z-pinch Implosions**, *BEAMS '96, Proceedings of the 11th Inter. Conf. on High-Power Particle Beams*, 146 (Prague, Czech Republic, June 10-14, 1996), eds. K. Jungwirth and J. Ullschmied, Academy of Sciences of the Czech Republic, Za Slovankou 3, 182 00 Prague 8, Czech Republic (1996), p. 146.

89. T. W. L Sanford, T. J. Nash, R. C. Mock, et al, **Dynamics of a High-**

Power Aluminum-Wire Array z-Pinch Implosion, *Phys. Plasmas* **4**, 2188 (1997).

90. T.J. Nash, T. W. L. Sanford, C. Deeney, et al, **High Temperature, Dense Cores in an Aluminum Wire Array Z-Pinches Observed by Spatially-Resolved Spectroscopy,** J. *Quant. Spectrosc. Radiat. Transfer*, **60**, 97 (1998).

91. T. W. L. Sanford, T. J. Nash, R. C. Mock,et al, **Time-Dependent Electron Temperature Diagnostics for High-Power, Aluminum Z-pinch Plasmas**, *Rev. Sci. Instrum*. **68** (1), 852 (1997).

92. T. W. L. Sanford, R. C. Mock, R. B. Spielman, et al, **Increased x-ray power generated from low-mass large-number aluminum-wire-array Z-pinch implosions**, *Phys. Plasmas* **5**, 3737 (1998).

93. T. W. L. Sanford, R. C. Mock, R. B. Spielman, et al, **Symmetric aluminum-wire arrays generate high-quality Z pinches at large array radii**, *Phys. Plasmas* **5**, 3755 (1998).

94. D. Mosher, N. Qi, and M. Krishnan, *IEEE Trans. Plasma Sci*. **26,** 1052 (1998).

95. C. Deeney, T. J. Nash, R. B. Spielman, et al, *Phys. Rev. E* **56**, 5945 (1997).

96. R. J. Leeper, T. E. Alberts, G. A. Allshouse, et al, **Pulsed Power Driven Hohlraum Research at Sandia National Laboratories,** *BEAMS '96, Proceedings of the 11th Inter. Conf. on High-Power Particle Beams*, 146 (Prague, Czech Republic, June 10-14, 1996), eds. K. Jungwirth and J. Ullschmied, Academy of Sciences of the Czech Republic, Za Slovankou 3, 182 00 Prague 8, Czech Republic (1996), p. 37.

97. J. P. Quintenz, R. G. Adams, et al (including T. W. L. Sanford), **Progress in Pulsed Power Fusion**, *BEAMS '96, Proceedings of the 11th Inter. Conf. on High-Power Particle Beams*, 146 (Prague, Czech Republic, June 10-14, 1996), eds. K. Jungwirth and J. Ullschmied, Academy of Sciences of the Czech Republic, Za Slovankou 3, 182 00 Prague 8, Czech Republic (1996), p. 1.

98. Leland Johnson, **Sandia National Laboratories: A History of Exceptional Service in the National Interest,** Sandia National Laboratories Report SAND97-1029 (1997).

99. Gerold Yonas, **Fusion and the Z Pinch,** *Scientific American,* Pages 40-47, August 1998.

100. R. B. Spielman, C. Deeney, et al (including T. W. L. Sanford), **Tungsten wire-array Z-pinch experiments at 200 TW and 2 MJ**, *Phys. Plasmas* **5**, 2105 (1998).

101. M. L. Kiefer and M. M. Widner, Digest of Tech. Papers, *Fifth IEEE*

Pulse Power Conference, Arlington VA, 1985, edited by M. F. Rose and P. J. Turchi (IEEE, New Your, 1985), p.685.

102. T. W. L. Sanford, R. B. Spielman, G. O. Allshouse, et al, **Wire Number Doubling in High-Wire-Number Regime Increases Z-Accelerator X-ray Power**, *IEEE Trans. Plasma Sci.***26**, 1086 (1998).

103. D. L. Peterson, R. L. Bowers, J. H. Brownell, et al, *Phys. Plasmas* **3**, 368 (1996).

104. M. G. Haines, *IEEE Trans. Plasma Sci.* **26,** 1275 (1998).

105. J. P. Chittenden, R. Aliaga Rossel, S. V. Lebedev, et al, *Phys. Plasmas* **4**, 4309 (1997).

106. T. W. L. Sanford, R. C. Mock, R. B. Spielman, et al, **Wire Array Z-Pinch Insights for Enhanced X-Ray Production**, *Phys. Plasmas* **6**, 2030 (1999).

107. M. K. Matzen, C. Deeney, et al (including T. W. L. Sanford), **Fast Z-Pinches as a Dense Plasma, Intense X-ray Source for Plasma and Fusion Applications**, *Plasma Physics and Controlled Fusion* **41**, A175 (1999).

108. R. J. Leeper, T. E. Alberts, et al (including T. W. L. Sanford), **Z-pinch Driven Inertial Confinement Fusion Target Physics Research at Sandia National Laboratories**, *Nuclear Fusion* **39**, 1283 (1999).

109. R. E. Olson, G. A. Chandler, et al (including T. W. L. Sanford), **Indirect-Drive ICF Target Concepts for the X-1 Z-Pinch Facility**, *Fusion Technol..* **35**, 260 (1999).

110.R. E. Olson, T. W. L. Sanford, G. A. Chandler,et al, **Hohlraum temperature inference via measurement of aluminum shock velocity and time- and spatially resolved x-ray re-emission**, *Rev. Sci. Instrum*. **72** (1), 1214 (2001).

111. C. Deeney, M. R. Douglas, R. B. Spielman, et al, **Enhancement of X-ray power from a Z pinch using nested-wire arrrays**, *Phys. Rev. Lett.* **81,** 4883 (1998).

112. T. W. L. Sanford, R. E. Olson, R. L. Bowers, et al, **Z-pinch-generated x rays demonstrate potential for indirect-drive ICF experiments**, *Phys. Rev. Lett*. **83** (26), 5511 (1999).

113. T. W. L. Sanford, R. E. Olson, R. A. Vesey, et al, **Characteristics of ICF relevant hohlraums driven by x-rays from a z-pinch**, *Fusion Technol.*, **38**, 11 (2000).

114. T. W. L. Sanford, R. E. Olson, R. C. Mock, et al, **Dynamics of a z-pinch x-ray source for heating inertial-confinement-fusion relevant hohlraums to 120-160 eV**, *Phys. Plasmas* **7**, 4669 (2000).

115. T. W. L. Sanford, **Overview of the Dynamic Hohlraum X-ray Source at Sandia National Laboratories**, *IEEE Trans. Plasma. Sci.* **36**, No 1, 22 (2008).

116. J. P. Chittenden,, S. V.Lebedev, S. N. Bland, F. N. Beg, and M. G. Haines, **One-,two-, and three-dimensional modeling of the different phases of wire array Z pinch evolution,** *Phys. Plasmas*, **8**, 2305-2314, 2001.

117. T. W. L. Sanford, **Wire number breakthrough for high-power annular z pinches and some characteristics at high wire number**, *Laser and Part. Beams* **19**, 541(2001).

118. T. W. L. Sanford, R. W. Lemke, R. C. Mock, et al, **Dynamics and characteristics of a 215-eV dynamic hohlraum x-ray source on Z**, *Phys. Plasmas* **9**, 3573 (2002).

119. T. W. L. Sanford, N. F. Roderick, R. C. Mock, et al, **Azimuthal structure in wire-array z pinch experiments**, *IEEE Trans. Plasma. Sci.* **30**, 538 (2002).

120. R. E. Peterkin, M. H. Frese, and C. R. Sovinec, **Transport of magnetic flux in an arbitrary coordinate ALE code**, *J. Comp. Phys.*, **140**, 148 (1998).

121. T. W. L. Sanford, R. W. Lemke, R. C. Mock, et al, **Trends in radiation production from dynamic-hohlraums driven by single and nested arrays**, *Phys. Plasmas* **10**, 3252 (2003).

122.T. W. L. Sanford, R. C. Mock, S. A. Slutz, et al, **Length scaling of dynamic hohlraum axial radiation**, *Phys. Plasmas* **10**, 4790 (2003).

123.T. W. L. Sanford, R. C. Mock, R. J. Leeper et al, **Unexpected axial asymmetry in radiated power from high-temperature dynamic-hohlraum x-ray sources**, *Phys. Plasmas* **10**, 1187 (2003).

124. T. W. L. Sanford, T. J. Nash, R. C. Mock, et al, **Evidence and mechanisms of axial-radiation asymmetry in dynamic hohlraums driven by wire-array z-pinches**, *Phys. Plasmas* **12**, 022701 (2005).

125. J. P. Apruzese, R. W. Clark, et al (including T. W. L. Sanford*)*, **Diagnosing dynamic hohlraums with tracer absorption line spectroscopy** *Phys. Plasmas* **12,** 1 (2005).

126. T. W. L. Sanford, T. J. Nash, R. C. Mock, et al, **Diagnosed internal temperatures and shock evolution provide insight on dynamic-Hohlraum's axial radiation production and asymmetry**, *Phys. Plasmas* **13**, 012701 (2006).

127. J. P. Apruzese, R. W. Clark,_et al, (including_T. W. L. Sanford*)*, **Comparative properties of the interior and blowoff plasmas in a dynamic hohlraum**, *Phys. Plasmas* **14**,

1 (2007).

128. T. W. L. Sanford, R. C. Mock, J. F. Seamen, et al, **Wire fixturing in high wire-number z pinches critical for high radiation power and reproducibility**, *Phys. Plasmas* **12**, 122701 (2005).

129. P. U. Duselis and B. R. Kusse, *Phys. Plasmas* **10,** 565 (2003).

130. D. B. Sinars, T. A. Shelkovenko, S. A. Pikus, et al, *Phys. Plasmas* **7,** 429 (2000).

131. G. S. Sarkisov, P. V. Sasorov, K. W. Struve, et al, *Phys. Rev. E* **66**, 046413 (2002).

132. T. W. L. Sanford, M. E. Cuneo, D. E. Bliss, et al, **Demonstrated transparent mode in nested wire arrays used for Dynamic Hohlraum Z-pinches**, *Phys. Plasmas* **14**, 052703 (2007).

133. T. W. L. Sanford, T. J. Nash, R. E. Olson, et al, **Progress in z-pinch driven dynamic-hohlraums for high-temperature radiation-flow and ICF experiments at Sandia National Laboratories**, *Plasma Phys. Control. Fusion* **46**, B423-B433 (2004).

134. T. A. Mehlhorn, et al, *Plasma Phys. Control. Fusion* **45,** A325 (2003).

135. S. A. Slutz, et al, *Phys. Plasmas* **10,** 1875 (2003).

136. J. E. Bailey, et al *Phys. Rev. Lett.* **92,** 085002-1 (2004).

137. C. L. Ruiz, et al, *Phys. Rev. Lett.* **93**, 015001-1 (2004).

138. C. L. Olson, **Z-Pinch inertial fusion energy,** *Landholt-Bornstein Handbook on Energy Technologies,* ed K Heinloth (Berlin: Springer) 2004.

139. M. G. Haines, T. W. L. Sanford, and V. P. Smirnov, **Wire-array z-pinch: a powerful x-ray source for ICF**, *Plasma Phys. Control. Fusion* **47**, B1-B11 (2005).

140. R. E. Terry, J. Davis, C Deeney, and A. L. Velikovich, *Phys. Rev. Lett* **83**,4305 (1999).

141. M. E. Cuneo, D. B. Sinars, E. M. Waisman, et al, *Phys. Plasmas* **13**, 056318 (2006).

142. E. M. Waisman, M. E. Cuneo, A. A. Stygar, et al, *Phys Plasmas* **11**, 2009 (2004).

143. J. P. Chittenden, S. V. Lebedev, C. A. Jennings, S. N. Bland, and C. Ciardi, Plasma Phys. Controled Fusion 46, B457 (2004).

144. T. W. L. Sanford, C. A. Jennings, G. A. Rochau, et al, **Wire initiation critical for radiation symmetry in z-pinch-driven dynamic hohlraums**, *Phys. Rev. Lett*. **98** 065003 (2007).

145. M. G. Mazarakis, C. E. Deeney, W. A.

Stygar, et al, *Phys. Plasmas* **18**, 112706-1 (2011).

146. S. V. Lebedev, F. N. Beg, S. N. Bland, et al, *Phys. Plasmas* **9**, 2293 (2002).

147. Richard Wilson, Ed., **Energy for the Year 2000,** *Plenum Press,* New York, 1980.

148. T. W. L. Sanford, **Number of Detectable Kaon Decays at LAMPF II**, *LANL Report*, LA-9334-MS (April 1982).

149. T. W. L. Sanford, **Rare Kaon Decays at LAMPF II,** *LANL Report,* LA-9385-MS (June 1982).

150. T. W. L. Sanford, **LAMPF II--Also a Hyperon Factory,** *LANL Report,* LA-9386-MS (June 1982).

151. J. F. Seamen, J. P. VanDevender, D. L. Johnson, et al, in *Proceedings of the Fourth IEEE Pulsed Power Conference,* Albuquerque, NM June 6-8, 1983.

152. K. R. Prestwitch, D. Hasti, R. B. Miller, and A. W. Sharp, *IEEE Trans. Nucl. Sci.* W-30, No 4, 3155 (1983).

153. T. W. L. Sanford, J. A. Halbleib, J. W. Poukey, C. E. Heath, and R. Mock, **Dose-Voltage Dependence of Coaxial Bremsstrahlung Diodes,** *Nuclear Instrum. and Methods in Physics Research* B34, 347-356 (1988).

154. T. W. L. Sanford, D. Mosher, J. S. De Groot, et al, **X-ray Emission from a High-Atomic-Number Z-Pinch Plasma Created from Compact Wire Arrays**, *BEAMS '96, Proceedings of the 11th Inter. Conf. on High-Power Particle Beams*, 146 (Prague, Czech Republic, June 10-14, 1996), eds. K. Jungwirth and J. Ullschmied, Academy of Sciences of the Czech Republic, Za Slovankou 3, 182 00 Prague 8, Czech Republic (1996), p. 753.

155. T. W. L. Sanford, J. A. Halbleib, J. W. Poukey, and T. P. Write, **Theoretical Motivation of Indented-Anode Diode for HERMES III**, *Sandia Report* SAND85-2383, January 1987.

156.T. W. L. Sanford, J. A. Halbleib, and J. W. Poukey, **Preoperational Radiation Studies for HERMES III Using an Indented-Anode Diode**, *Sandia Report* SAND-0424, June 1988.

DISTRIBUTION

External:

Lawrence Livermore National Laboratory
Attn: N. Dunipace (1)
P.O. Box 808, MS L-795
Livermore, CA 94551-0808

Lawrence Livermore National Laboratory
Attn: J. H. Hammer
P. O. Box 808
Livermore, CA 94550

Berkeley Research Associates
Attn: Dr. N. R. Periera
P.O. Box 852
Springfield, VA 22150

Prof. Jeremy Chittenden
Plasma Physics Group,
Blackett Laboratories
Prince Consort Rd
South Kennsington, London
SW72BZ
UK

Dr. John Hardwick
Culham Laboratory
OXON OX14 3DB
UK

C.E.R.N.
CH-1211
Attn: Dr. W. Blum
Dr. W. Manner
Geneva 23
Switzerland

University of Chicago
Physics Department
Attn: Prof. L. M. Lederman
Chicago, IL 60637

Prof. L. M. Lederman
Fermilab
P.O.Box 500, Batavia, IL 60510

Dr. Wendland Beezhold
1110 Yellowstone Ave. PMB 322
Pocatello, Id 87201

Dr. Hans Jensen
804 Bridle Lane
Wheaton, Ill 60187

Dr. Darrell Peterson
Los Alamos National Laboratory
P.O.Box 1663
Los Alamos, NM 87545

Dr. Juan Ramirez
8315 Casa Gris CT NW
Albuquerque, New Mexico 87120

Dr. Phil Spence
240 Kuss Road
Danville, CA 94526

Dr. Jeffrey Turner
4676 Admiralty Way, Suite 101
Marina del Rey, CA 90292

Prof. David Hammer
327 Rhods Hall
Cornell Univeristy
Ithaca, NY 14853

Prof. Y. Maron
Weizmann Institute
Rehovot 76100 ISRAEL

Naval Research Laboratory
Attn: Dr. John P. Apruzese
Dr. K. G. Whitney
Washington DC 20375

Internal:

1	MS 0899	Technical Library, 9536 (electronic copy)
1	MS 1169	J. Lee, 1300
1	MS 1179	G. Heffelfinger, 1340
1	MS 1179	L. Lorence, 1341
1	MS 1179	R. Kensek, 1341
1	MS 1106	R. Thomas, 1342
1	MS 1167	F. Hartman, 1343
1	MS 1159	J. Bryson, 1344
1	MS 1159	V. Slaboszewicz, 1344
1	MS 1468	N. Singer, 3651
1	MS 1478	P. Armstrong, 3554
1	MS 1190	M. K. Matzen, 1600
1	MS 1191	Mary Ann Sweeney, 1610
1	MS 1189	M. Herrmann, 1640
1	MS 1189	P. VanDevender, 1640
1	MS 1193	M. Cuneo, 1643
1	MS 1106	D. Ampleford, 1643
1	MS 1193	B. Jones, 1643
1	MS 1193	D. Rovang, 1643
1	MS 1193	E. Waisman, 1643
1	MS 1186	C. Nakhleh, 1644
1	MS 1186	P. Christenson, 1644
1	MS 1106	C. Jennings, 1644
1	MS 1186	S. Slutz, 1644
1	MS 1186	R. Vesey, 1644
1	MS 1186	E. Yu, 1644
1	MS 1195	G. Leifeste, 1647
1	MS 1193	D. Sinars, 1648
1	MS 1196	D. Schroen, 1648
1	MS 1181	L. Schneider, 1650
1	MS 1178	M. Kiefer, 1612
1	MS 1168	B. Oliver, 1656
1	MS 1168	R. Commisso, 1656
1	MS 1168	G. Cooperstein, 1656
1	MS 1168	D. Welch, 1656
1	MS 1191	J. Porter, 1670
1	MS 1196	W. Stygar, 1671
1	MS 1194	M. Mazarakis, 1671
1	MS 1192	M. Jones, 1674
1	MS 1196	G. Rochau, 1675
10	MS 1196	R. Leeper, 1677
1	MS 1196	J. Bailey, 1677
1	MS 1196	G. Chandler, 1677
1	MS 1196	G. Cooper, 1677
1	MS 1196	D. Fehl, 1677
1	MS 1196	R. Olson, 1677
1	MS 1196	C. Ruiz, 1677
20	MS 1196	T. Sanford, 1677